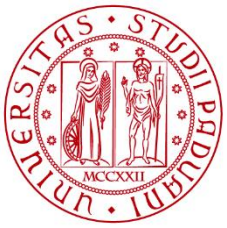

UNIVERSITÀ DEGLI STUDI DI PADOVA

UNIVERSITÀ DEGLI STUDI DI PADOVA
DIPARTIMENTO DI SCIENZE CHIMICHE

SCUOLA DI DOTTORATO DI RICERCA IN SCIENZE MOLECOLARI
INDIRIZZO SCIENZE CHIMICHE
XXVII CICLO

DEFECTS IN CARBON-BASED MATERIAL STUDIED BY ELECTRON PARAMAGNETIC RESONANCE METHODS

DIRETTORE DELLA SCUOLA: CH.MO PROF. ANTONINO POLIMENO

COORDINATORE D'INDIRIZZO: CH.MO PROF. ANTONINO POLIMENO

SUPERVISORE: DR. ANTONIO BARBON

DOTTORANDO: FRANCESCO TAMPIERI

INDEX

ABSTRACT

The study of defects in carbon-based materials is of great interest, because of their elusive nature and because these defects determine some of their fundamental electronic, optical and magnetic properties.

The type of defects depends strongly on the materials structure. In ordered materials, for example, defects are due to distortions of the crystalline structure, while in amorphous materials they are related most to unsaturated bonds. In recent years, great interest has grown on graphene and graphene-like systems. The properties of these materials make them very promising for electronic and mechanical applications. Deviations from perfection can also be useful in some tecnical applications, as they enable to tailor the local properties of graphene and to achieve new functionalities.

Most of the defects that can be found in carbon-based materials are characterized by the presence of unpaired electrons and are therefore paramagnetic. In several cases, the existence of unpaired spins within a material can lead also to cooperative magnetism phenomena. A complete and accurate description of the defects distribution in a material is therefore of fundamental importance for its possible applications.

In this thesis, we identify and characterize the different types of defects that can be found in graphene-like systems by using electron paramagnetic resonance (EPR) spectroscopy and Density Functional Theory (DFT) calculations. We study materials with different types of defects and try to correlate their EPR characteristics with their structure. We also report a study on the reactivity of these materials that is determined by the presence of defects.

RIASSUNTO

Lo studio dei difetti in materiali carboniosi è di estremo interesse a causa della loro natura sfuggente e perché questi difetti determinano alcune delle fondamentali proprietà elettroniche, ottiche e magnetiche.
Il tipo di difetti dipende fortemente dalla struttura dei materiali. In materiali ordinati i difetti sono dovuti a distorsioni della struttura cristallina, mentre in materiali amorfi sono maggiormente legati alla presenza di legami non saturati. Negli ultimi anni, l'interesse della comunità scientifica nei confronti del grafene e di materiali con struttura grafenica è aumentato esponenzialmente. Le proprietà di questi materiali li rendono estremamente promettenti per applicazioni elettroniche e meccaniche. Deviazioni dalla perfezione possono essere utili per alcune applicazioni dal momento che permettono di modificare le proprietà locali del grafene per ottenere nuove funzionalità.
La maggior parte dei difetti che si possono trovare in materiali carboniosi è caratterizzata dalla presenza di elettroni spaiati e per questo sono paramagnetici. In diversi casi, l'esistenza di spin spaiati in un materiali può portare anche a fenomeni di magnetismo di cooperazione. Una completa e accurata descrizione della distribuzione di difetti nei materiali è quindi di fondamentale importanza per le loro possibili applicazioni.
In questa tesi, abbiamo identificato e caratterizzato i diversi tipi di difetti che si possono trovare in sistemi di tipo grafenico usando la spettroscopia di risonanza paramagnetica elettronica (EPR) e calcoli basati sulla teoria del funzionale densità (DFT). Abbiamo studiato materiali con diversi tipi di difetti e abbiamo correlato le loro caratteristiche EPR con le strutture. E' riportato inoltre uno studio sulla reattività di questi materiali determinata dalla presenza dei difetti.

CHAPTER 1 - INTRODUCTION

1.1 - Carbon-based materials

Carbon-based materials have captured broad interest in the materials science community for decades. Carbon is an extremely light and versatile material that, depending on the local bonding of the constituting carbon atoms, has hugely varying properties. Well-known classic examples of carbon allotropes are diamond, amorphous carbon and graphite. More recently discovered allotropes are buckminsterfullerenes or buckyballs, carbon nanotubes and of course graphene.
The amazing feature of carbon to combine with itself and other elements in many different ways is the basis of all organic and biological chemistry. The chemical flexibility of this element is also the cause of the wide variety of structural forms of solid carbon.
Carbon is able to form different allotropes because of its valence (Fig. 1.1). The more typical, that are known since centuries, are diamond, graphite and amorphous carbon. Diamond and graphite are ordered crystalline materials, with respectively a sp^3 and a sp^2 carbon network; graphite is made of sp^2 carbon sheets (graphene) that are stacked together via Van der Waals interactions. In amorphous carbon, there is no crystalline structure and therefore, no long-range order; different type of bonds can be found in this material. In recent decades, many more allotropes and forms of carbon have been discovered and researched including ball shapes such as buckminsterfullerene and sheets such as graphene. Larger scale structures of carbon include nanotubes, nanobuds and nanoribbons. Other unusual forms of carbon exist at very high temperature or extreme pressures.

1.2 - Graphene

Graphene is a carbon allotrope. Its structure is based on a single layers or carbon atoms arranged in a hexagonal bidimensional lattice and can be seen as the starting point for obtaining other carbon-based materials with different dimensionality. Graphene can be wrapped to give fullerene (0D), rolled to give nanotubes (1D) or stacked to give graphite (3D) (Fig. 1.2).
Graphene is studied, with theoretical approaches, from at least sixty years [1], and until a few years ago it was considered a purely academic material because it was thought that it could not be isolated and that it was unstable with respect to formation of curved structures (fullerenes and nanotubes). Only in 2004 Geim and Novoselov, have managed to produce, isolate, identify and characterize experimentally graphene [2]. Thanks to these studies, they were awarded the Nobel

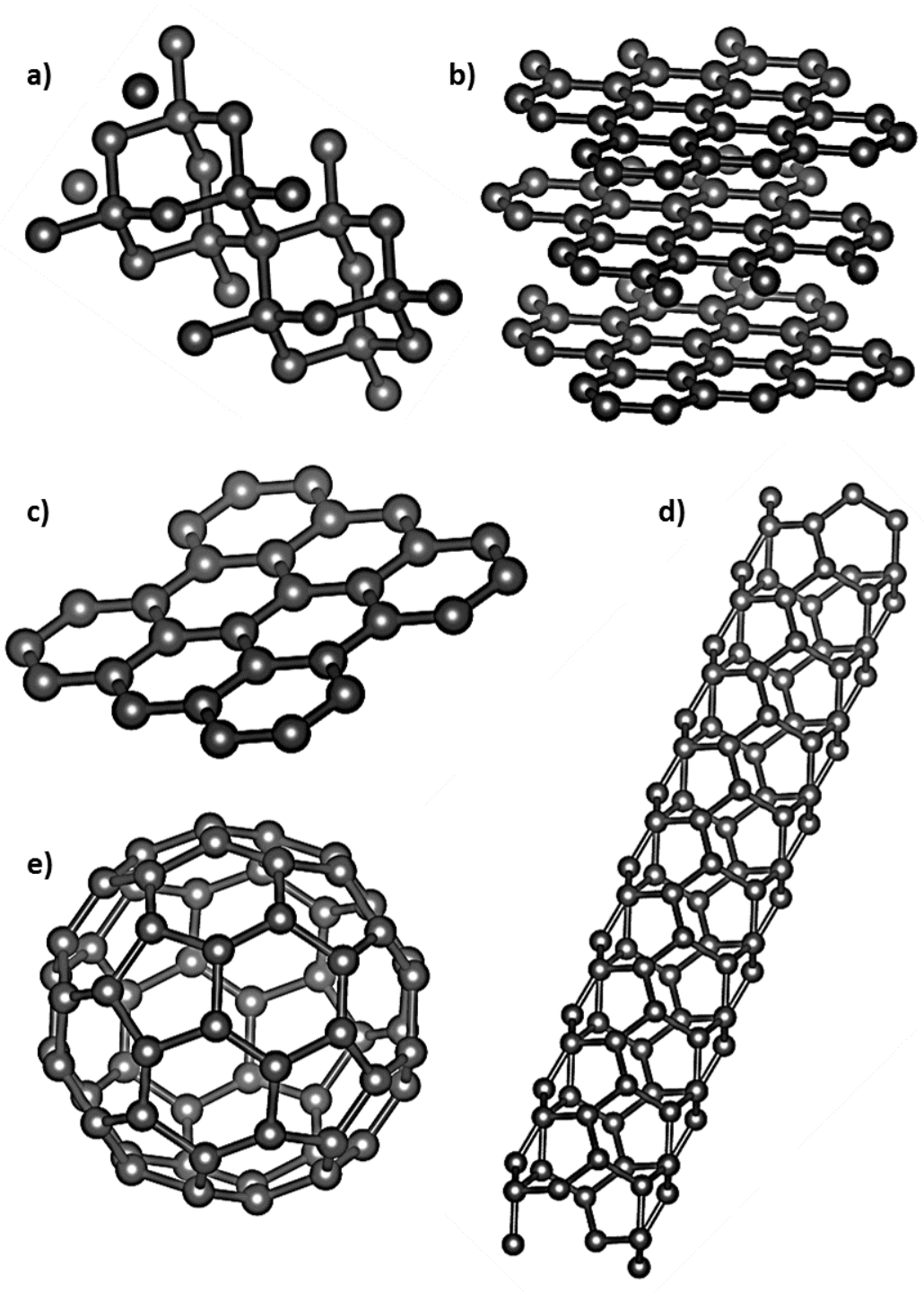

Figure 1.1 Structures of carbon-based materials: a) cubic diamond; b) graphite; c) graphene; d) carbon nanotube; e) Buckminsterfullerene.

Prize for physics in 2010.

The unique properties of graphene make it an excellent candidate for different applications. One of the first applications to be proposed is the use of graphene for the preparation of nano-polymer composites with many improved properties like electrical conductivity, thermal stability, elastic modulus and tensile strength [3]. The

use of graphene in electronics is very promising because of its high carriers mobility and low electronic noise. These properties have been exploited for the fabrication of high-performance field-effect transistor [2,4]. The zero band-gap makes graphene a poor candidate in the field of digital electronics. A way to overcome this limitation consists in the use of graphene nanoribbons (GNRs). GNRs have a band-gap suitable for electronic applications; the dimension of the gap can be tuned by varying the size of the ribbon or the geometry of the edges [5]. The excellent electrical conductivity and high optical transparency of graphene make it an ideal candidate for the development of transparent electrodes and conductors, with important consequences for optoelectronics and photovoltaics [5]. The exceptionally high surface to volume ratio has induced the scientific community to investigate the potentialities of graphene in the field of gas detection; the ability to detect single molecules has been demonstrated [6]. In the literature are shown many other possible applications of graphene, in addition to those just named, from the use in distillation processes [7], to the development of equipment for biomedical applications [8] up to the antibacterial for purposes related to hygiene and food preservation [9].

The $C - C$ bond length in graphene is 1.42 Å, the unitary cell contains two carbon

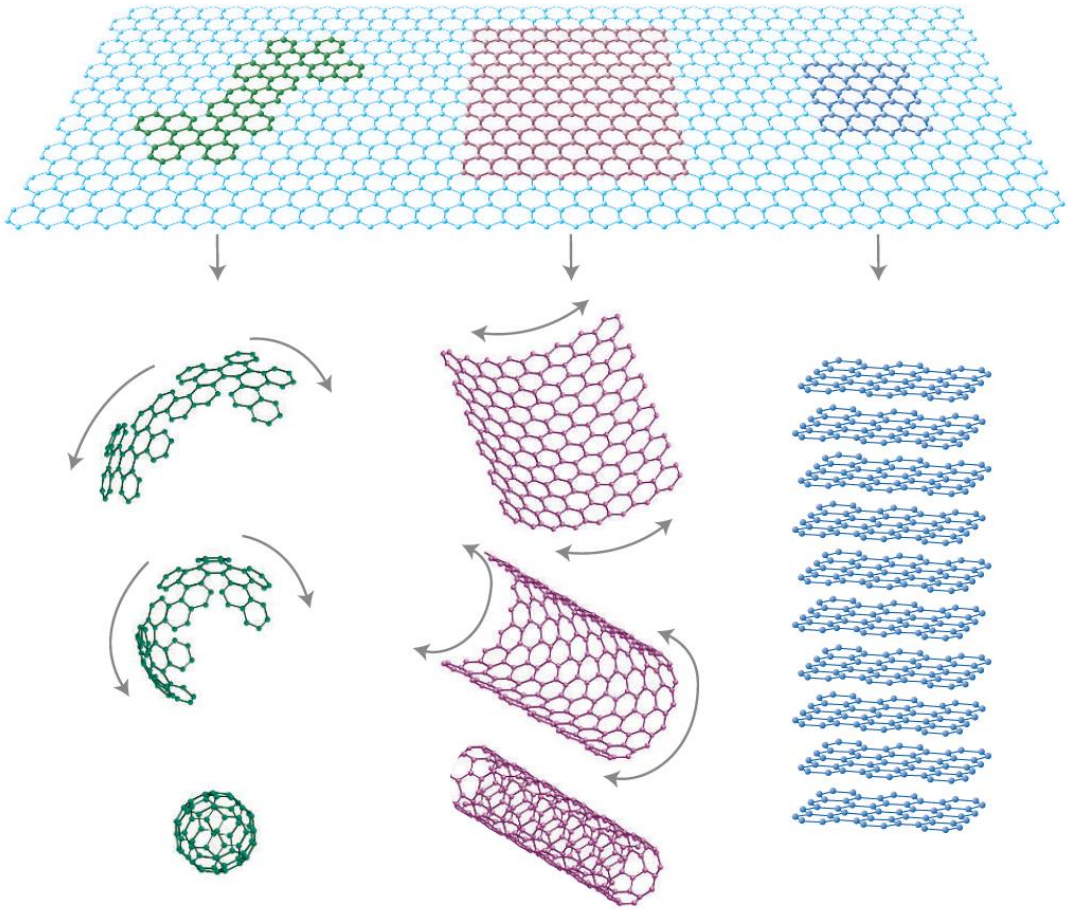

Figure 1.2 Fullerene, carbon nanotube and graphite obtained starting from a graphene sheet.

atoms and has an area of 5.2 Å^2; the density of graphene is therefore 0.77 mg m^{-2}. Intrinsic graphene is a zero band-gap semiconductor. The electronic structure of graphene is quite different from those of normal 3D materials; the Fermi surface is characterized by six double cones (Fig. 1.3). In intrinsic graphene, the Fermi level is located at the connection points of the cones. Since the density of states is zero at these points, the electrical conductivity of graphene, for temperatures different from zero, is quite low. It is possible however to change the Fermi level by using electromagnetic fields, doping the material with electrons or with holes, depending on the polarity of the applied field. Graphene can also be doped by adsorption of molecules, such as water or ammonia. The conductivity in these cases is potentially very high, and at room temperature may exceed that of copper [10].

Graphene is a perfect thermal conductor. Its thermal conductivity is much higher if compared to what observed in other carbon-based materials [11]. The hardness of graphene is superior to that of diamond and at least 200 times greater than steel [12]. In addition to that, graphene is also very stretchable, up to 20% of the initial length. These properties are very interesting for applications in the field of new composite materials. Graphene is able to adsorb and desorb different atomic or molecular species (such as NO_2, NH_3, K, and OH). The adsorbed species can act as donors or acceptors by changing the concentration of the charge carriers and significantly increasing the conductivity of the material [6]. Graphene can also be functionalized with various groups, for example OH^- or F^-, to give graphene oxide or fluorinated graphene, which show very different chemical properties from the pure material.

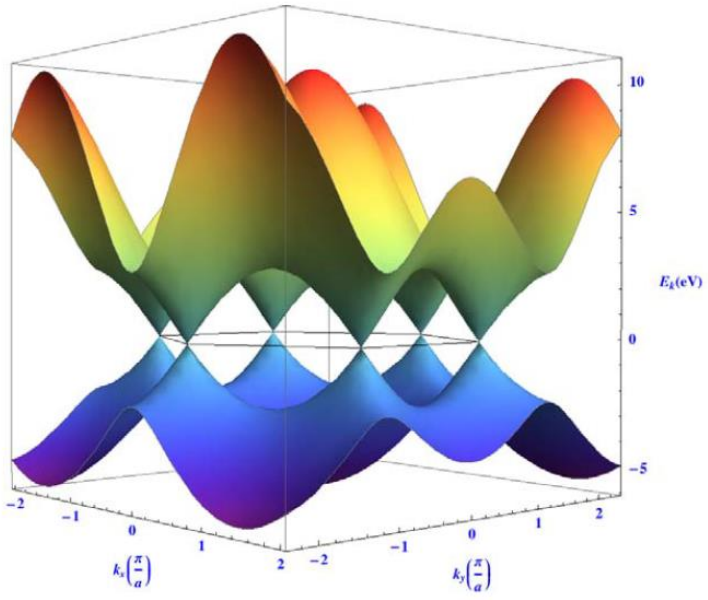

Figure 1.3 Energy surface near the Fermi level in the k_x and k_y space. The central line represents the Fermi energy for undoped graphene. Near the Fermi level the energy surface has the shape of six double cones.

In literature, many methods of production of graphene are reported. The first used method, called scotch tape or drawing method [2], involves the mechanical exfoliation of graphite using adhesive tape. Another method is based on the treatment at high temperature of silicon carbide until it becomes graphene [13]. Alternatively, it is possible to obtain graphene by epitaxial growth on metal substrates by chemical vapor deposition (CVD) [14].
The probably most used method is the reduction of graphite oxide (GO) [15]. The material produced in this way is low in quality when compared with other methods of synthesis due to incomplete removal of the functional groups. Moreover, several evidences point towards metal ions residues deriving from the synthesis of GO. In particular, some authors identified the presence Mn(II) ions [16,17] as a consequence of using potassium permanganate as an oxidant. Other methods are the unzipping of carbon nanotubes by treatment with potassium permanganate and sulfuric acid [18] and the chemical exfoliation of graphite by intercalation with strong reducing metals and treatment with protic solvents [19]. This last method was used to produce the expanded graphites that we will study in Chapter 3.

1.3 - Defects in graphene-like materials

Imperfections and defects are very common in carbon-based materials. They change deeply the chemical and physical properties of graphite and graphene. Sometimes defects come from imperfections in the crystal lattice, sometimes from the synthesis of the materials and sometimes are they are introduced on purpose to modify and tune the reactivity of the systems.
Defects in three-dimensional crystals are called intrinsic if the crystalline order is perturbed without the introduction of foreign atoms. If those atoms are present, they acts as impurities and constitute extrinsic defects. In macroscopic crystalline materials, we can have intrinsic defects with different dimensionalities. Point defects (vacancies, interstitial atoms, etc.) are zero-dimensional and dislocations are mono-dimensional because are based on a line of defects. Grain boundaries and stacking faults are two-dimensional defects while inclusions and voids extend in three dimensions. Extrinsic defects can also have different dimensionalities, if a single carbon atom is substituted with other elements or if there is an interstitial atom the defect is zero-dimensional. If there are agglomerations of heteroatoms, they can extend to more dimensions.
We give here a brief overview of defects that can be found in graphene-like materials. We will see some of these defects in the experimental chapters (Chapters 3 and 4) and some of them will be studied theoretically in Chapter 5. The reduced

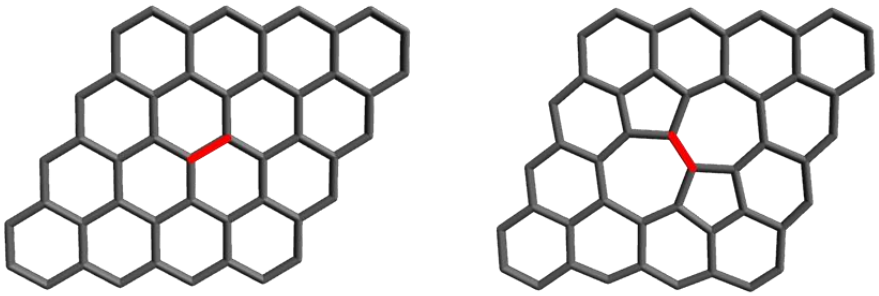

Figure 1.4 Stone-Wall defect. This defect comes from the rotation of a $C - C$ bond by 90° (red bond). Two heptagons and two pentagons are formed.

dimensionality of graphene makes the number of possible defects lower; three-dimensional defects do not exist in graphene-like materials.
Defects are not always stationary. They can migrate, and this can affect deeply the properties of the materials. In graphene and graphite, the defects can migrate parallel to the graphene plane. The mobility can be very low or very high; it is generally governed by an energy barrier with depends on the type of defects and increases with the temperature.

1.3.1 - Point defects

Stone-Wales defects. The graphene lattice has the ability to reconstruct by forming non-hexagonal rings. Stone-Wall (SW) defect [20] is an example of this ability. In a SW defects the total number of carbon atoms does not change, four hexagon turn into two pentagon and two heptagon after the rotation of one $C - C$ bond by 90° (see Figure 1.4); by doing so no dangling bond is formed. The SW defect has a formation energy of about 5 eV [21,22] so at room temperature, there is a negligible equilibrium concentration of such defects. The reverse process has also an energy barrier of about 5 eV, so if defects are formed at high temperatures or because of high energies, they remain stable.

Single vacancies (SV). This kind of defect comes when an atom of the lattice is missing. Single vacancies have been observed by TEM [23] and STM [24]. If one atom is removed from the graphene lattice, three dangling bonds are formed; in order to minimize the energy, the system undergoes Jahn-Teller distortion that leads to the saturation of two dangling bonds, leaving only one dangling bond. This results in the formation of a pentagonal ring and a nine-membered ring (Fig. 1.5). A SV implies an increase in the local density of states at the Fermi energy, which is localized on the dangling bond. Because of the presence of the dangling bond, the formation energy of a SV is quite high, calculations give values of about 7.5 eV [25,26]. The SV can migrate along the graphene plane already at relative low temperatures (100-200 °C) since the energy barrier is about 1.3 eV [25,26].

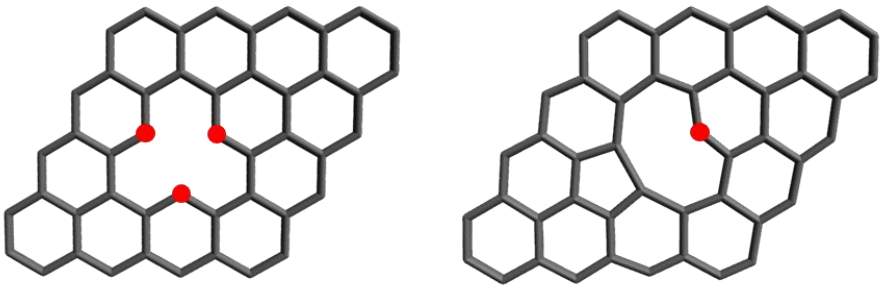

Figure 1.5 Single vacancy. If a carbon atom is removed three dangling bonds are formed (red circles, left). The structure rearranges to minimize the number of dangling bonds by forming a pentagonal ring and a nine-membered ring (right).

Multiple vacancies. Double vacancies (DV) can be formed by the removal of two nearby carbon atoms, or by coalescence of two SV. Instead of four hexagons, the structure is rearranged to form two pentagons and one octagon without dangling bonds. This structure can rearrange by rotation of a single bond to form other structures that are energetically more favoured (Fig. 1.6). The formation energy for a DV is similar to the formation energy for a SV (about 8 eV [25,26]), so the formation energy per missing atom is lower for DV. If more than two carbon atoms are removed, complex structure are formed. The removal of an odd number of atoms results in the formation of dangling bonds. Nonhexagonal rings induce local Gaussian curvature in a graphene sheet. Pentagons lead to positive (spherical) and heptagons to negative (saddle-like) curvature. This kind of topological modification can affect many properties of the materials including the EPR properties; the dependence of the EPR properties on the geometrical modification of a graphene sheet is studied in Chapter 5.

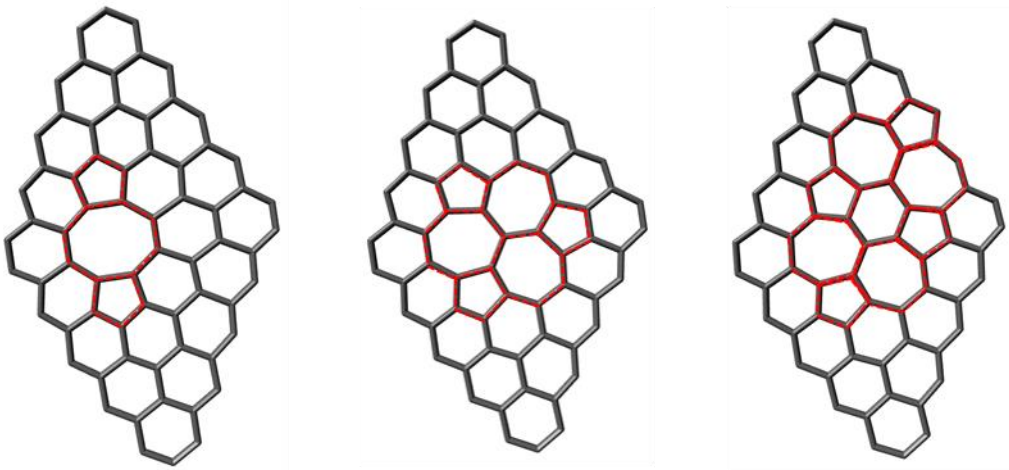

Figure 1.6 Double vacancies. Rearrangements that follow the formation of a double vacancies. The second structure derives from the first after the rotation of a $C-C$ bond, the third derives from the second after the rotation of another bond. No dangling bonds are present in these structures.

Carbon adatoms. In graphite can exist interstitial atoms between graphene planes. In single layer graphene, additional carbon atoms cannot be placed inside the graphene plane without increasing prohibitively the energy of the system. Additional carbon atoms can occupy some position out of the graphene plane. When a carbon atom interacts with a perfect graphene layer, the hybridization of the carbon atoms in the layer changes. Some degree of sp^3-hybridization can appear locally so that two new covalent bonds can be formed between the adatom and the underlying atoms in the graphene plane. Carbon adatoms can easily migrate along the graphene plane and can form dimers that could be inserted inside the graphene lattice [27].

Foreign adatoms. The effect of a foreign (non-carbon) atom on the properties of graphene depends on the bonding between the atom and graphene [28]. If the bond is weak, only physisorption due to Van der Waals interaction occurs. If the interaction is stronger, covalent bonding between the foreign atom and the nearest carbon atoms leads to chemisorption.

Substitutional impurities. Foreign atoms can be incorporated into the graphene lattice by replacing one or two carbon atoms. Boron and nitrogen have been extensively studied as dopant for graphene since they have respectively one less and one more electron than carbon and more or less the same atomic radius. In this case impurities move the Fermi level of graphene and change its electrical properties [29,30]. Doping by nitrogen is also a good way to introduce reactive sites in carbon materials to be used for subsequent reactions [31]. Substitutional dopants, once formed, are very stable because of the formation of covalent bonds. These kind of defects are treated more deeply in Chapter 4 where it is reported an EPR study of some pure and N-doped graphene-like systems.

1.3.2 - One-dimensional defects

Dislocation-like defects. Line defects in graphene frequently separate domains of different crystal orientation. They are formed because of the simultaneous

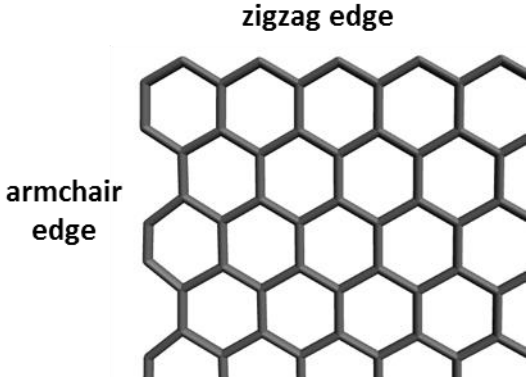

Figure 1.7 Zigzag and armchair edges that can be found in a real graphene flake.

nucleation of graphene at different points that may lead to independent two-dimensional domains, corresponding to grains in three-dimensional crystals. These linear defects in graphene are of paramount importance. The properties of polycrystalline materials are often dominated by the size of their grains and by the atomic structure of the grain boundaries, but the role of such structures should be pronounced in two-dimensional materials such as graphene where even a line defect can divide and disrupt a crystal.

Edges. A non-ideal graphene layer has edges. These edges can be free, with dangling bonds or passivated with hydrogen atoms. The structure of the edges can be zigzag or armchair (Fig. 1.7). The properties of the materials are severely affected by the presence and the type of the edges. The orientation of the graphene edge determines the energy spectrum of π-electrons. For example, zigzag edges possess localized edge states with energies close to the Fermi level [32]. Hydrogen atoms and other chemical groups that can saturate dangling bonds at the edge under ambient conditions may be considered as disorder, dramatically increasing the number of possible edge defects.

Localized electrons can be found not only along the external edges of a graphene flakes, but in some cases, depending on the geometry of the system, also along the edges of vacancies inside the flake [33]. The simple Hückel calculations reported in

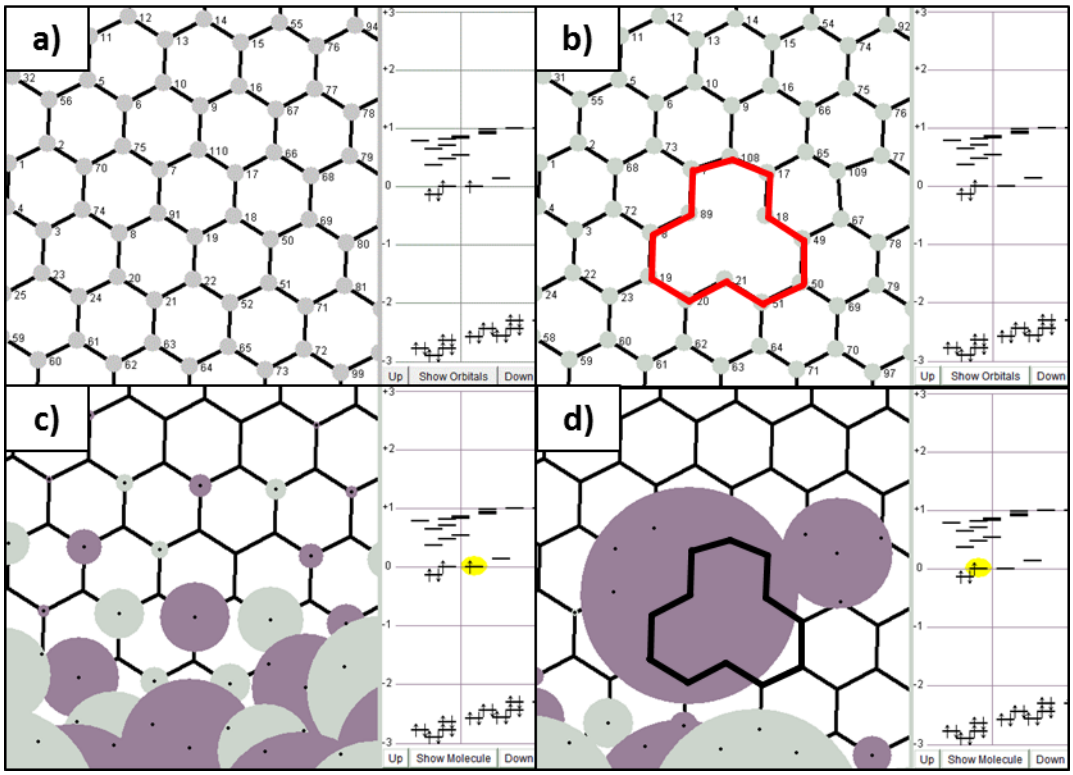

Figure 1.8 Hückel calculation of the frontier orbital for an ordered graphene sheet a) and c) and of the same graphene sheet after removal of a carbon atom b) and d).

Figure 1.8 show that the removal of a carbon atom from a certain position of the graphene lattice may result in a localization of the unpaired electron in that position. The study of the localized electrons in edge states of graphene-like materials is one of the major purposes of this thesis. They will be studied both experimentally with spectroscopic techniques and theoretically by DFT calculations.

1.3.3 - Properties induced by defects

Defects deeply affect the properties of the materials. The presence of defects affects the electronic properties of conductive materials, like graphite, graphene and nanotubes. Defect states can modify the Fermi level and enable a fine-tuning of the band-gap. The study of defects enables also to understand the magnetic properties of graphene, fullerenes, nanotubes and nanodiamonds that in the pristine form should be diamagnetic. Under-coordinated carbon atoms, vacancies, interstitials, carbon adatoms have local magnetic moments that may give rise to magnetic ordering.

Defects change essentially also the chemical properties of carbon-based materials, being centers of their chemical activity. Perfect graphene, graphite and carbon nanotubes are chemically stable materials, because of the strong π-interaction of their hexagonal network. However, if there are imperfections, defects or dopants, the chemical properties of the materials change and the reactivity increases [34-38]. The presence of dangling bonds for example enhance the chemical reactivity towards lots of functional groups [30,39]. Defects can also change the reactivity by modifying the π density, like for example in zigzag edges [40].

The functionalization of graphite and graphene for example is much easier in presence and in proximity of defects [41]. Lee and coworkers studied defective graphite produced by ion bombardment and showed with scanning tunneling microscopy its increased activity toward the reaction with molecular oxygen [42,43]. Many DFT-based studies report also the enhanced chemical reactivity of defective carbon materials with respect to the pristine materials for the reaction of addition of some functional groups (like O, CH_3 and O_3, etc.) [44,45]. Wang et coworkers report an increased defect reactivity at grain boundaries in graphene [45]. They found that the formation energies of interstitial carbon atoms and single vacancies are lower at grain boundaries than in pristine graphene.

Denis and Iribarne [46] found out a ranking of reactivity of different types of defects in graphene. They showed that, for the addiction of one functional group, the reactivity decreases with the following order: single vacancy > hydrogenated zigzag edge > double vacancy > Stone−Wales defects > hydrogenated armchair edge > perfect graphene. They found also that the extent to which defects increase reactivity is strongly dependent on the functional group attached to the structure. The lower the binding energy of the functional group onto perfect graphene, the larger the increase in reactivity.

Many reactions that are catalyzed on surfaces have been prover to have higher rates if the surface is defective. Most of these studies are done on inorganic compounds, but those findings are true also for carbon materials [47]. In a study on oxygen adsorption on defective graphene-supported Pt nanoparticles, for example, Lim and Wilcox report that defects in graphene, enhance the catalytic activity of the nanoparticles toward the interaction with molecular oxygen [48].

1.4 - EPR studies on graphite and graphene-like systems

Graphite has shown to be a semiconductor with zero band-gap [49,50]. One of the fundamental works on the magnetic properties of this material is an Electron Paramagnetic Resonance (EPR) work by Wagoner in the late 50's [51] on graphite single crystals, a quasi-ideal system with properties closely conforming to the theory. *Au contraire*, for non-ideal samples of graphitic materials these properties can vary, mostly due to defects.

Edge states, in particular, play an important role in determining the magnetic properties. They are associated to the limited extension of the crystals, being better observed in nanostructured materials [52]. These are non-bonding states localized at the Fermi level [53] and are responsible for the paramagnetic contribution to the magnetization [54].

The same type of defects is expected to play a role on graphene systems as well. Theoretical studies suggest that a crucial role in determining the magnetic properties of graphene is played by localized electron states, or defects [55], which infer anti/ferromagnetic properties to the materials.

The EPR technique is particularly convenient to study in detail the magnetic properties of graphitic and graphene-like materials, as it enables to distinguish the contributions from different paramagnetic species. It is rather surprising that the potentialities of this spectroscopy have not been fully exploited yet to study the properties of graphene and related materials. The seminal EPR paper on graphene has appeared in 2009 by L. Ćirić [56]. In that work, graphene sheets obtained by the scotch-tape technique were studied. The authors found a single Lorentzian line ($g = 2.0045$), with an intensity which varies with the temperature as expected for a zero gap semiconductor ($\chi \propto T$) for $T > 70$ K due to the thermal promotion of the electron from the valence to the conduction band. More publications on the topic followed, sometimes reporting contradictory results [57,58]; this is a clear indications that the studied systems are complex, and require the characterization of the nature of the *active sites* responsible for the macroscopic behaviour.

1.5 - Aim of the work

This PhD project has been mainly oriented to the study of different types of defects

that can be present in graphene-like materials by means of EPR techniques, continuous wave (cw) or pulsed and of DFT calculations.

The main part of this thesis is devoted to the EPR characterization of different materials. We focused mostly on graphite and graphene-like materials. In particular, we studied chemically expanded graphites, in collaboration with the group of Prof. Michele Maggini (Università degli studi di Padova) and graphene quantum dots in collaboration with the group of Prof. Stefano Agnoli (Università degli studi di Padova). Cw experiments at different frequencies and at different temperatures were used to determine the $\boldsymbol{g}$-tensors, the linewidths and the trends of the magnetic susceptibility with temperature of the various contributions to the EPR signals. The pulsed experiments instead enabled a characterization of the species, constituting the materials, from the point of view of the relaxation times (sequences of spin echo, inversion recovery) and the hyperfine coupling constants with magnetic nuclei (ESEEM and ENDOR experiments).
The spectroscopic analysis on the different available materials has been supported by theoretical and computational studies (based on DFT) in order to determine the EPR parameters for the different spin systems. We performed an accurate computational study on the $\boldsymbol{g}$-tensors of different molecular systems, that can be considered as fragments of graphene-like materials, in order to rationalize the dependence of the principal values of the tensor on their morphology. The aspect that we considered mostly is the variation of the $\boldsymbol{g}$-tensor because of the curvature effects in the graphene sheets. Where possible, the computational results have been correlated with results from experimental measurements. All the computational part of the thesis has been developed in collaboration with Prof. Matteo Tommasini (Politecnico di Milano).
In the last part of the thesis, we moved from the structural characterization of carbon materials to the study of the reactivity of defects. Defects strongly affect the chemical properties and reactivity of carbon-based materials, so we tried to correlate the nature and concentration of defects in some systems with their reactivity. We studied the catalytic activity of carbon-based material in a reaction of biological interest, the reaction of formation of reactive oxygen species. In this case, we could exploit EPR spectroscopy twice: first by characterize the carbon materials, as we did for all materials described in this thesis, and then by detect very reactive and short-living oxygen radicals by means of the spin-trapping techniques. That last part was done in collaboration with the group of Prof. Giuseppe Zerbi (Politecnico di Milano).

This thesis is organized as follows: in the first chapter a general introduction on graphene and on the defects that can occur in this material is given. The second chapter reports the basis of the EPR spectroscopy that are required to understand all the measurements reported in the following parts. In chapters 3, 4, 5 and 6 the work

done during my PhD is described. In chapter 3 and 4 are reported respectively the experimental characterizations of chemically expanded graphites and graphene quantum dots. Chapter 5 deals with the DFT study of the geometric effects on the $\boldsymbol{g}$-tensors of extended π-systems and chapter 6 with spin trapping study of the reactivity of defects. In the last chapter (7) a general discussion of all the results and the conclusions of the work are given.

References

[1] PR Wallace. The band theory of graphite, Physical Review. 71 (1947) 622.

[2] KS Novoselov, AK Geim, SV Morozov, D Jiang, Y Zhang, SV Dubonos, et al. Electric field effect in atomically thin carbon films, Science. 306 (2004) 666-669.

[3] S Stankovich, DA Dikin, GH Dommett, KM Kohlhaas, EJ Zimney, EA Stach, et al. Graphene-based composite materials, Nature. 442 (2006) 282-286.

[4] MC Lemme, TJ Echtermeyer, M Baus, H Kurz. A graphene field-effect device, arXiv preprint cond-mat/0703208. (2007).

[5] G Eda, G Fanchini, M Chhowalla. Large-area ultrathin films of reduced graphene oxide as a transparent and flexible electronic material, Nature nanotechnology. 3 (2008) 270-274.

[6] F Schedin, A Geim, S Morozov, E Hill, P Blake, M Katsnelson, et al. Detection of individual gas molecules adsorbed on graphene, Nature materials. 6 (2007) 652-655.

[7] RR Nair, HA Wu, PN Jayaram, IV Grigorieva, AK Geim. Unimpeded permeation of water through helium-leak-tight graphene-based membranes, Science. 335 (2012) 442-444.

[8] N Mohanty, V Berry. Graphene-based single-bacterium resolution biodevice and DNA transistor: interfacing graphene derivatives with nanoscale and microscale biocomponents, Nano letters. 8 (2008) 4469-4476.

[9] W Hu, C Peng, W Luo, M Lv, X Li, D Li, et al. Graphene-based antibacterial paper, Acs Nano. 4 (2010) 4317-4323.

[10] AK Geim, KS Novoselov. The rise of graphene, Nature materials. 6 (2007) 183-191.

[11] AA Balandin, S Ghosh, W Bao, I Calizo, D Teweldebrhan, F Miao, et al. Superior thermal conductivity of single-layer graphene, Nano letters. 8 (2008) 902-907.

[12] C Lee, X Wei, JW Kysar, J Hone. Measurement of the elastic properties and intrinsic strength of monolayer graphene, Science. 321 (2008) 385-388.

[13] P Sutter. Epitaxial graphene: How silicon leaves the scene, Nature Materials. 8 (2009) 171-172.

[14] PW Sutter, J Flege, EA Sutter. Epitaxial graphene on ruthenium, Nature materials. 7 (2008) 406-411.

[15] H Boehm, A Clauss, G Fischer, U Hofmann. Thin carbon leaves, Z Naturforsch. 17 (1962) 150-153.

[16] AM Panich, AI Shames, AE Aleksenskii, A Dideikin. Magnetic resonance evidence of manganese–graphene complexes in reduced graphene oxide, Solid State Commun. 152 (2012) 466-468.

[17] BS Paratala, BD Jacobson, S Kanakia, LD Francis, B Sitharaman. Physicochemical characterization, and relaxometry studies of micro-graphite oxide, graphene nanoplatelets, and nanoribbons, PLoS One. 7 (2012) e38185.

[18] DV Kosynkin, AL Higginbotham, A Sinitskii, JR Lomeda, A Dimiev, BK Price, et al. Longitudinal unzipping of carbon nanotubes to form graphene nanoribbons, Nature. 458 (2009) 872-876.

[19] F Tampieri, S Silvestrini, R Riccò, M Maggini, A Barbon. A comparative electron paramagnetic resonance study of expanded graphites and graphene, Journal of Materials Chemistry C. 2 (2014) 8105-8112.

[20] A Stone, D Wales. Theoretical studies of icosahedral C 60 and some related species, Chemical Physics Letters. 128 (1986) 501-503.

[21] L Li, S Reich, J Robertson. Defect energies of graphite: density-functional calculations, Physical Review B. 72 (2005) 184109.

[22] J Ma, D Alfe, A Michaelides, E Wang. Stone-Wales defects in graphene and other planar s p 2-bonded materials, Physical Review B. 80 (2009) 033407.

[23] MH Gass, U Bangert, AL Bleloch, P Wang, RR Nair, A Geim. Free-standing graphene at atomic resolution, Nature nanotechnology. 3 (2008) 676-681.

[24] MM Ugeda, I Brihuega, F Guinea, JM Gómez-Rodríguez. Missing atom as a source of carbon magnetism, Phys.Rev.Lett. 104 (2010) 096804.

[25] A Krasheninnikov, P Lehtinen, A Foster, R Nieminen. Bending the rules: contrasting vacancy energetics and migration in graphite and carbon nanotubes, Chemical Physics Letters. 418 (2006) 132-136.

[26] A El-Barbary, R Telling, C Ewels, M Heggie, P Briddon. Structure and energetics of the vacancy in graphite, Physical Review B. 68 (2003) 144107.

[27] MT Lusk, LD Carr. Nanoengineering defect structures on graphene, Phys.Rev.Lett. 100 (2008) 175503.

[28] F Banhart. Interactions between metals and carbon nanotubes: at the interface between old and new materials, Nanoscale. 1 (2009) 201-213.

[29] L Ci, L Song, C Jin, D Jariwala, D Wu, Y Li, et al. Atomic layers of hybridized boron nitride and graphene domains, Nature materials. 9 (2010) 430-435.

[30] D Boukhvalov, M Katsnelson. Chemical functionalization of graphene with defects, Nano letters. 8 (2008) 4373-4379.

[31] AH Nevidomskyy, G Csányi, MC Payne. Chemically active substitutional nitrogen impurity in carbon nanotubes, Phys.Rev.Lett. 91 (2003) 105502.

[32] K Wakabayashi, M Fujita, H Ajiki, M Sigrist. Electronic and magnetic properties of nanographite ribbons, Physical Review B. 59 (1999) 8271.

[33] D Bahamon, A Pereira, P Schulz. Inner and outer edge states in graphene rings: A numerical investigation, Physical Review B. 79 (2009) 125414.

[34] N Chakrapani, YM Zhang, SK Nayak, JA Moore, DL Carroll, YY Choi, et al. Chemisorption of acetone on carbon nanotubes, The Journal of Physical Chemistry B. 107 (2003) 9308-9311.

[35] M Grujicic, G Cao, A Rao, T Tritt, S Nayak. UV-light enhanced oxidation of carbon nanotubes, Appl.Surf.Sci. 214 (2003) 289-303.

[36] F Meng, L Zhou, S Shi, R Yang. Atomic adsorption of catalyst metals on Stone–Wales defects in carbon nanotubes, Carbon. 41 (2003) 2023-2025.

[37] S Picozzi, S Santucci, L Lozzi, L Valentini, B Delley. Ozone adsorption on carbon nanotubes: the role of Stone–Wales defects, J.Chem.Phys. 120 (2004) 7147-7152.

[38] L Zhou, S Shi. Adsorption of foreign atoms on Stone–Wales defects in carbon nanotube, Carbon. 41 (2003) 613-615.

[39] G Cantele, Y Lee, D Ninno, N Marzari. Spin channels in functionalized graphene nanoribbons, Nano letters. 9 (2009) 3425-3429.

[40] D Jiang, BG Sumpter, S Dai. Unique chemical reactivity of a graphene nanoribbon's zigzag edge, J.Chem.Phys. 126 (2007) 134701.

[41] D Boukhvalov, M Katsnelson. Chemical functionalization of graphene with defects, Nano letters. 8 (2008) 4373-4379.

[42] J Hahn, H Kang, S Lee, Y Lee. Mechanistic study of defect-induced oxidation of graphite, The Journal of Physical Chemistry B. 103 (1999) 9944-9951.

[43] SM Lee, YH Lee, YG Hwang, J Hahn, H Kang. Defect-induced oxidation of graphite, Phys.Rev.Lett. 82 (1999) 217.

[44] X Lu, Z Chen, PvR Schleyer. Are stone-wales defect sites always more reactive than perfect sites in the sidewalls of single-wall carbon nanotubes? J.Am.Chem.Soc. 127 (2005) 20-21.

[45] B Wang, Y Puzyrev, ST Pantelides. Strain enhanced defect reactivity at grain boundaries in polycrystalline graphene, Carbon. 49 (2011) 3983-3988.

[46] PA Denis, F Iribarne. Comparative study of defect reactivity in graphene, The Journal of Physical Chemistry C. 117 (2013) 19048-19055.

[47] BF Machado, P Serp. Graphene-based materials for catalysis, Catalysis Science & Technology. 2 (2012) 54-75.

[48] D Lim, J Wilcox. DFT-based study on oxygen adsorption on defective graphene-supported Pt nanoparticles, The Journal of Physical Chemistry C. 115 (2011) 22742-22747.

[49] C Coulson. Energy bands in graphite, Nature. 159 (1947) 265-266.

[50] P Wallace. The band theory of graphite, Physical Review. 71 (1947) 622.

[51] G Wagoner. Spin resonance of charge carriers in graphite, Physical Review. 118 (1960) 647.

[52] M Tommasini, C Castiglioni, G Zerbi, A Barbon, M Brustolon. A joint Raman and EPR spectroscopic study on ball-milled nanographites, Chemical Physics Letters. 516 (2011) 220-224.

[53] T Makarova, F Palacio, Carbon based magnetism: an overview of the magnetism of metal free carbon-based compounds and materials, Elsevier Science 2006.

[54] VY Osipov, A Shames, T Enoki, K Takai, M Endo, T Hayashi, et al. Magnetic and EPR studies of edge-localized spin paramagnetism in multi-shell nanographites derived from nanodiamonds, Diamond and Related Materials. 18 (2009) 220-223.

[55] R Nair, M Sepioni, I Tsai, O Lehtinen, J Keinonen, A Krasheninnikov, et al. Spin-half paramagnetism in graphene induced by point defects, Nature Physics. 8 (2012) 199-202.

[56] L Ćirić, A Sienkiewicz, B Nafradi, M Mionić, A Magrez, L Forro. Towards electron spin resonance of mechanically exfoliated graphene, physica status solidi (b). 246 (2009) 2558-2561.

[57] S Rao, A Stesmans, D Kosynkin, A Higginbotham, J Tour. Paramagnetic centers in graphene nanoribbons prepared from longitudinal unzipping of carbon nanotubes, New Journal of Physics. 13 (2011) 113004.

[58] HR Matte, K Subrahmanyam, C Rao. Novel magnetic properties of graphene: presence of both ferromagnetic and antiferromagnetic features and other aspects, The Journal of Physical Chemistry C. 113 (2009) 9982-9985.

CHAPTER 2 - ELECTRON PARAMAGNETIC RESONANCE

2.1 - Introduction

Electron Paramagnetic Resonance (EPR) spectroscopy studies the interaction between the spin magnetic moment of the electrons with the magnetic part of the electromagnetic radiation, usually in the microwave (mw) region (1 - 1000 GHz).
Each electron has a magnetic dipole moment that comes from its spin and orbital angular moments. Anyway, in most chemical systems, electrons are paired in such a way to cancel the total magnetic moment and the orbital moment is mostly quenched. Usually, only the species that have unpaired electrons have a non-zero magnetic dipole moment that can interact with the electromagnetic radiation. Therefore the species that can be studied with EPR are:

- organic radicals in solids or in solution
- organic molecules with more than one unpaired electron (biradicals, correlated radical pairs, triplet states, polyradicals)
- inorganic radicals, small paramagnetic molecules and isolated atoms
- transition metal ions
- natural systems in biological processes
- different types of punctual defects in solids
- systems with mobile charge carriers

Due to its intrinsic selectivity, EPR can give important information about the nature of paramagnetic centers, their environment and the dynamical processes in which they are involved. In this chapter, we describe some basic concepts of EPR technique useful to understand the experiments conducted in this thesis and reported in the following chapters. For more information on the EPR technique, you can refer to some more comprehensive textbooks [1-4].

2.2 - Free electron in a magnetic field

Electrons, like all elementary particles, are characterized by an intrinsic angular moment, which is called spin angular moment, to which, the operator $\widehat{\boldsymbol{S}}$ is associated. The component of $\widehat{\boldsymbol{S}}$, along the axes of an orthogonal reference system, are $\hat{S}_x$, $\hat{S}_y$ and $\hat{S}_z$.
The electron spin angular moment is characterized by the $S = 1/2$ quantum number; the eigenvalue of the operator $\widehat{\boldsymbol{S}}^2$ is $[s(s+1)]\hbar^2$ where $\hbar$ is the reduced Planck

constant ($\hbar = h/2\pi$ =1.055·10^{-34} J s). The eigenvalues of the operator $\hat{S}_z$, corresponding to the spin component along z are $1/2$ and $-1/2$. Thus, the eigenstates of the operators $\widehat{\boldsymbol{S}}^2$ and $\hat{S}_z$ can be written as $|1/2,\ 1/2\rangle$ and $|1/2,\ -1/2\rangle$ and are typically labelled with the Greek letters α and β respectively. The two states α and β are degenerate if no magnetic field is applied.

We can always associate a magnetic moment $\boldsymbol{\mu^e}$ to the spin angular moment, the two vectors are parallel with each other but they point toward opposite directions

$$\widehat{\boldsymbol{\mu}}^e = -g_e\beta_e\widehat{\boldsymbol{S}} \tag{2.1}$$

where $g_e = 2.0023$ is the g-factor for the free electron and β_e is the Bohr magneton that is defined as $\beta_e = e\hbar/2m_e$ with e = 1.602·10^{-19} C electron charge and m_e = 9.109·10^{-31} kg electron mass. The component of the magnetic moment along z can be written as follows

$$\hat{\mu}_z^e = -g_e\beta_e\hat{S}_z \tag{2.2}$$

since g_e and β_e are constant, the eigenfunctions of the operator $\hat{\mu}_z^e$ are the same of the operator $\hat{S}_z$. The eigenvalues are

$$\mu_z^e = \mp 1/2\hbar g_e\beta_e \tag{2.3}$$

where the − sign is referred to the α state and the + sign to the β state.

If the electron is placed inside a static magnetic field $\boldsymbol{B}_0$, the α and β states are no more degenerate, but they have different energies because of the interaction of the spin magnetic moment with the applied magnetic field (Figure 2.1). This is the electron Zeeman interaction and can be described by the following Hamiltonian operator (we assume that the applied magnetic field is along z, $\boldsymbol{B}_0 = B_0\boldsymbol{z}$)

$$\widehat{\mathcal{H}}^Z = -\widehat{\boldsymbol{\mu}}^e \cdot \boldsymbol{B}_0 = g_e\beta_e\widehat{\boldsymbol{S}} \cdot \boldsymbol{B}_0 = g_e\beta_e B_0\hat{S}_z \tag{2.4}$$

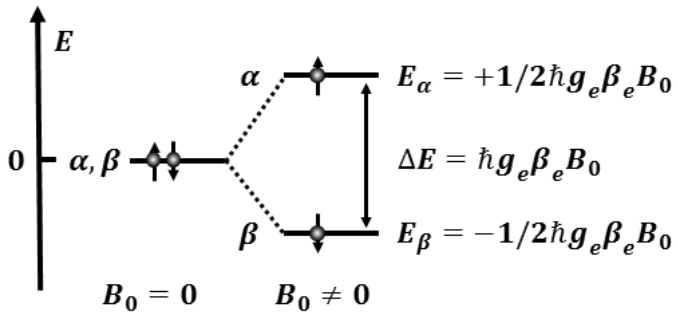

Figure 2.1 Separation in energy of the α and β states due to the Zeeman interaction between the spin magnetic moment and the applied magnetic field $\boldsymbol{B}_0$.

The eigenvalues associated to the α and β states are

$$E = \pm 1/2 \hbar g_e \beta_e B_0 \tag{2.5}$$

where the $+$ sign refers to the α state and the $-$ sign to the β state, that is consequently lower in energy. The energy difference between the two states, due to the Zeeman interaction, is proportional to the magnetic field and its value is:

$$\Delta E = E_\alpha - E_\beta = \hbar g_e \beta_e B_0 \tag{2.6}$$

If the two spin levels are different in energy, an electron in the β state can absorb a photon with energy equal to the energy difference between the two states and be promoted to the higher energy state. In the same way, an electron in the α state can expell a photon and go to the lower energy level. The frequency needed to have these transitions (Larmor Frequency, ν_0) can be obtained using the Planck relation ($\Delta E = h\nu$) with the equation 2.6. The Larmor frequency is

$$\nu_0 = \frac{g_e \beta_e B_0}{2\pi} \tag{2.7}$$

In a 3.5 T magnetic field (standard magnetic field used in most EPR spectrometers), Equation 2.7 gives 9.5 GHz; this value is in the microwave frequency region called X-band (8-12 GHz).

We can show [4] that, in order to have a transition between the two spin states, the oscillating magnetic field $\boldsymbol{B}_1$, associated to the mw radiation, must have a non-zero component in the xy plane, perpendicular to the direction of $\boldsymbol{B}_0$.

There are in principle two ways to conduct a continuous wave (cw) EPR experiment: in the first, the magnetic field $\boldsymbol{B}_0$ is kept constant during the experiment and the mw frequency is swept. We have resonance, and therefore EPR signal, when the mw frequency fulfills Equation 2.7. The second way, that is used in most EPR experiments, for instrumental reasons, implies that the mw radiation is kept constant (ν_0) and that the magnetic field is swept linearly. In this case, we have resonance when Equation 2.7 is fulfilled too.

2.3 - The g-tensor

2.3.1 - Electrons in molecules

Until now, we considered isolated electrons. Within atoms and molecules, the magnetic moment of each electron comes from two contributions: the contribution arising from the spin angular moment, already described in the previous section, and

the contribution due to the orbital motion of the electron around the nucleus

$$\widehat{\boldsymbol{\mu}}^{e} = \widehat{\boldsymbol{\mu}}^{e,orb} + \widehat{\boldsymbol{\mu}}^{e,spin} = -\beta_e \hat{\boldsymbol{L}} - g_e \beta_e \widehat{\boldsymbol{S}} = -\beta_e (\hat{\boldsymbol{L}} + g_e \widehat{\boldsymbol{S}}) \tag{2.8}$$

$\hat{\boldsymbol{L}}$ is the orbital angular moment operator. The eigenvalues of the operator $\hat{\boldsymbol{L}}^2$ are $[l(l+1)]\hbar^2$ where l is an integer quantum number, that can be positive or equal to zero and that depends on the spatial wavefunction of the electron. The eigenvalues of the operator $\hat{L}_z$ are the $2l+1$ terms with values $m_l\hbar$ where m_l is an integer quantum number that goes from $-l$ to $+l$. Within an atom, the orbital and spin angular moments are not independent, but they interact. This interaction is called spin-orbit interaction and can be written as

$$\widehat{\mathcal{H}}^{so} = \lambda \hat{\boldsymbol{L}} \cdot \widehat{\boldsymbol{S}} = \lambda \left[\hat{L}_x \hat{S}_x + \hat{L}_y \hat{S}_y + \hat{L}_z \hat{S}_z \right] \tag{2.9}$$

where λ is the spin-orbit coupling constant and depends on the atomic number of the element that is considered to the fourth. The Hamiltonian operator of an electron, in an atom or a molecule is the sum of the Zeeman term and of the spin-orbit interaction term

$$\widehat{\mathcal{H}} = \widehat{\mathcal{H}}^{Z} + \widehat{\mathcal{H}}^{so} = \beta_e \left(\hat{\boldsymbol{L}} + g_e \widehat{\boldsymbol{S}} \right) \cdot \boldsymbol{B}_0 + \lambda \hat{\boldsymbol{L}} \cdot \widehat{\boldsymbol{S}} \tag{2.10}$$

The Hamiltonian operator 2.10 is not a pure spin Hamiltonian, since it contains also operators that act on spatial variables. It's possible, with some math [4], starting from equation 2.10, to obtain a new Hamiltonian that depends only on the spin angular operator $\widehat{\boldsymbol{S}}$

$$\widehat{\mathcal{H}} = \beta_e \widehat{\boldsymbol{S}} \cdot \boldsymbol{g} \cdot \boldsymbol{B}_0 \tag{2.11}$$

in this case $\boldsymbol{g}$ is a symmetrical tensor (that can be represented by a 3x3 matrix) and contains the dependence on the spatial variables

$$\boldsymbol{g} = \begin{pmatrix} g_{xx} & g_{xy} & g_{xz} \\ g_{yx} & g_{yy} & g_{yz} \\ g_{zx} & g_{zy} & g_{zz} \end{pmatrix} = g_e \mathbf{1}_3 + 2\lambda \boldsymbol{\Lambda} \tag{2.12}$$

where $\mathbf{1}_3$ is the 3x3 identity matrix. The elements of tensor $\boldsymbol{\Lambda}$ are

$$\Lambda_{ij} = -\sum_{n' \neq n} \frac{\langle 0 | \hat{L}_i | n \rangle \langle n | \hat{L}_j | 0 \rangle}{E_n - E_0} \tag{2.13}$$

with $|0\rangle$, $|n\rangle$, E_0 and E_n spatial wavefunction and energies relative to the ground

state and the n-th excited state. The elements g_{ij} of the $\boldsymbol{g}$-tensor depend on the reference system. However, since the tensor is symmetric with respect of the diagonal ($g_{ij} = g_{ji}$), it's always possible to find a particular reference system XYZ in which all the elements of the tensor are equal to zero if $i \neq j$. The axes X, Y, Z are called principal axes and the corresponding tensor elements g_X, g_Y and g_Z are called principal values.

2.3.2 - Anisotropy of the $\boldsymbol{g}$-tensor

The local symmetry of the center that contains the unpaired electron is of paramount importance in the determination of the $\boldsymbol{g}$-tensor principal values (and of any other tensor that describes other parameters, which are dependent on the orientation of the sample with respect to the magnetic field). There are three possibilities.

1. *Cubic symmetry*: In this case, there is no anisotropy of any EPR properties; the principal values of the $\boldsymbol{g}$-tensor are equal ($g_X = g_Y = g_Z$).
2. *Uniaxial symmetry (or axial)*: in this case, there is linear rotational symmetry (at least three-fold) about a unique axis contained in each paramagnetic species. Anisotropy is observable unless the field $\boldsymbol{B}_0$ lies in the plane perpendicular to the unique axis. If the symmetry axis is along the principal direction Z the two principal values perpendicular to it coincide ($g_X = g_Y = g_\perp$) and differ from the third value parallel to the axis ($g_Z = g_\parallel$).
3. *Rhombic symmetry (or orthorhombic)*: this is the general case, implying anisotropy for all rotations and the presence of three unequal principal values in each parameter matrix ($g_X \neq g_Y \neq g_Z$).

To determine the principal values and principal directions of the $\boldsymbol{g}$-tensor, measurements on single crystal are necessary. In a single crystal, all the paramagnetic centers have the same orientation with respect of the external magnetic field. A single crystal spectrum, if there are no couplings with paramagnetic nuclei or other particular effects, is a single line that moves to different field according to the orientation of the crystal (Fig. 2.2). When the crystal is rotated, inside the EPR spectrometer, in such way that one of the principal directions of $\boldsymbol{g}$ becomes parallel to the field $\boldsymbol{B}_0$ the line has a g-factor equal to the principal values related to that direction.

The dependence of the observed g-factor on the orientation of the paramagnetic center with respect to the magnetic field can be obtained from 2.11 and is

$$g(\theta,\varphi) = \sqrt{\sin^2\theta \cdot \cos^2\varphi \cdot g_X^2 + \sin^2\theta \cdot \sin^2\varphi \cdot g_Y^2 + \cos^2\theta \cdot g_Z^2} \qquad (2.14)$$

where θ and φ are polar angles that are needed to describe the orientation of $\boldsymbol{B}_0$

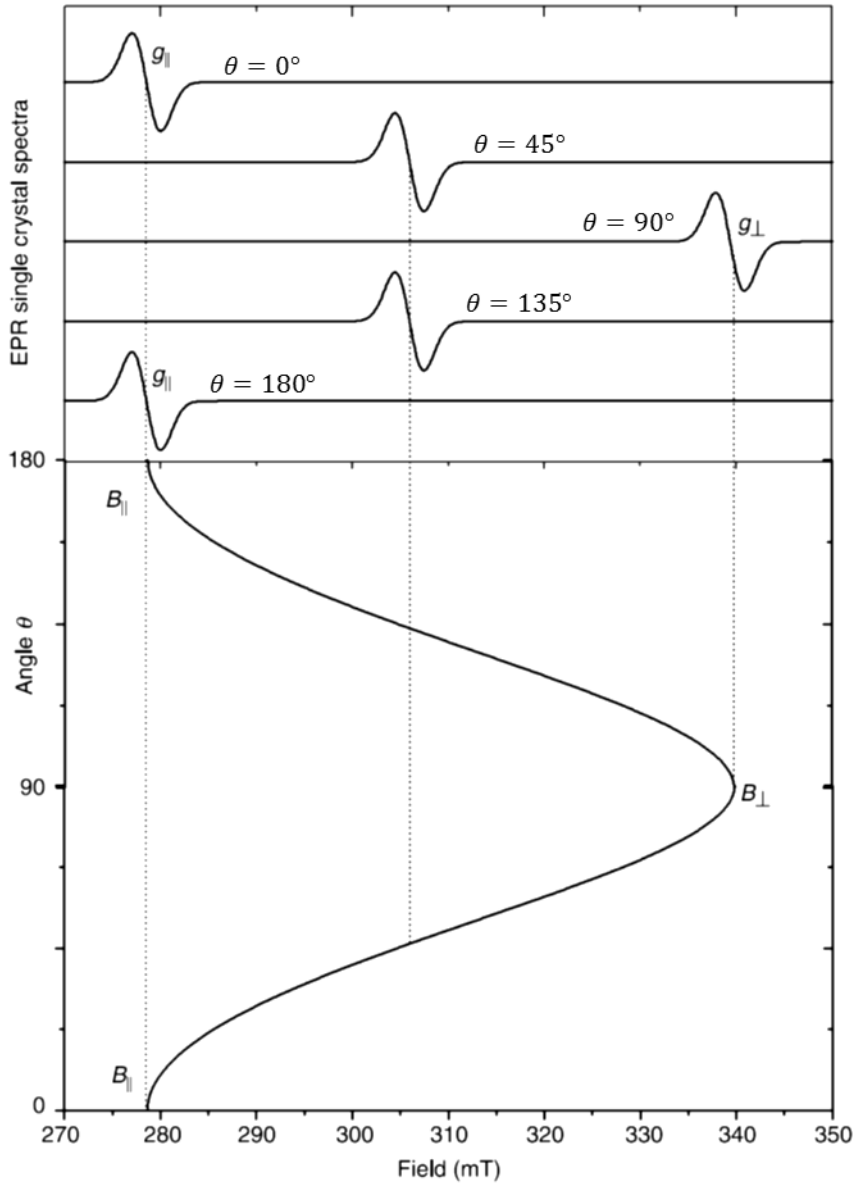

Figure 2.2 Simulated EPR profile for a single crystal with paramagnetic centers $s = 1/2$ and axial symmetry. If the crystal is rotated with respect to the magnetic field, the position of the EPR line changes. In the lower part is represented the angular dependence of the line position, this dependence can be obtained from 2.14 if $\varphi = 0$, $g_X = g_Y = g_\perp$and $g_Z = g_\parallel$.

with respect of the principal directions of the $\boldsymbol{g}$-tensor.

If we have powder spectra, i. e. radicals in polycrystalline or glassy samples, the EPR spectrum is the sum of the contributions of all the molecules, each in its specific orientation with respect to the applied magnetic field. Each paramagnetic center has its own resonance field that is dependent on the orientation; therefore, the powder spectrum that results is generally wide since it is obtained from the envelope that represents a weighted distribution of all possible resonance fields.

From a powder spectrum, it is possible to obtain the $\boldsymbol{g}$-tensor principal values, but not the principal directions. If we have a system with axial symmetry (Fig. 2.3) the

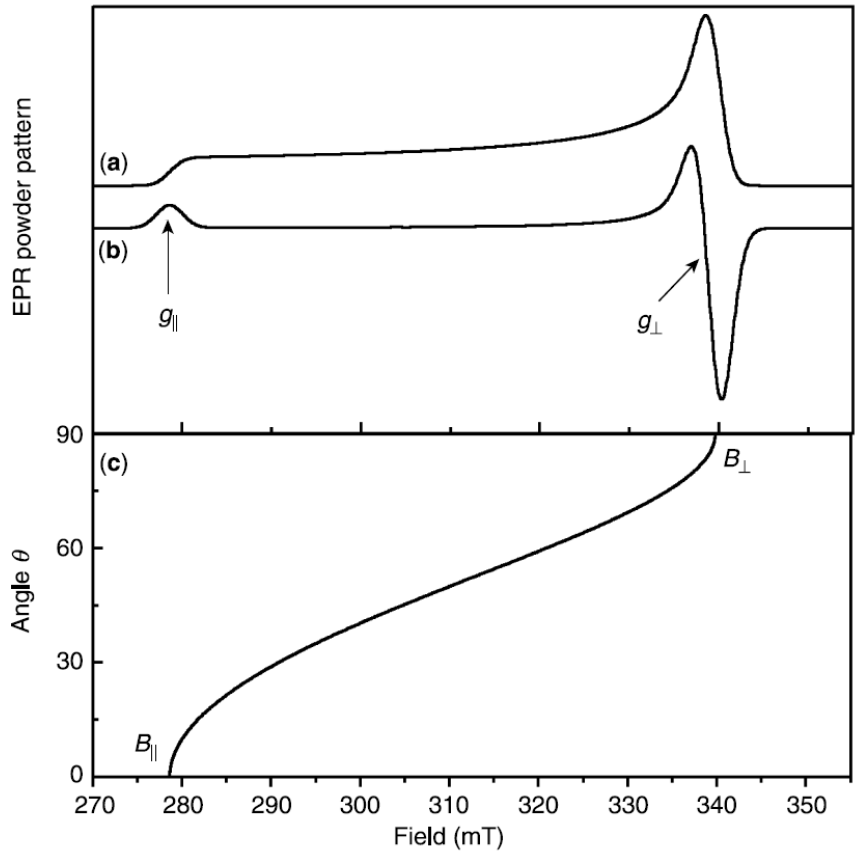

Figure 2.3 Absorption (a) and derivative (b) EPR spectrum of a spin system ($s = 1/2$) oriented randomly with respect to the applied magnetic field with axial symmetry ($g_{\parallel} > g_{\perp}$). (c) resonance field as function of the θ angle between the symmetry axis and the magnetic field.

values $g_{\perp}$ and $g_{\parallel}$ define the field range inside of which the resonance occurs. Only few spins are oriented in such a way to have their symmetry axis parallel to the external field, so in the spectrum a minimum is observed at a field corresponding to $g_{\parallel}$. At the field value, corresponding to $g_{\perp}$ there is a maximum because there are many spins with their symmetry axis perpendicular to the magnetic field.

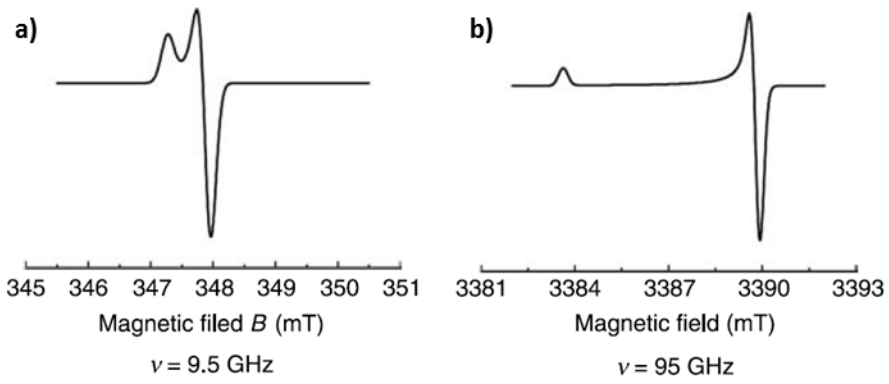

Figure 2.4 Powder EPR spectra of a sample with axial paramagnetic centers measured (a) with a X-band ($\nu = 9.5$ GHz) and (b) with a W-band ($\nu = 95$ GHz) spectrometer.

If the anisotropy of the $\boldsymbol{g}$-tensor is small, as the case of most organic radicals, its effects on the EPR line can be hidden by the linewidth. In this case, to resolve better the anisotropy, it is useful to use spectrometers that work with higher frequencies with respect to X-band (Fig. 2.4).

2.3.3 – Simulation of cw-EPR spectra

In a powder spectrum, the intensity at a given field is due to the superposition of all components resonating at the field, or close to that field. In the presence of a randomly distributed paramagnetic species with an anisotropic $\boldsymbol{g}$-tensor and negligible hyperfine interaction, the spectrum is given by the relation:

$$I(B) \propto \int_0^{4\pi} \left[f\left(B - B_0(\Omega)\right) \right] d\Omega \tag{2.15}$$

where B_0 is the resonance fields which depends on the angle Ω between the $\boldsymbol{g}$-tensor axes and the field direction. In the presence of more than one species, one has to sum all the spectra as:

$$I(B) \propto \sum_i c_i \int_0^{4\pi} \left[f_i\left(B - B_0(\Omega)\right) \right] d\Omega \tag{2.16}$$

the coefficients c_i determine the relative contribution of each spin packet.

2.4 - Macroscopic magnetization, relaxation and lineshapes

In typical EPR experiments, the samples have many electron spins (about 10^{10} or more). It is convenient to define the vector macroscopic magnetization $\boldsymbol{M}$ as the total magnetic moment per unit volume

$$\boldsymbol{M} = \frac{1}{V} \sum \boldsymbol{\mu}^e \tag{2.17}$$

At thermal equilibrium, without an applied magnetic field, half of the total spins is in the α state and half in the β state, since the two states are degenerate. They can be depicted as vectors lying on the surface of a cone with axis parallel to z, with apothem equal to $[s(s+1)]^{1/2}$ and heith equal to m_s. $\boldsymbol{M}$ is equal to zero because each spin has a random orientation in the xy plane (Fig. 2.5a).
If a magnetic field $\boldsymbol{B}_0$, parallel to the z, axis is applied, the two states are no more degenerate and they are populated according to the Boltzman law [5]; each magnetic moment, moreover, start to precede around the direction of the external magnetic

field with angular frequency $\omega_0 = g_e \beta_e B_0$ (Larmor) and random phase. In this case (Fig. 2.5b) the equilibrium magnetization M_0 is proportional to the population difference between the two states and has the same direction of the magnetic field

$$M_x = M_y = 0 \qquad\qquad M_z = M_0 \tag{2.18}$$

If the system is perturbed, in presence of an external magnetic field, the M_z component tends to restore the equilibrium value M_0 with an exponential trend characterized by the time constant T_1 that is called longitudinal relaxation time or spin-lattice relaxation time. That time constant is typical of energy transfer processes between the spin system and the lattice. The components of the magnetization perpendicular to the external field M_x and M_y precede around its direction at the Larmor frequency and their values tend to become equal to zero with an exponential trend characterized by the time constant T_2 called transverse relaxation time or spin-spin relaxation time. This time constant is typical of energy transfer processes that happen within the spin system. The time variation of the magnetization components, if we consider the relaxation processes, can be expressed by the following equations

$$\frac{\partial M_z}{\partial t} = -\frac{M_z - M_0}{T_1} \tag{2.19a}$$

$$\frac{\partial M_{x,y}}{\partial t} = -\frac{M_{x,y}}{T_2} \tag{2.19b}$$

To better follow the evolution of the magnetization, if a mw field $\boldsymbol{B}_1$ is applied to the system, it's convenient to use a new reference system (XYZ) that rotates with respect to the laboratory reference system (xyz) with frequency ω_{mw}. We suppose that one of the axes of the new reference system coincides with one of the old (for

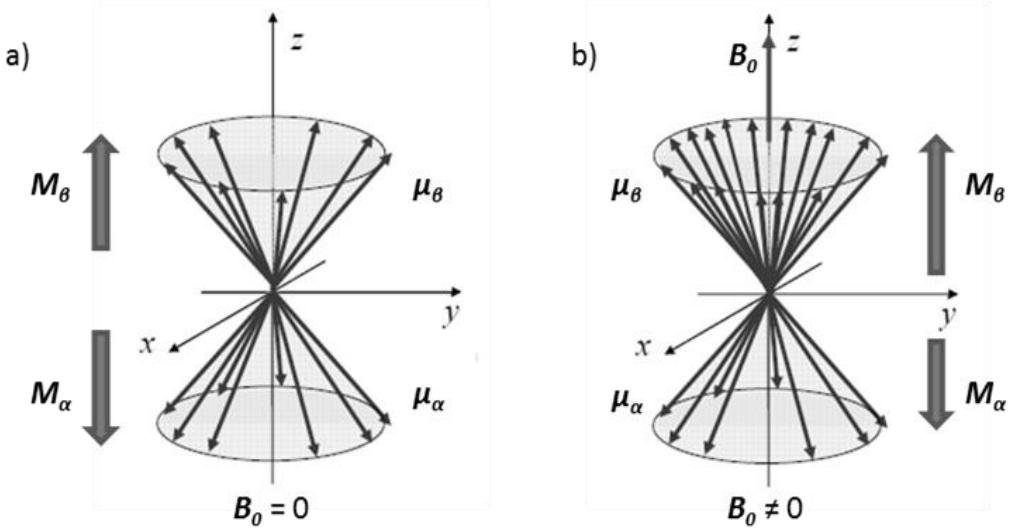

Figure 2.5 Spin magnetic moments of an ensemble of electrons without (a) and with (b) an external magnetic field applied along z.

convenience $Z \equiv z$). If $\boldsymbol{B}_1$ is applied in the XY plane of the rotating system (for convenience along X) the effective field experienced by the spins in the rotating reference system is no more $\boldsymbol{B}_0$ (Fig. 2.6), but

$$\boldsymbol{B}_{eff} = \boldsymbol{B}_1 + \left[\boldsymbol{B}_0 - \frac{\boldsymbol{\omega}_{mw}}{g_e\beta_e}\right] = \boldsymbol{B}_1 + \frac{1}{g_e\beta_e}[\boldsymbol{\omega}_0 - \boldsymbol{\omega}_{mw}] = \boldsymbol{B}_1 + \frac{\boldsymbol{\Omega}}{g_e\beta_e} \qquad (2.20)$$

If the rotating reference system rotates with angular frequency equal to the Larmor frequency ($\omega_{mw} = \omega_0$, resonance condition) the effective magnetic field coincides with the mw field and consequently the magnetization precedes around $\boldsymbol{B}_1$ (therefore around X) with frequency equal to $\omega_1 = g_e\beta_e B_1$.
The behavior of the magnetization vector, in presence of an external magnetic field, of a mw field and of relaxation processes can be described and rationalized using the Bloch equations [1,2,4]. By solving them we can obtain the magnetization components in the rotating reference system as function of the rotation frequency of the mw field ω_{mw}:

$$M_X = M_0 \frac{T_2^2(\omega_0 - \omega_{mw})}{1 + T_2^2(\omega_0 - \omega_{mw})^2} g_e\beta_e B_1 \qquad (2.21a)$$

$$M_Y = M_0 \frac{T_2}{1 + T_2^2(\omega_0 - \omega_{mw})^2} g_e\beta_e B_1 \qquad (2.21b)$$

$$M_Z = M_0 \frac{1 + T_2^2}{1 + T_2^2(\omega_0 - \omega_{mw})^2} \qquad (2.21c)$$

The classical EPR spectrometers detect the components of the magnetization in the xy plane of the laboratory reference system.
The magnetization in most materials (linear materials) is directly proportional to the applied magnetic field, unless the material has some degree of magnetic order. The proportionality constant is the magnetic suceptivity χ

$$\boldsymbol{M} = \chi \boldsymbol{B} \qquad (2.22)$$

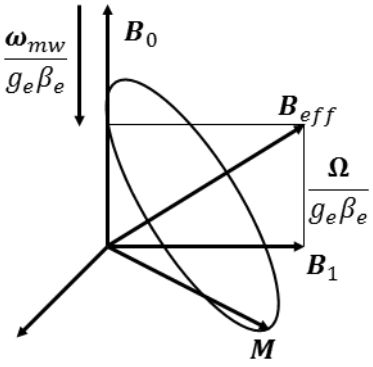

Figure 2.6 Effective magnetic field experimented by the spins in the rotating reference system as vector sum of field $\boldsymbol{B}_1$ and of the residual field along z

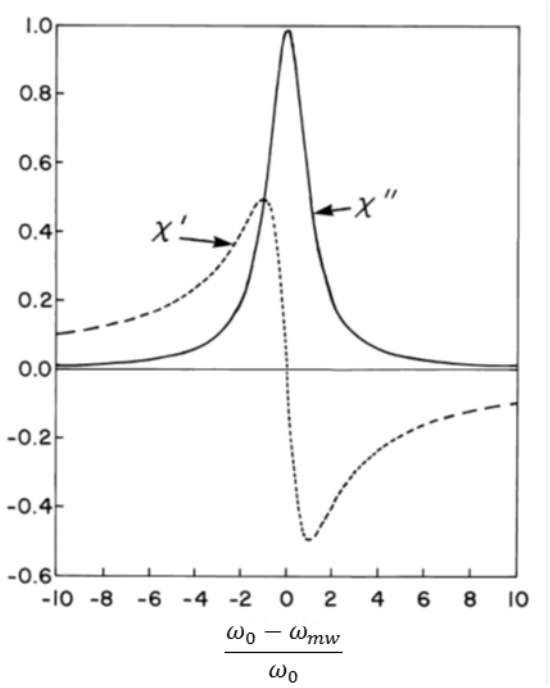

Figure 2.7 Real and imaginary part of the magnetic susceptivity as function of the frequency of the mw field.

It is useful to write the transverse magnetization $M_\perp$ and the magnetic susceptivity χ as complex quantities [4]:

$$M_\perp = M_X + iM_Y \tag{2.23a}$$
$$\chi = \chi' + i\chi'' \tag{2.23b}$$

By combining these expressions with 2.21a and 2.21b, and using 2.22 we obtain:

$$\chi' = \frac{M_0 g_e \beta_e}{2} \frac{T_2^2(\omega_0 - \omega_{mw})}{1 + T_2^2(\omega_0 - \omega_{mw})^2} \tag{2.24a}$$
$$\chi'' = \frac{M_0 g_e \beta_e}{2} \frac{T_2}{1 + T_2^2(\omega_0 - \omega_{mw})^2} \tag{2.24b}$$

The real part of the susceptivity has the same phase of $\boldsymbol{B}_1$ expressed in the rotating reference system; the imaginary part is 90° out of phase. The two components are depicted in Figure 2.7.

The curve $\chi''(\omega)$ is called absorption curve and has Lorentzian lineshape, the maximum of the curve correspond to the resonance. $\chi'(\omega)$ is the dispersion curve; in this case we have resonance in correspondence of the point that cross the abscissa axis. Usually, during the EPR experiments we record the absorption curve. We can experimentally obtain the EPR spectra as function of the mw frequency are with pulsed techniques. Most of the EPR is done in continuous wave; in this case, it is practically impossible to scan the frequencies because of the small bandwidths of the

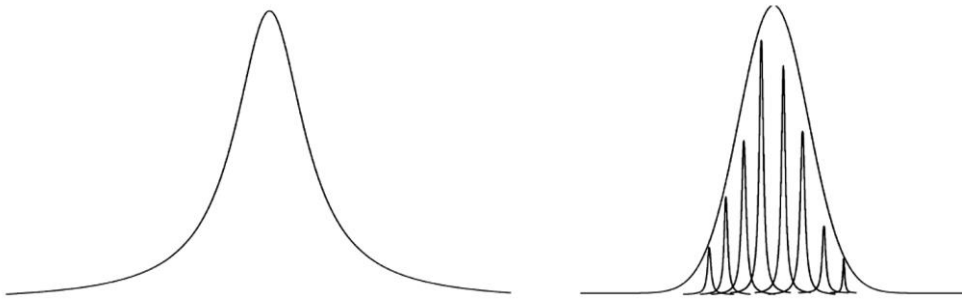

Figure 2.8 Homogeneously broadened line with Lorentzian shape (left) and inhomogenuously broadened line with Gaussian shape (right). The Gaussian line is the convolution of homogeneous lines.

resonators that are commonly used. In cw-EPR, the spectra are recorded as function of the magnetic field, keeping the mw frequency fixed. The signal is recorded using a lock-in amplifier, so the signals are recorded in derivative form. For systems that can be described by a pure Zeeman Hamiltonian operator, the magnetic field and the mw frequency are directly proportional. A parameter that can be easily obtained from an EPR spectrum is the linewidth, that is inversely proportional to the relaxation time T_2.

Lorentzian lineshape are observed when all spins in the system have the same resonance frequency. In this case, we have an homogeneous broadening. Often the EPR lines are sums of different unresolved contributions; in this case, we have an inhomogeneous broadening and the lineshape in Gaussian (Fig. 2.8).

Some possible reasons that imply an inhomogeneous broadening are the following:

1. Non homogeneous external magnetic field
2. Unresolved hyperfine structure (see section 2.6)
3. Anisotropic interactions, solid systems randomly oriented with respect to the magnetic field (see section 2.3.2)
4. Dipolar interaction with other paramagnetic centers

Systems containing mobile charge carriers show generally an asymmetric lineshape that is called Dysonian [6]. It will be explained better in the following.

2.5 - EPR spectroscopy of systems with conduction electrons

Most of EPR experiments are conducted on samples in which the unpaired electrons are localized on single atoms or small groups of atoms. Anyway, also conductive systems show an EPR signal (Conduction Electron Spin Resonance, CESR [2]). These systems have electrons that can be considered as free and that are delocalized over the whole sample. That affects strongly the resonance signal.

2.5.1 - EPR lineshape for systems with conduction electrons

EPR spectra of conductive system have a single line with an asymmetrical shape, low intensity, if compared with the usual values measured for localized electrons and no hyperfine interaction with paramagnetic nuclei. The lineshape for this kind of systems is called Dysonian by Freeman Dyson who studied and rationalized it first [6]. An exemplum is reported in Figure 2.9. The asymmetry of the CESR lines is due to the impossibility of the mw radiation to penetrate fully the conductive systems. Indeed, only a small portion of a conductive sample feels the mw radiation, so not all the spins experience the same magnetic field. This effect is called skin effect. The penetration depth δ of the mw inside a conductive sample is

$$\delta = \left(\frac{c^2 \varepsilon_0 \rho}{\pi \nu}\right)^{1/2} \tag{2.25}$$

c is the speed of light in vacuum, ε_0 is the vacuum permittivity, ρ is the electrical resistivity of the sample and ν is the radiation frequency. Only the part of the sample that is localized at a depth less of δ from the surface feels the mw radiation.

We have to keep in mind that electrons in conductive systems are mobile; they can enter and exit the layer in which the mw radiation can penetrate. The theory that enable to obtain the CESR lineshape was developed by Dyson [6] and experimentally proven by Feher and Kip [7]. The principal parameters that they used are the time that one electron needs to diffuse across the skin depth (T_D), the spin-spin relaxation time (T_2) and the time that an electron needs to cross the whole sample (T_T). There

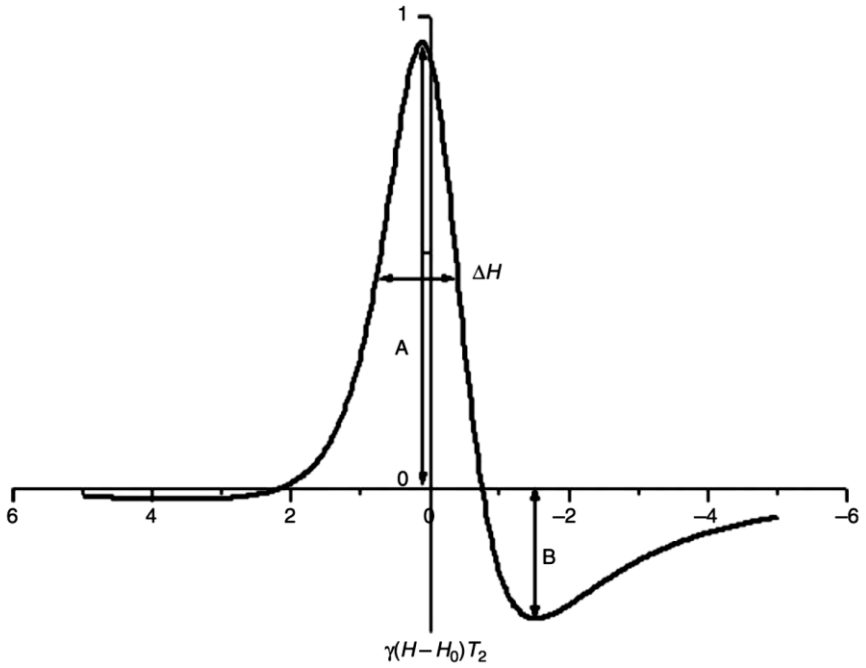

Figure 2.9 Dysonian lineshape, observable by recording the EPR spectra of conductive samples. The ratio A/B describes the asimmetry of the line. ΔH is the linewidth.

are two limiting situations:

1. Samples with smaller size than the skin depth. In this case $T_T \ll T_D$, the whole sample feels a uniform mw field and the EPR lineshape is Lorentzian with linewidth that depends on the invers of the relaxation time T_2.
2. Samples with size larger or comparable to the skin depth. The electrons experience a different field if they are inside or outside the skin region. The resonance signal is asymmetric; the ratio A/B that describes the asymmetry (see Figure 2.9) is related to the ratio T_D/T_2. If g and T_2 are fixed, the lineshape and linewidth depend on the sample thickness.

If the sample size is much larger with respect of the skin depth and the spin diffusion velocity is slow enough we have $T_T \gg T_D$, $T_T \gg T_2$ and $T_D/T_2 \gg 1$. This situation is typical of graphite single crystals [8]. The derivative of the absorbed power is

$$\frac{dP}{d\omega} = \frac{\omega H_1^2}{2}\left(\frac{\delta A}{2}\right)\frac{\chi_0 \omega_0 T_2^2}{4}\frac{[1 - 2T_2(\omega_0 - \omega) - T_2^2(\omega_0 - \omega)^2]}{[1 + T_2^2(\omega_0 - \omega)^2]^2} \qquad (2.26)$$

ω is the mw radiation frequency, ω_0 the resonance frequency, H_1 is the amplitude of the magnetic component of the mw radiation, χ_0 is the Pauli paramagnetic susceptivity, δ is the skin depth and A is the surface area of the sample.

2.5.2 - EPR intensity for conductive systems

The conduction electrons can be considered as a Fermi gas. The alignment of magnetic moments with the external magnetic field is opposed not only by the thermal energy as for the isolated and independent electrons, but we also have to be sure that the Pauli principle is fulfilled. Therefore, the electron gas must obey to the Fermi-Dirac statistics [9]; consequently, the electrons that can be measured in a CESR experiment are those with energy near to the Fermi level. The others do not contribute. For this reason, the CESR spectra are usually less intense, regardless the number of electrons in the sample. The Fermi-Dirac statistic determines also the type of magnetism of these systems.

A solid that contains an ensemble of unpaired, non-interacting spins obeys to the Maxwell-Boltzmann statistic and its magnetic susceptivity obeys the Curie law [9,10]

$$\chi = \frac{N_V \mu^2}{3k_T T}\mu_0 = \frac{C}{T} \geq 0 \qquad (2.27)$$

where $\mu^2 = g^2 {\beta_e}^2 S(S+1)$ and N_V is the number of magnetic species per unit volume. C is the Curie constant and is characteristic of each paramagnetic substance through μ. Usually, real solids do not obey exactly the Curie law; often the

dependence of the magnetic susceptivity from the temperature has the following form

$$\chi = \frac{C}{T - \theta} \tag{2.28}$$

this is the Curie-Weiss law and the parameter θ, the Weiss temperature, depends on the specific material and it is positive for materials that have a ferromagnetic behavior and negative for antiferromagnetic materials. The Curie-Weiss law comes as direct consequence of the dipolar magnetic interaction between the spin in the materials.
Conductive systems have a magnetic suceptivity that is lower in module with respect to the systems with localized electrons and it doesn't depend on the temperature; in this case we have the Pauli paramagetism [9,10]

$$\chi_{Pauli} = \frac{3n_0{\beta_e}^2}{2\varepsilon_F} \tag{2.29}$$

ε_F is the Fermi energy and n_0 is the total number of electrons per unit volume that occupy the levels up to the one with maximum energy (that for $T = 0$ corresponds to ε_F).

2.6 - Hyperfine interaction

The nuclei, as the electrons, have a spin angular moment that is described by the operator $\hat{\boldsymbol{I}}$, that obeys the same rules of the electron spin angular moment described in section 2.2. The magnetic moment associated to the nuclear spin angular moment is

$$\hat{\boldsymbol{\mu}}^n = g_n\beta_n\hat{\boldsymbol{I}} \tag{2.30}$$

g_n is the nuclear g-factor and depends on the specific isotope and β_n is the nuclear magneton, defined as $\beta_n = e\hbar/2m_p$ with $m_p = 1.673{\cdot}10^{-27}$ kg, proton mass. As for electron spins, the energy of nuclear spins depends on the presence of external magnetic fields, in this case we have the nuclear Zeeman interaction between the nuclear spin magnetic moment and the magnetic field.
If we have nuclear spins in our system, the electron spin feels both the applied magnetic field and the local fields induced by the nuclei magnetic moments that modify the resonance conditions. This interaction between nuclear and electron spin magnetic moments is called hyperfine interaction. The hyperfine interaction causes the EPR line to be separated into $2i + 1$ lines. i is a quantum number that depends

on the nucleus.
If we have a system with more than one paramagnetic nuclei, we must add two terms to the Hamiltonian 2.11 for each nucleus. Those terms describe the hyperfine interaction and the nuclear Zeeman interaction. The Hamiltonian operator becomes

$$\widehat{\mathcal{H}} = \beta_e \widehat{\boldsymbol{S}} \cdot \boldsymbol{g} \cdot \boldsymbol{B_0} + \sum_i (g_N^i \mu_N \, \widehat{\boldsymbol{I}}^{\boldsymbol{i}} \cdot \boldsymbol{B_0} + \widehat{\boldsymbol{I}}^{\boldsymbol{i}} \cdot \boldsymbol{A}^{\boldsymbol{i}} \cdot \widehat{\boldsymbol{S}}) \tag{2.31}$$

$\boldsymbol{A}^i$ is the hyperfine coupling tensor of the i-th nucleus with the electron. It has two contributions: an isotropic one due to the Fermi contact term and an anisotropic one due to the dipolar coupling between the electron and nuclear spins. It can be written as follows

$$\boldsymbol{A} = \begin{pmatrix} A_{xx} & A_{xy} & A_{xz} \\ A_{yx} & A_{yy} & A_{yz} \\ A_{zx} & A_{zy} & A_{zz} \end{pmatrix} = a_{iso} \mathbf{1}_3 + \boldsymbol{T} \tag{2.32}$$

The first term of the 2.32 is the isotropic one; a_{iso} is the hyperfine coupling constant, it is a scalar number and depends on the non-zero probability to have spin density on the nucleus. It can be written as

$$a_{iso} = (8\pi/3) g \beta_e g_n \beta_n |\Psi(0)|^2 \tag{2.33}$$

where $\Psi(0)$ is the wavefunction that describes the motion of the election computed at the nucleus position. The second contribution in 2.32 rises from the dipolar interaction between the nuclear and electron magnetic moments and it is anisotropic

$$\widehat{\mathcal{H}}^{dip} = \frac{\mu_0}{4\pi} \left[\frac{\widehat{\boldsymbol{\mu}}^e \cdot \widehat{\boldsymbol{\mu}}^n}{r^3} - \frac{3(\widehat{\boldsymbol{\mu}}^e \cdot \boldsymbol{r})(\widehat{\boldsymbol{\mu}}^n \cdot \boldsymbol{r})}{r^5} \right] \tag{2.34}$$

$\boldsymbol{r}$ is the vector that connects the two magnetic dipoles and $\mu_0 = 4\pi \cdot 10^{-7}$ N A^{-2} is the vacuum magnetic permittivity. The equation 2.34 can be manipulated *[2]* to obtain the nine T_{ij} terms that form the $\boldsymbol{T}$-tensor

$$T_{ij} = \frac{\mu_0}{4\pi} g \beta_e g_n \beta_n \langle \frac{\delta_{ij}}{r^3} - \frac{3ij}{r^5} \rangle \tag{2.35}$$

$i, j = x, y, z$, δ_{ij} is the Kronecker delta and the parentheses $\langle \dots \rangle$ indicate the average on all the electron spatial coordinates. The $\boldsymbol{T}$-tensor is called dipolar hyperfine interaction tensor or anisotropic hyperfine tensor and it is represented by a symmetric matrix with zero trace. As for the $\boldsymbol{g}$-tensor, the elements A_{ij} and T_{ij} of the tensors $\boldsymbol{A}$ and $\boldsymbol{T}$ depend on the reference system. The tensors become diagonal

if they are expressed in the principal axes reference system; the values on the diagonal are the principal values and are indicated as A_X, A_Y, A_Z and T_X, T_Y, T_Z.
In solid samples or in high viscosity solutions, the hyperfine separation between the EPR lines depends on the orientation of the paramagnetic molecules with respect to the external magnetic field.

2.7 - Pulsed EPR spectroscopy

2.7.1 - General remarks

The first pulsed EPR measurements go back to the fifties [3,11], short after the first experiments of pulsed NMR spectroscopy. However, unlike NMR, pulsed EPR spectroscopy has been fully developed only some decades after its discovery because of the different technical requirements of the two techniques. The magnetic moment of the electron is about 1000 times higher with respect of the magnetic moments of proton and ^{13}C, because of the high mass difference ($m_H = 1833 m_e$); the relaxation times decrease approximately with the square of the magnetic moments, so the electrons have relaxation times about 10^6 times smaller with respect to the nuclei. Therefore, pulsed EPR requires much shorter pulse than those used for pulsed NMR and consequently a much faster and complex electronic apparatus.
Although the technology today enables many pulsed experiments with various pulse sequences, the pulsed EPR techniques have not replaced the cw techniques as for NMR, but they are both used. The main reason is that a typical EPR spectrum covers a frequency region that is wider than that covered by a typical NMR spectrum. The spectra or organic radicals cover some tens to hundreds of megahertz, while the spectra of transition metal ions can reach the thousands of megahertz. With the current spectrometers, the shortest pulse that can be generated have a duration τ_p of some nanoseconds, so they can excite a frequency region of some tens of megahertz ($\Delta\nu_{eff} = 1/6\tau_p$); with pulsed EPR we can excite only a small region of the spectral range.
Another drawback of the pulsed EPR technique is due to an instrumental time between the generation of the pulse and the detection of the signal during which the EPR signal is lost. This is called instrumental dead time (in X-band it is about 200 ns) and it's necessary to protect the detector from the high power mw radiations of the pulses, but involves a loss of the fastest decaying signals.
The main advantage of the pulsed techniques consists of the very accurate control that the operator has during the generation of the EPR signal and consequently on the information that are contained in it. In a simple cw spectrum we observe the effects due to all the parameters that affect the spin system, relaxation processes, hyperfine couplings, anisotropies, quadrupole moments, field inhomogeneity, etc. and often it is not possible to disentangle all these contributes. However using an

appropriate pulse sequence it is possible to generate a signal that contains only the desired information by removing all the uninteresting effects.

2.7.2 - Basic principles

We start with the system described in section 2.4, with equilibrium conditions (2.18). We apply a mw pulse $\boldsymbol{B}_1$ of duration τ_p along the X axis of the rotating reference system and centered at the resonance frequency ω_0, the effective magnetic field in the rotating system then coincides with $\boldsymbol{B}_1$ and the magnetization vector starts to precede around $\boldsymbol{B}_1$ of an angle $\beta = g_e\beta_e B_1\tau_p$. In the simplest pulsed EPR experiments a single pulse along X is used with such a duration to bring the magnetization from the Z axis exactly to the Y axis of the rotating reference system (Fig. 2.10 upper part); this pulse is called 90° pulse or $\pi/2$ pulse and its duration is $\tau_p = \pi/2g_e\beta_e B_1$.

If the resonance condition is not exactly fulfilled, the magnetization, in the rotating reference system, precedes around the effective field that is the vector sum of $\boldsymbol{B}_1$ and of the residual field along Z; the frequency of the rotation is $\Omega = \omega_0 - \omega_{mw}$.

Usually the detection system is located in the xy plane of the laboratory reference system. The signal that is recorded is the time evolution of the transverse magnetization that is the product of an oscillating function at frequency Ω and of an exponential decay function with time constant T_2. This product is called free induction decay (FID). By calculating the Fourier transform of the FID we obtain the spectrum in the frequency domain (Fig. 2.10 down).

2.7.3 - Experiments and pulse sequences

The simplest pulse sequence consists of a single pulse and has just been described in

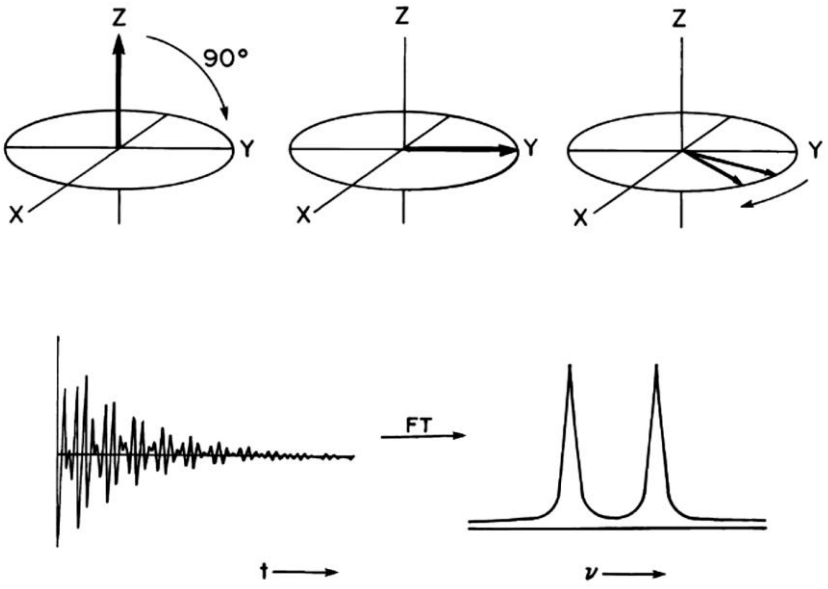

Figure 2.10 up) behavior of the magnetization due to a $\pi/2$ pulse along X; down) FID and corresponding FT-EPR spectra.

the previous section. With this pulse sequence, it is possible to obtain the FID. Almost all pulse sequences, both the simple and the more complex, are characterized by three phases:

1. Preparation phase: in this phase, the spin system is prepared. Some pulses and some constant time delays are used to generate a non-equilibrium magnetization that can evolve in the next period.
2. Evolution phase: this phase consists of time delays and/or pulses that generally vary during the experiment.
3. Acquisition phase: this phase usually begins with one or more pulses that bring all or part of the magnetization in the xy plane in order to have a detectable signal.

2.7.4 - 2p and 3p Electron Spin-echo experiments

The simplest pulse sequence for an electron spin-echo (ESE) experiment is the following: $\pi/2 - \tau - \pi - \tau - echo$ (two pulse echo, Fig. 2.11 upper part). The preparation phase consists of a $\pi/2$ pulse along X that equals the populations of the states and induces coherence in the spin motion; in this way the resulting magnetization is along Y. After the pulse, the system is free to evolve for a time delay τ. During τ the component of the magnetization in the XY tends to disappear because of the loss of coherence caused by the different precession frequencies of each spin ($\Omega_i = \omega_i - \omega_{mw}$), the transverse relaxation (T_2) and the inhomogeneity of the external field $\boldsymbol{B}_0$. The π pulse, applied after τ, rotates the magnetization by 180° around the X axis converting M_Y into $-M_Y$; the direction of precession of the spins remains unchanged. This second pulse causes the spins to be refocused after another time delay τ, along $-Y$, generating so a spin-echo that can be revealed (Fig. 2.11 lower part).

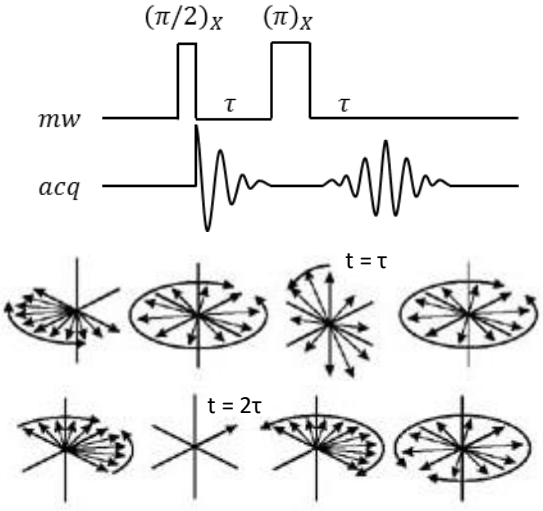

Figure 2.11 Pulse sequence for a two pulse electon spin echo experiment. In the lower part is depicted the behavior of the magnetization during a spin-echo experiment.

The evolution period has a total duration of 2τ and is divided into two equal parts by the π pulse; in the first part the phase coherence between the spins is lost and it is recovered during the second part, but not totally because the phase loss is due also to T_2-type processes that are completely random. The spin-echo is formed by two facing FIDs and its intensity depends on the value of τ. Sometimes the echo is used to obtain the whole FID in fast relaxing samples, whose FID signal decays within the instrumental dead time. Hahn echo experiments are obtained by collecting echo intensity as function of the delay τ, generating a trace that is normally fitted by exponential functions. Important deviation from this type of decay has been found at very low temperatures (see for example [12]).
Moreover, in solid samples the echo decays not only because of typical T_2 processes, but also because of other solid state processes, like Instantaneous diffusion and spin diffusion, in general the decay observed for samples in solid phase has a form of type $\exp[-(2\tau/T_M)^x]$ with T_M the phase memory time and x the exponent of the stretched exponential (often $x = 1$).

A stimulated spin-echo (or three pulse echo) is obtained by the pulse sequence: $\pi/2 - \tau - \pi/2 - T - \pi/2 - \tau - echo$ (Fig 2.12). The first pulse transfer the magnetization along Y, then the spins precede around Z and lose their phase coherence. After τ the components of the magnetization that are in resonance ($\omega_i = \omega_{mw}$) and the components that precede with frequency $\Omega = 2\pi n/\tau$ are along Y. These components are rotated along $-z$ by the second mw pulse, so the overall effect of the first two pulses is a population inversion. The components of the magnetization that are along $-Y$ at time τ are rotated along $+z$ by the second pulse, while the components that are along $\pm X$ are not affected by the pulse.
The components of the magnetization that are stored along $-z$ decay with time constant T_1. After the evolution time T ($T \leq T_1$), the third pulse brings the magnetization along $-Y$ and, after a sencond time delay τ, the spin are refocused and the echo is formed. In the three pulse echo experiments the intensity of the echo is measured varying the time T and keeping fixed the time τ. This three pulse echo sequence can be assimilated to the two pulse sequence if we imagine to divide the π pulse into two $\pi/2$ pulses and between them, during the evolution time T, to store the magnetization along $-z$. The echo is therefore influenced by everything that modifies the component M_z during time T, such as spin or spectral diffusion,

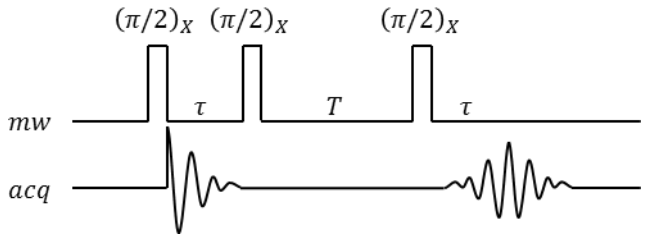

Figure 2.12 Pulse sequence for a three pulse electon spin echo experiment.

chemical exchange, molecular motion, etc.

2.7.5 - Echo-detected EPR

The echo-detected EPR (ED-EPR) experiment enables to acquire the equivalent of cw-EPR spectra obtained by an ESE experiment, for species with long relaxation times. In field-swept echo detected EPR (ED-EPR), the intensity of the Hahn echo is recorded on varying the magnetic field B_0 at a fixed time delay τ between the two pulses.
This spectroscopy is interesting for samples where the phase memory time T_M does not vary substantially for the different spin packets. In fact, in this case, the relative intensities of the EPR lines in cw-EPR and ED-EPR spectra are substantially the same.

2.7.6 - Inversion Recovery experiment

The inversion recovery (IR) experiment has the purpose of measuring the spin-lattice relaxation time T_1 that determines the recovery of the equilibrium of the longitudinal component of the magnetization according equation 2.19a. To conduct this experiment we need to build a non-equilibrium population using a π pulse; after that we record the recovery of the equilibrium using an echo sequence. The pulse sequence used for this experiment is: $\pi - T - \pi/2 - \tau - \pi - \tau - echo$ (Fig. 2.13).
The preparation period consists of the first π pulse along X. It inverts the population of the spin states, the magnetization vector is still oriented along the Z axis, but with opposite direction ($M_z = -M_0$). Then, there is an evolution period during which the system can relax toward equilibrium; this period has a variable duration T. After that, there is the acquisition period in which the magnetization is brought in the XY plane and then revealed with an echo sequence. The whole sequence is repeated many times varying the delay time T. The echo intensity is proportional to the magnetization M_z. For short T, the echo signal is in emission since the magnetization, before the $\pi/2$ pulse, is still along $-Z$. For larger T the magnetization has time enough to come back along $+Z$ and the echo signal is in absorption. The echo intensity is equal to zero when $\tau = T_1 \ln 2 = 0.693 T_1$. An IR experiment is conducted by measuring the echo intensity by varying the time T between the first and the second pulse

2.7.7 - 2p and 3p ESEEM experiments

Hyperfine interactions can provide essential information regarding spin distribution

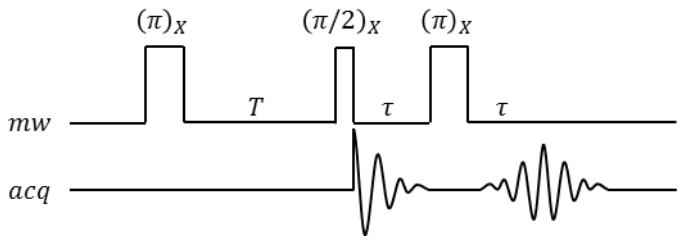

Figure 2.13 Pulse sequence for an echo-detected inversion recovery experiment.

inside molecules, and/or, more in general, can provide geometrical information regarding the nuclei distribution in the neighborhood of the unpaired electron.
In the echo experiments, the presence of anisotropic hyperfine coupling between the electron spin and nuclear spins can cause a modulation of the echo intensity. This effect is called electron spin echo envelope modulation (ESEEM) and occurs only for solid samples or viscous solution because appears only in presence of anisotropic interactions. The ESEEM technique is very useful to detect nuclei that are weakly coupled with a paramagnetic center and with a small Zeeman splitting; it is often used complementarily with the ENDOR technique (electron nuclear double resonance). The echo modulation can be observed only if the some forbidden EPR transitions become partially allowed, indeed the simultaneous variation of the quantum numbers m_S e m_i ($\Delta m_S = \pm 1, \Delta m_i = 0, \pm 1, \dots, \pm 2i$).
In a two pulse ESEEM experiment (2p-ESEEM, Fig. 2.11) the echo decay is recorded varying the evolution time τ. The echo decays because of the T_1 and T_2 relaxations, but the decay is modulated by the presence of hyperfine interactions. The modulation for a simple system formed by an electron anisotropically coupled with a proton ($i = 1/2$) in a two pulse experiment is:

$$E_{mod}(2\tau) = 1 - \frac{k}{4}\big[2 - 2\cos(\omega_\alpha \tau) - 2\cos(\omega_\beta \tau) + \cos(\omega_+ \tau) - \cos(\omega_- \tau)\big] \tag{2.36}$$

where k is a parameter called modulation depth and is related to the asymmetry of the transitions ω_α and ω_β with respect to the resonance frequency of the free nucleus; along the principal directions of the hyperfine tensor $k = 0$. To detect the frequencies ω_α and ω_β, the ESEEM signal is Fourier transformed. If the system is made of different nuclei that are coupled with the electron, the echo modulation is given by the product rule:

$$E^n_{mod}(2\tau) = \prod_i^n E^{(i)}_{mod}(2\tau) \tag{2.37}$$

so, in the spectrum are contained also combination frequencies. Except for these frequencies and for sum and difference frequencies, the lines in a ESEEM spectrum correspond to those that are obtained in the ENDOR spectrum is recorded. The echo decays with time constant T_2 that usually is about some microseconds, that is generally a drawback because the decay is too fast and cannot be recorded for enough time. This can be avoided using a three pulse echo sequence.

In a three pulse ESEEM (3p-ESEEM) experiment (Fig. 2.12) the echo decay is recorded varying the time T between the second and the third pulse and keeping the time τ

fixed; the three pulse echo shows also a modulation due to hyperfine interactions. In the two pulse experiment coherence is generated only for the electron spins, on the other side, in a three pulse experiment, the second $\pi/2$ pulse transfers the coherence from the electron to the nuclear spins. This coherence evolves during the evolution time T and decays with time constant T_{2n} (nuclear, or with time constant T_1 if $T_1 > T_{2n}$) that usually is much bigger than the electronic T_2. The third pulse transfers the coherence back to the electron spins to be detected. If we consider the simple system that was considered before (an electron coupled with a proton), the echo modulation at time $\tau + \tau$' (where $\tau' = T + \tau$) for the three pulse experiment is:

$$E_{mod}(\tau + \tau') = 1 - \frac{k}{4}\left\{\begin{matrix}[1-\cos(\omega_\alpha \tau)]\left[1-\cos\left(\omega_\beta \tau'\right)\right] \\ +\left[1-\cos(\omega_\beta \tau)\right][1-\cos(\omega_\alpha \tau')]\end{matrix}\right\} \qquad (2.38)$$

Unlike the modulation obtained in the two pulse experiment, in this case, we have no sum or difference frequency. If there are more than one coupled nucleus we can use the product rule:

$$E^n_{mod}(\tau + \tau') = \frac{1}{2}\left[\prod_i^n E^{(i)}_\alpha(\tau, \tau') + \prod_i^n E^{(i)}_\beta(\tau, \tau')\right] \qquad (2.39)$$

The great advantage of the three pulse ESEEM with respect to the two pulse experiment is due to the slow decay of the modulation that is no more determined by T_2. The ESEEM spectrum obtained with a three pulse sequence is simpler, but has a drawback: in the spectra some frequencies are missing when one of the term of equation 2.38 is equal to zero ($\omega\tau = 2n\pi$). These frequencies are called blind spots.

2.7.8 - Pulsed ENDOR experiments

The ENDOR technique enables to measure the resonance frequency of nuclei coupled with the unpaired electron by exciting at the same time the electronic spin with a mw radiation and the nuclear spins with a radiofrequency (rf) radiation. In the cw-ENDOR experiments the intensity of the spectrum depends critically on the relaxing times of the electron and the nuclei and on the mw and rf fields. Moreover, even if all is optimized, the intensity of a cw-ENDOR spectrum is only a small fraction of the intensity of a cw-EPR spectrum.

After the discovery of the pulsed EPR, many pulse sequences to record ENDOR spectra were developed. The main advantage of pulsed ENDOR is that the whole pulse sequence is short enough to exclude undesired relaxation effects, so it is possible to study very fast relaxing systems. There are two basic approaches to the pulsed ENDOR spectroscopy: the original one developed by Mims in 1965 [13] and the one developed by Davies in 1974 [14].

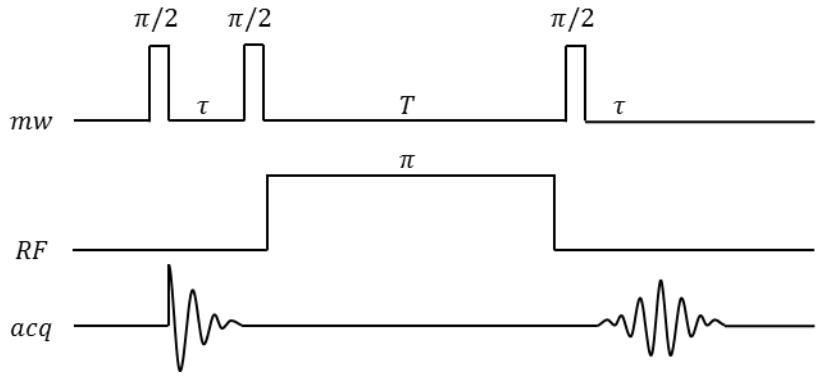

Figure 2.14 Pulse sequence for a Mims ENDOR experiment.

Mims ENDOR

The pulse sequence developed by Mims is formed by a three pulse echo sequence with a rf pulse during the evolution time T (Fig. x.14). The preparation period is formed by the two first $\pi/2$ pulses, the evolution period by the delay T and the rf pulse and the acquisition period follows the third $\pi/2$ pulse. If the rf pulse inverts a nuclear spin coupled with one electron spin, this changes its resonance frequency of a quantity that is equal to the hyperfine coupling constant a. Thus, at time τ after the third mw pulse, when the stimulated echo appears, the electron spin has not the same phase that would have had without the rf pulse, the phase difference is equal to $a\tau$. Unless $a\tau$ is a multiple of 2π we don't observe a complete refocusing of M_Y at time τ to form the echo; thus the ENDOR signal appears as a lowering of the echo intensity. The Mims ENDOR spectrum has blind spots for $\tau = 2k\pi/a$ where k is an integer.

Davies ENDOR

The Davies ENDOR experiment uses a pulse sequence that invertes the populations of the electronic spin states (Fig. x.15). The preparation period consists of a selective π pulse that invertes the population of one EPR transition; the evolution period consist of a delay time T during which a selective rf π pulse is applied to invert the population of one of the NMR transitions. Then there is an echo sequence and the echo is recorded. The rf pulse eliminates the population difference of the EPR

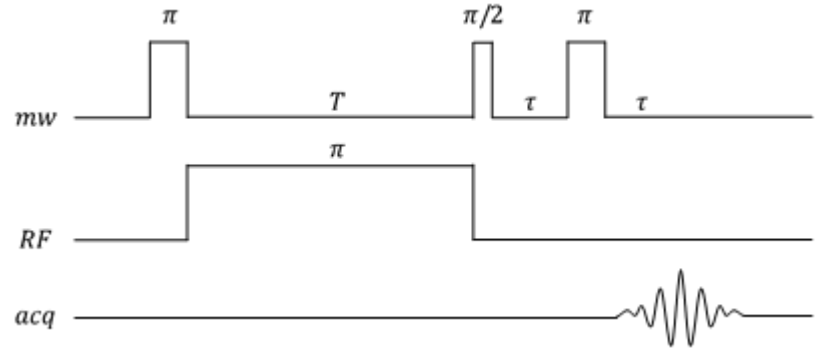

Figure 2.15 Pulse sequence for a Davies ENDOR experiment.

transition that was excited by the first mw pulse, consequently there is a lowering or a disappearance of the echo.

References

[1] NM Atherton, N Atherton, Electron spin resonance: theory and applications, Ellis Horwood Chichester 1973.

[2] M Brustolon, Electron paramagnetic resonance: a practitioner's toolkit, John Wiley & Sons 2009.

[3] A Schweiger, G Jeschke. Principles of pulse electron paramagnetic resonance, Oxford University Press, Great Clarendon Street, Oxford, OX 2 6 DP, UK, 2001. (2001) 1-578.

[4] JA Weil, JR Bolton, Electron paramagnetic resonance: elementary theory and practical applications, Wiley-Interscience 2007.

[5] PW Atkins, J De Paula, Atkins' physical chemistry, Oxford University Press Oxford 2006.

[6] FJ Dyson. Electron spin resonance absorption in metals. II. Theory of electron diffusion and the skin effect, Physical Review. 98 (1955) 349.

[7] G Feher, A Kip. Electron spin resonance absorption in metals. I. Experimental, Physical Review. 98 (1955) 337.

[8] G Wagoner. Spin resonance of charge carriers in graphite, Physical Review. 118 (1960) 647.

[9] NW Ashcroft, ND Mermin, Solid State Physics, Saunders College, Philadelphia, 1976.

[10] AF Orchard, Magnetochemistry, Oxford University Press 2003.

[11] A Schweiger. Pulsed Electron Spin Resonance Spectroscopy: Basic Principles, Techniques, and Examples of Applications [New Analytical Methods (43)], Angewandte Chemie International Edition in English. 30 (1991) 265-292.

[12] A Maniero. Dynamics and spin relaxation of tempone in a host crystal. An ENDOR, high field EPR and electron spin echo study, Physical Chemistry Chemical Physics. 1 (1999) 4015-4023.

[13] W Mims. Pulsed ENDOR experiments, Proceedings of the Royal Society of London.Series A, Mathematical and Physical Sciences. (1965) 452-457.

[14] E Davies. A new pulse ENDOR technique, Physics Letters A. 47 (1974) 1-2.

CHAPTER 3 - EPR CHARACTERIZATION OF GRAPHENE-LIKE MATERIALS: CHEMICALLY EXFOLIATED GRAPHITES

3.1 - Introduction

Nowadays several methods to produce graphene have been reported; the aim of many researcher is to find a way to obtain good quality materials at low cost and in large quantities. A review of the methods proposed so far has been given in the introduction. Among these methods, one that enable to obtain materials in large scale is the exfoliation of graphite. The production of reduced graphene oxide is based on the exfoliation of graphite, but the most common methods based on the Hummers process [1] enables to obtain very defective materials. Other methods to chemically expand graphites are available [2]. In this part of the thesis we focus on expanded graphites, since their electronic properties, to the best of our knowledge, have never been studied in detail, with the aim of rationalizing the development of the features typical of graphene during the preparation of this material.

Exfoliation of graphite is a 'top-down' approach [3]. In some way it resembles the original scotch-tape method [4], seeking to separate carbon monolayers from graphite, but it does so by using a combination of solvents, exfoliating agents and sonication. Some of the exfoliation methods have recently gained interest [5] as they enable the production of graphene-like materials in relatively high quantity without introducing oxygen defects in the graphene structure. One drawback is that the separation of the graphite sheets is often incomplete. In some cases, to make exfoliation easier, the starting material is functionalized to provide a better interaction with the solvent [6].

Two approaches have been used to obtain the exfoliated samples studied in this chapter, the first is the intercalation of graphite with potassium metal and subsequent treatment with ethanol that causes the production of molecular hydrogen that separates mechanically the graphene layers. The second method is the intercalation of graphite with a mixture of nitric and sulphuric acid. The separation of the layers is obtained by heating and decomposing the acids to give volatile products (water, sulfur dioxide and nitrogen oxides).

In this chapter we show a comparative study of the electronic properties of natural graphite, used as a starting material, chemically expanded graphites obtained by different methods based on chemical exfoliation and a commercial sample of reduced graphene oxide consisting of stacks of few graphene layers, with the edges decorated with oxygen functional groups, in the undispersed solid form. We focus in particular on a sophisticated EPR study, to identify paramagnetic defects and conduction electrons.

3.2 - Experimentals

3.2.1 - Materials

Five different materials were characterized in this study. We started from natural Madagascar graphite, which was used as starting material (**SM**). This was used for the preparation of three processed samples as described below in this section. Finally, we considered a commercial reduced graphene oxide (**RGO**) for reference.
RGO was received from ACS Materials (MA, USA), labelled 'Single layer Graphene' and used solid without further purification. Natural Madagascar graphite was kindly provided by Superior Graphite (Chicago, USA). Potassium metal, absolute ethanol, sulphuric acid and nitric acid were acquired from Sigma-Aldrich and were used as received.

*Exfoliation of graphite by potassium intercalation and expansion (sample **EK**).* SM (1 g, 83.3 mmol) was loaded in a glass vial with mounted Schlenk-type valve. The vial underwent three vacuum-argon cycles, and then potassium metal (0.41 g, 10.5 mmol) was loaded under argon flow. After evacuation and three more vacuum-argon cycles, the vial was flame-sealed under vacuum. The tube was set in a tubular oven and heated to 200 °C overnight. The tube was opened in a glove box and the potassium graphite (KC_8) poured in a 100 mL round bottom flask together with 20 mL ethanol. The suspension was stirred for 1 hour, then filtered and washed thoroughly with ethanol to remove potassium ethoxide. The product was finally sonicated in 20 mL ethanol for 8 hours at 150 W, then the solvent was removed under vacuum and the residue dried overnight at 100 °C under vacuum.

*Expansion of graphite by acid treatment (sample **EH**).* 100 ml of a 4:1 mixture of sulphuric and nitric acid were loaded in a 250 mL round bottom flask. SM (5 g) was then added and the suspension stirred overnight. The resulting solid was filtered and washed with water to remove excess acid, then irradiated in a microwave apparatus for 40 s at 800 W. The product was dried overnight at 100 °C under vacuum.

*Combined expansion-exfoliation (sample **EHK**).* One portion of sample EH underwent further treatment with potassium intercalation and exfoliation in ethanol, following the whole procedure described before for sample EK.
In Figure 3.1 are reported the SEM images for the expanded graphites and for the RGO sample.

3.2.2 - X-ray powder diffraction analysis

X-rays powder diffraction (XRD) transmission patterns were recorded in the diffraction angular range $5° \leq 2\theta \leq 60°$ with a 0.1° resolution, by a Philips X'Pert PRO diffractometer working in the reflection geometry and equipped with a graphite

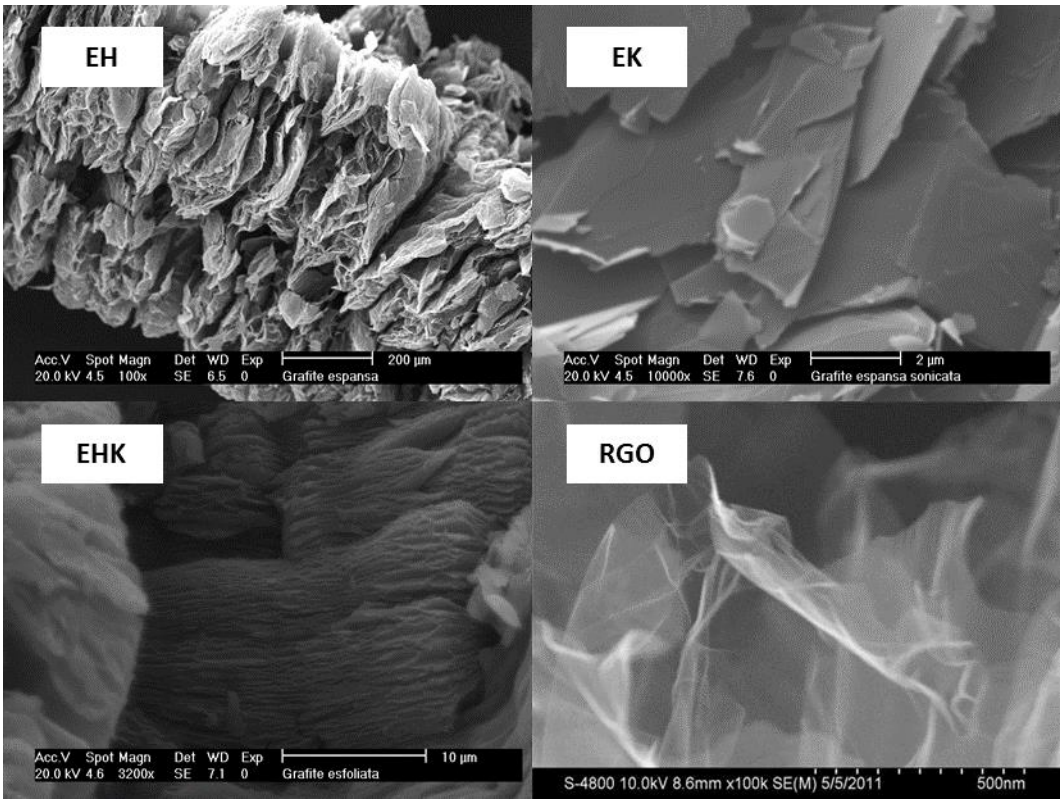

Figure 3.1 SEM images of sample EH, EK, EHK and RGO. The scale is indicated in each picture. The SEM image for sample RGO comes from the technical data sheet of the sample.

monochromator on the diffracted beam ($Cu_{\mathrm{K}\alpha}$ radiation). The full width at half maximum (FWHM) parameters were calculated for most intense peaks by fitting the diffractogram with Lorentzian functions.

3.2.3 - Raman measurements

Raman spectra have been recorded with a micro-Raman via a Renishaw spectrometer coupled with an optical microscope. Powder samples were suspended in dichloromethane in an ultrasound bath and drop cast on a standard microscope borosilicate glass plate. After evaporation of the solvent, the spectra were recorded with an excitation wavelength of 622 nm in the 900 to 3200 cm^{-1} range.

3.2.4 - EPR measurements

The EPR measurements, cw and pulsed, were obtained with an X-band Bruker ELEXYS spectrometer, equipped with a dielectric resonator and a nitrogen/helium gas-flow cryostat for low temperature measurement. The samples were placed inside 2 or 3 mm ID quartz EPR tubes sealed under vacuum after full evacuation of adsorbed gases. The EPR signals were followed as function of temperature from room temperature (290 K) down to almost the liquid helium temperature (10 K ca.). The field was calibrated using a standard sample with known g-factor (LiTCNQ). The spectra were

also corrected taking into account the variation of the quality factor of the resonators with temperature.

Pulsed experiments were performed using the standard pulse sequences: $\pi/2 - \tau - \pi - \tau - echo$ for the electron spin echo (ESE) decay measurement (HD); for the echo detected inversion recovery (IR), instead, the sequence was $\pi - T - \pi/2 - \tau - \pi - \tau - echo$. The resonance field was set at the maximum of the EPR intensity. The Echo-detected EPR (ED-EPR) spectra were obtained by recording the integrated echo intensity as function of the magnetic field. The two pulse electron spin echo envelope modulation (2p-ESEEM) spectra were obtained by Fourier transforming the modulation of the HD, after a proper reconstruction of the signal taking into account the instrumental dead time.

3.3 - Results

3.3.1 - XRD measurements

XRD patterns recorded for the samples EH, EK, EHK and RGO are reported in Figure 3.2, along with the data from the starting material. In the spectra, the (002), the (100), (101) and (004) reflections are observed at about 26°, 42° 44° and 54° respectively [7].

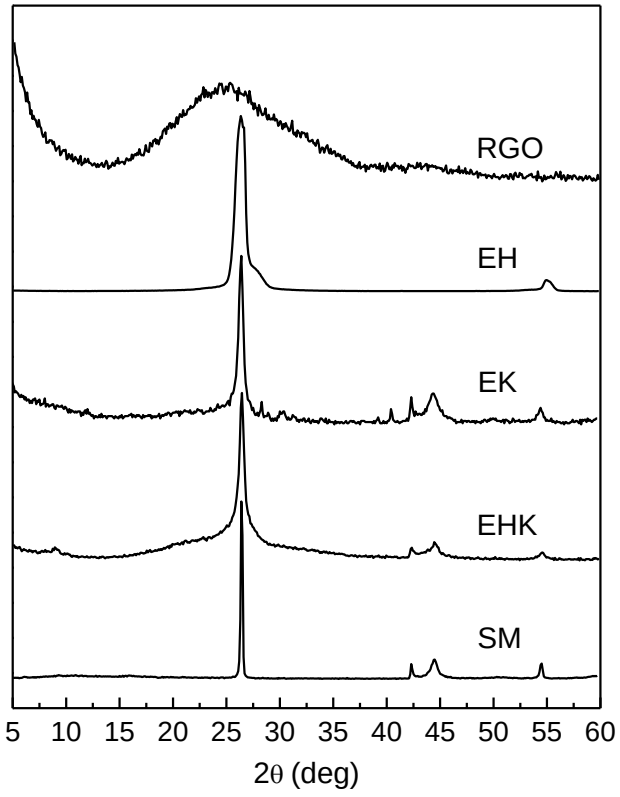

Figure 3.2 Powder diffraction patterns for SM, EK, EH, EHK and RGO samples.

Table 3.1 Position and linewidth (FWHM) of the XRD (002) peaks for the relative samples in Figure 3.2.

Sample	Peak 1 (002)		
	Position (°)	FWHM (°)	Amplitude
RGO	23.9	7.9	810
	29.5*	10.1	500
EH	26	0.57	6100
	26.36	0.51	6600
	26.66	0.3	3200
	27.83*	1.2	1800
EK	24.6	10	164
	26.4	0.48	100
EHK	22	6	350
	26.02	3.3	417
	26.44	0.47	314
	30*	10	400
SM	26.44	0.13	180

* likely (002) reflection of graphite in rhombohedral form (J.-T. Wang, C. Chen, E. Wang, Y. Kawazoe, Sci. Rep., **4**, (2013) 4339).

Comparison between different samples can be made by focusing on the (002) peaks, which are associated to the interplanar distance between graphene sheets packed into the graphitic structure and to the dimension of the stacking. Table 3.1 reports both the angular position and the full width at half maximum (FWHM) parameter of the (002) reflections. The spectra of the samples can be interpreted as a superposition of two types of reflections, one narrow, centered at 26.44° of the starting material, and one broad, which is particularly evident for the RGO sample. The narrow-line reflection is strong only for EH sample, for which the elastic scattering tail (due to amorphous parts) at low angle values is almost unobservable. The data in Table 3.1 show that, for samples EH, EK and EHK, the narrow peaks have a FWHM of 0.45° ÷ 0.51°, much broader than that of SM. It is possible to have a rough estimate of particle dimensions (L) by applying the Scherrer equation [8]:

$$L_{a,c} = \frac{k_{a,c}\lambda}{FWHM \cos\theta} \tag{3.1}$$

Where $k_{a,c}$ is a dimensionless shape factor with a typical value of about 0.9 that depends on the actual shape of the particles [9], λ is the instrument wavelength of the line centered at the given θ value. Because of the inhomogeneity of the sample, we consider the obtained numbers representative of the average structures. From the above equation we found that the thickness of the stacks (L_c) is about 260 Å, that corresponds to 70-80 stacked graphene layers. Samples EK and EHK, which are dominated by broader signals, 3.3° to 10° wide, have fewer stacked graphene layers:

about 14 layers for EK and 23-41 layers for EHK. For these samples the low-angle component is clearly visible, indicating likely the presence of non-crystalline carbon. Information about the lateral L_a dimension can be obtained from the FWHM values of the (100) reflections, that are evident for EK, EHK and RGO samples. In this case the Scherrer equation enables to obtain the values of $L_a = 0.16$, 0.12 and 0.02 μm respectively.

3.3.2 - Raman spectroscopy

The Raman spectra of the studied samples at room temperature, normalized for the G band intensity, are displayed in Figure 3.3a. In the spectra of all samples, the G bands are observed at 1580 cm^{-1} ca. (the position is shifted to lower values for RGO) [10,11] while the D bands were recorded at 1320 cm^{-1} ca. The D' bands (1600 cm^{-1} ca.) and the $2D$ bands (2700 cm^{-1} ca.) follow as expected in all cases. The difference in the ratio $A(D)/A(G)$ (see Table 3.2) between the integrated intensities of the D and the G bands is the first informative aspect emerging from the analysis of the spectra. This ratio is related to the density of the Raman-active defects in the materials.

Since in most cases the bands appeared to be multicomponent, we deconvoluted them as sum of Lorentzian lines. For the D, G and D' bands we used one Lorentzian component, while for the $2D$ band up to four components were used in order to

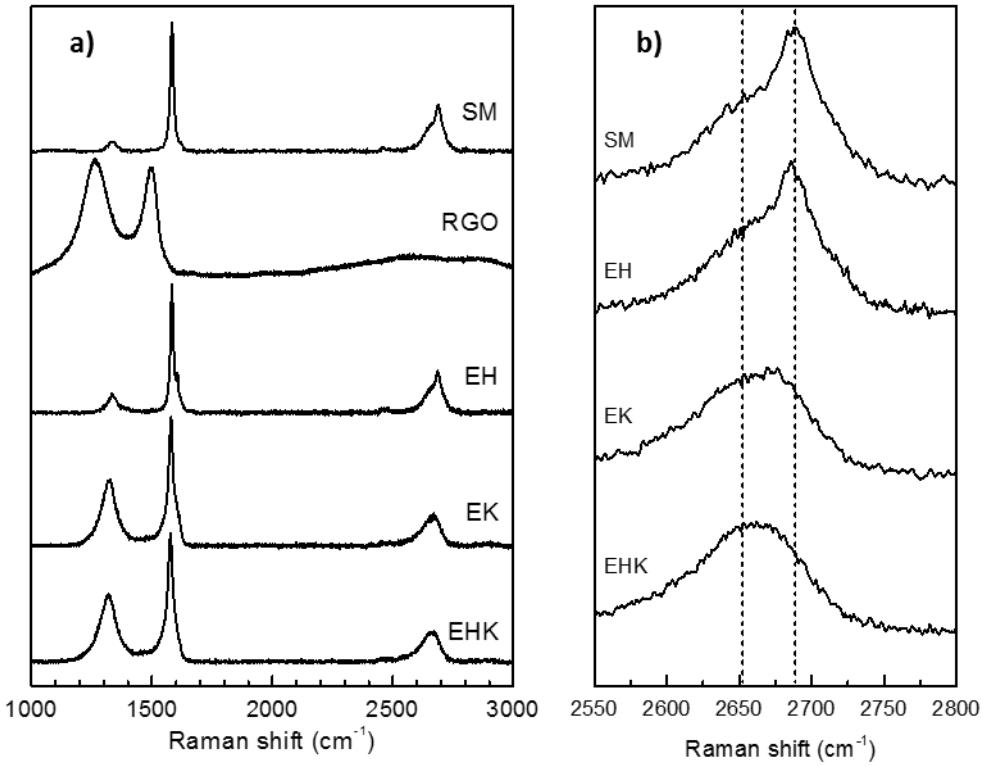

Figure 3.3 (a) Raman spectra of samples SM, RGO, EH, EK and EHK at 622 nm. (b) 2D band for samples SM, EH, EK and EHK. To guide the eye, the positions of the two major components of EH sample are reported (dotted lines).

Table 3.2 Raman shifts, bandwidths and amplitudes A derived from the fit of the bands D, G, D' and $2D$ for all samples. No D' band was observed for sample RGO, the $2D$ band was fitted using two to four components. In the last column the ratio between the amplitude of the D and the G bands are reported.

Sample	Band	Raman shift (cm^{-1})	Width (cm^{-1})	A /10^4 (a. u.)	$A(D)/A(G)$
RGO	D	1337.1 ± 0.3	148 ± 1	580 ± 5	1.78
	G	1489.0 ± 0.2	83.3 ± 0.8	325 ± 3	
	$2D_1$	2396±5	350	50	
	$2D_2$	2665±1	390	250	
	$2D_3$	2925±1	210	100	
EH	D	1337.0 ± 0.3	51 ± 1	4.26 ± 0.08	0.49
	G	1582.58 ± 0.03	14.3 ± 0.1	8.63 ± 0.04	
	D'	1605.9 ± 0.2	17.5 ± 0.5	2.12 ± 0.05	
	$2D_1$	2652 ± 1	69 ± 2	6.3 ± 0.4	
	$2D_2$	2687.7 ± 0.3	32 ± 1	4.9 ± 0.3	
	$2D_3$	2715.8 ± 0.9	17 ± 3	0.39 ± 0.09	
EK	D	1321.3 ± 0.2	71.9 ± 0.8	29.9 ± 0.3	1.44
	G	1578.4 ± 0.1	27.7 ± 0.3	20.7 ± 0.2	
	D'	1607.8 ± 0.5	14 ± 1	1.3 ± 0.1	
	$2D_1$	2610 ± 10	100 ± 10	4 ± 2	
	$2D_2$	2644 ± 2	50 ± 10	5 ± 2	
	$2D_3$	2673 ± 1	32 ± 8	3 ± 2	
	$2D_4$	2693 ± 2	27 ± 5	1.6 ± 0.7	
EHK	D	1318.2 ± 0.3	82 ± 1	35.8 ± 0.4	1.42
	G	1576.0 ± 0.1	32.6 ± 0.3	25.2 ± 0.2	
	D'	1605. ± 1	7 ± 4	0.2 ± 0.1	
	$2D_1$	2600 ± 10	110 ± 10	5 ± 1	
	$2D_2$	2645 ± 2	49 ± 8	6 ± 2	
	$2D_3$	2672 ± 1	32 ± 9	3 ± 1	
	$2D_4$	2692 ± 2	26 ± 4	1.4 ± 0.6	
SM	D	1335.4 ± 0.6	42.0 ± 1.8	3.7 ± 0.1	0.04
	G	1582.81 ± 0.03	16.3 ± 0.1	18.01 ± 0.07	
	D'	1662.1 ± 0.6	7 ± 1	0.24 ± 0.04	
	$2D_1$	2646 ± 2	60 ± 4	8.7 ± 0.7	
	$2D_2$	2689.3 ± 0.4	38 ± 1	12.9 ± 0.5	

obtain the best reproduction in agreement also with studies in literature [12-15]. The parameters obtained from the deconvolution of the Raman spectra of all samples are collected in Table 3.2.

The D' band is evident in the spectrum of sample EH at 1606 cm^{-1}, it can be observed in samples EK and EHK as a shoulder of the G band and it is apparently absent in sample RGO or hidden under the much wider G band.

The $2D$ bands for samples EH, EK and EHK are given by the sum of three or four components, their positions and intensities, compared to those of the relative G bands, are similar for the three samples and are similar also to what has already been reported in the literature for polycrystalline graphites [10]. The $2D$ band of the

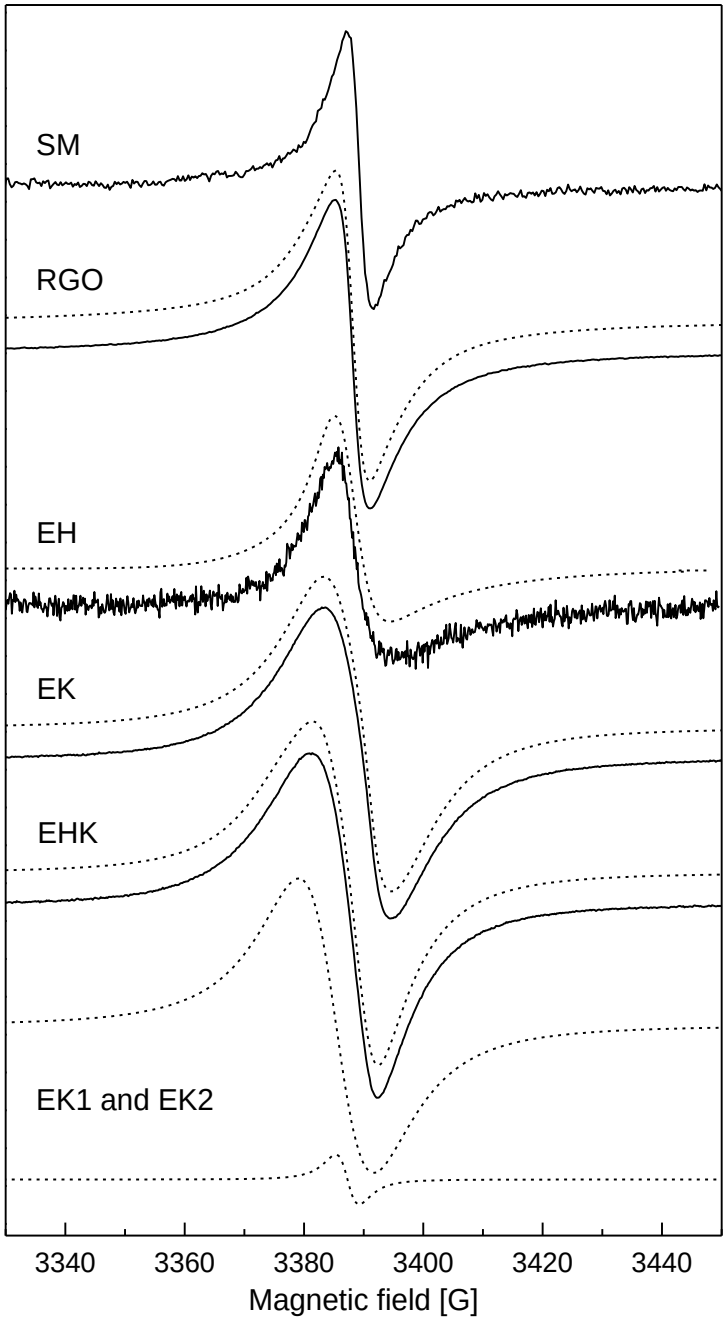

Figure 3.4 Normalized cw-EPR spectra of the samples SM, RGO, EH, EK, EHK at room temperature (full lines) together with their simulation (dashed lines). The simulation parameters are reported in Tables 3.3, 3.4, 3.5, and 3.6. For sample EK the single components EK-1 and EK-2 are reported (dotted lines).

sample RGO, observed after subtraction of a 2000-3000 cm^{-1} broad component [16], instead is much wider than the other samples. This band was deconvoluted using three Lorentzian components. A comparison of the shapes of the 2D bands reported in Fig. 3.3b can be done with Raman spectra obtained from materials with well-defined structures [11]. The structure of the bands of the two samples, EHK and EK is very similar to that obtained from graphene with very few stacked layers, whereas for EH the shape is more similar to materials with more than 5 stacked layers, and approaches that of graphite.

3.3.3 - cw-EPR

The cw-EPR spectra at room temperature for the studied samples are displayed in Fig. 3.4. All the samples are characterized by the presence of an EPR band with a g-factor of ca. 2, typical of organic aromatic systems with low spin-orbit coupling.
Heterogeneity of the samples made us to anticipate that the bands are due to superposition of different contribution, each characterized by different parameters. Analysis of the spectra have confirmed the hypothesis; the simulation of the spectra thus allowed to obtain the deconvoluted spectra of the most intense contributions. For the interpretation of the data we considered three general situations for the electrons: *a)* non-interacting localized electrons, like in radicals, with small hyperfine (electron-nuclear) interactions, exhibiting Gaussian lineshape, *b)* electrons localized or delocalized in narrow regions, with strong electron-electron interaction, exhibiting Lorentzian lineshape, and *c)* mobile electrons in conductive particles with dimension larger than the microwave penetration depth (skin depth), exhibiting Dysonian lineshape, and normally low intensity.
The profile $I(B)$ of the spectra was then fitted as sum of spectra relative to different components with proper normalized lineshape $f(B - B_0)$; typically two components were enough to obtain satisfactory simulations. The assignement of a component to a specific species was done *a posteriori*, after careful analysis of the parameters, and of their variation as function of the temperature. We allowed the lineshape profile to be Lorentzian, Gaussian [17,18] or Dysonian [19,20] choosing the profile fitting better the data. Moreover we simulated the spectra by taking into account only the Zeeman term of the Hamiltonian [17,18]. For components with anisotropic $\boldsymbol{g}$-tensor, we calculated the powder spectrum as a superposition of spectra due to spin packets resonating at different fields:

$$I(B) \propto \sum_i c_i \int_0^{4\pi} \left[f_i\left(B - B_0(\Omega)\right) \right] d\Omega \qquad (3.2)$$

where B_0 is the resonance fields which depends on the angle Ω between the $\boldsymbol{g}$-tensor axes and the field direction, and the coefficients c_i determine the relative contribution of each spin packet.

Table 3.3 Relevant simulation parameters of the cw-EPR spectra at selected temperature for sample RGO. For each contribution i, the linewidth Γ, the g-value and the relative abundance of the species (C_i) is indicated.

T (K)	$\%C_1$	g_1	Γ_1 (G)	g_2	Γ_2 (G)
290	20.3	2.0031	4.41[a]	2.0032	12.97[a]
150	6.3	2.0039	11.95[a]	2.0039	48.34[a]
80	22.3	2.0024	2.86[a]	2.0028	16.21[a]
10	33.6	2.0035	1.45[a]	2.0037	6.12[a]

[a] Lorentzian lineshape

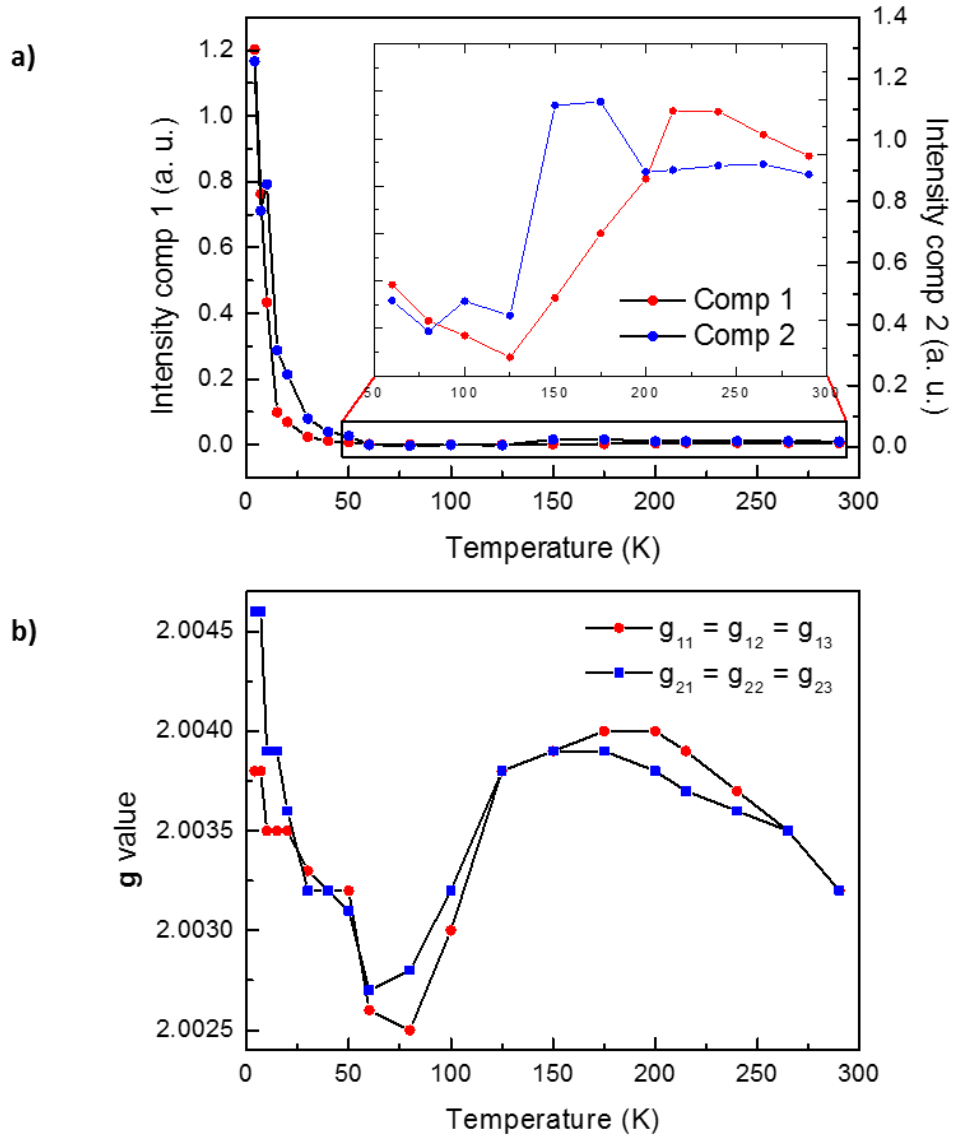

Figure 3.5 (a) intensity variation for each of the two components of the cw-EPR spectrum for sample RGO as function of the temperature (red points = RGO-1, blue points = RGO-2). The inset shows an enlargement of the graph at higher temperatures. (b) g-principal values variation for each of the two components of the cw-EPR spectrum as function of the temperature (red points = RGO-1, blue points = RGO-2).

Table 3.4 Relevant simulation parameters of the cw-EPR spectra at selected temperature for sample EH. For each contribution i, the linewidth Γ, the g-value, the asymmetry parameter α for the Dysonian lineshape and the relative abundance of the species (C_i) is indicated.

T (K)	$\%C_1$	g_1	Γ_1 (G)	g_2	Γ_2 (G)	α_2
295	82	2.0036	17.30[a]	2.0027	6.57[b]	1.8
205	94	2.0060	16.00[a]	2.0035	7.10[b]	6.2
150	97	2.0054	18.60[a]	2.0036	5.49[b]	2.9

[a] Bulk graphite lineshape
[b] General Dysonian lineshape

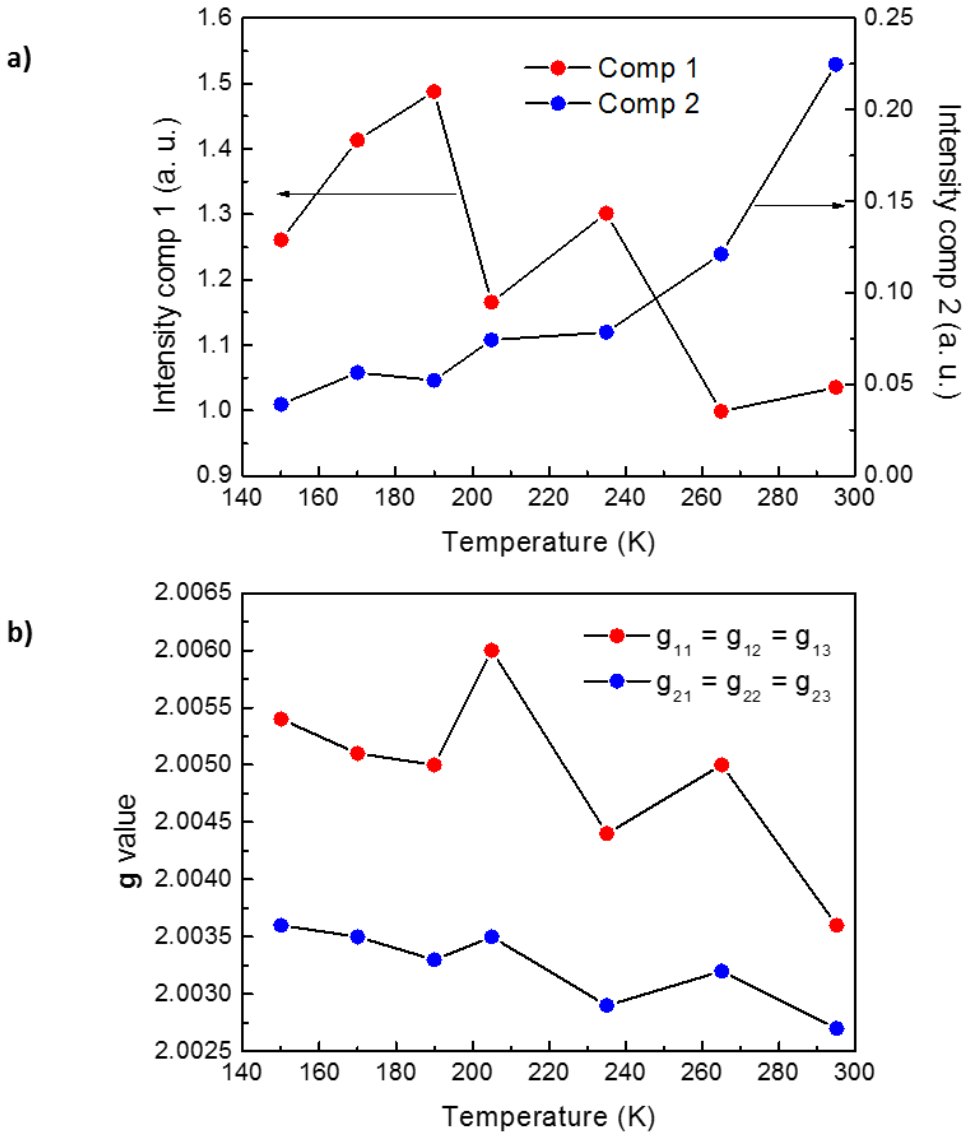

Figure 3.6 (a) intensity variation for each of the two components of the cw-EPR spectrum for sample EH as function of the temperature (red points = EH-1, blue points = EH-2). (b) g-principal values variation for each of the two components of the cw-EPR spectrum as function of the temperature (red points = EH-1, blue points = EH-2).

Table 3.5 Relevant simulation parameters of the cw-EPR spectra at selected temperature for sample EK. For each contribution i, the linewidth Γ, the perpendicular (subscript label a) and parallel (subscript label b) components of the g-tensor and the relative abundance of the species (C_i) is indicated.

T (K)	% C_1	g_1	Γ_1 (G)	g_{2a}	g_{2b}	Γ_2 (G)
290	1.6	2.0016	3.37[a]	2.0027	2.0027	10.9[a]
150	4.0	2.0027	4.53[a]	2.0029	2.0051	11.4[a]
16	15	2.0031	4.56[a]	2.0022	2.0065	9.8[a]

[a] Lorentzian lineshape

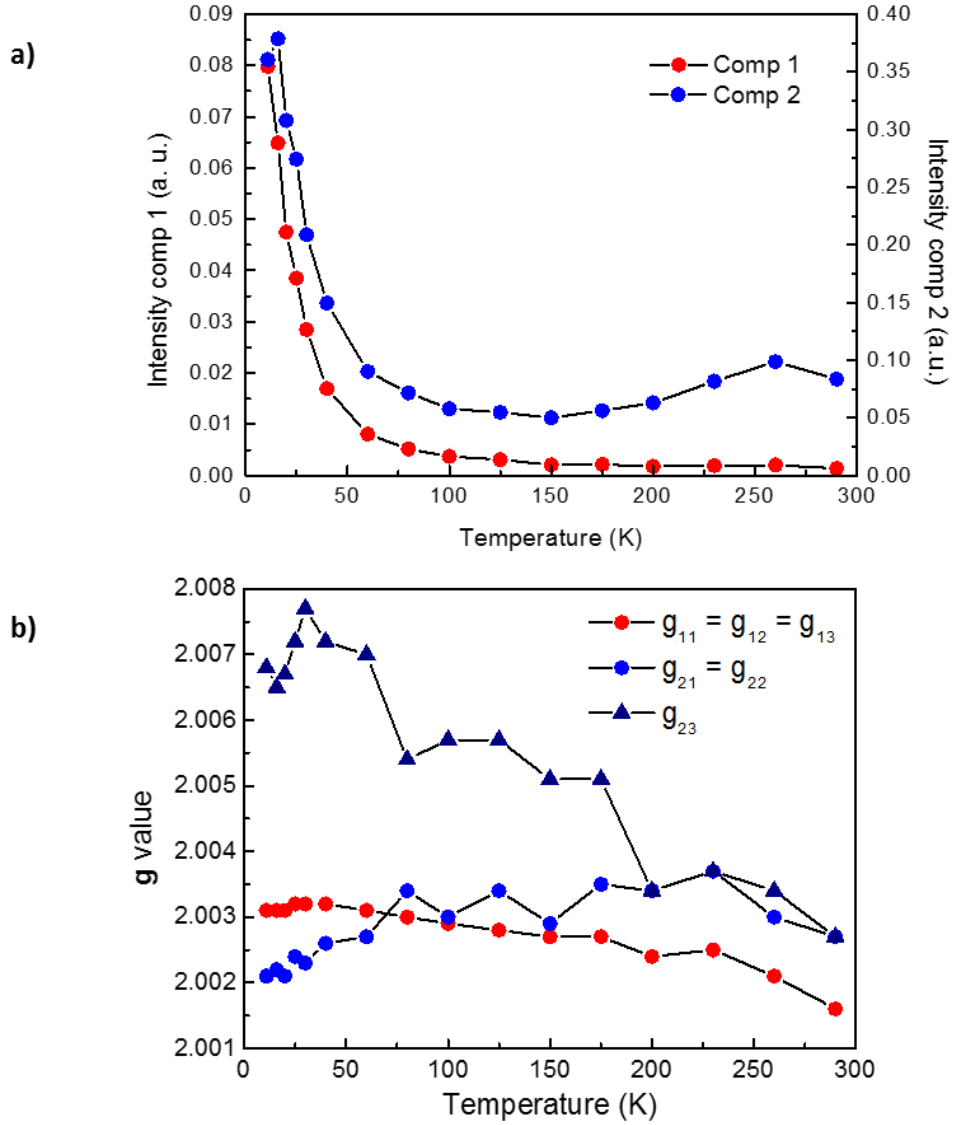

Figure 3.7 (a) intensity variation for each of the two components of the cw-EPR spectrum for sample EK as function of the temperature (red points = EK-1, blue points = EK-2). (b) g-principal values variation for each of the two components of the cw-EPR spectrum as function of the temperature (red points = EK-1, blue points = EK-2).

Table 3.6 Relevant simulation parameters of the cw-EPR spectra at selected temperature for sample EHK. For each contribution i, the linewidth Γ, the perpendicular (subscript label a) and parallel (subscript label b) components of the g-tensor and the relative abundance of the species (C_i) is indicated.

T (K)	$\%C_1$	g_{1a}	g_{1b}	Γ_1 (G)	g_{2a}	g_{2b}	Γ_2 (G)
290	27.5	2.0022	2.0065	5.23[a]	2.0026	2.0093	10.70[a]
140	21.4	2.0027	2.0078	4.90[a]	2.0035	2.0109	12.90[a]
7.5	21.3	2.0026	2.0047	3.31[a]	2.0041	2.0041	9.61[a]

[a] Lorentzian lineshape

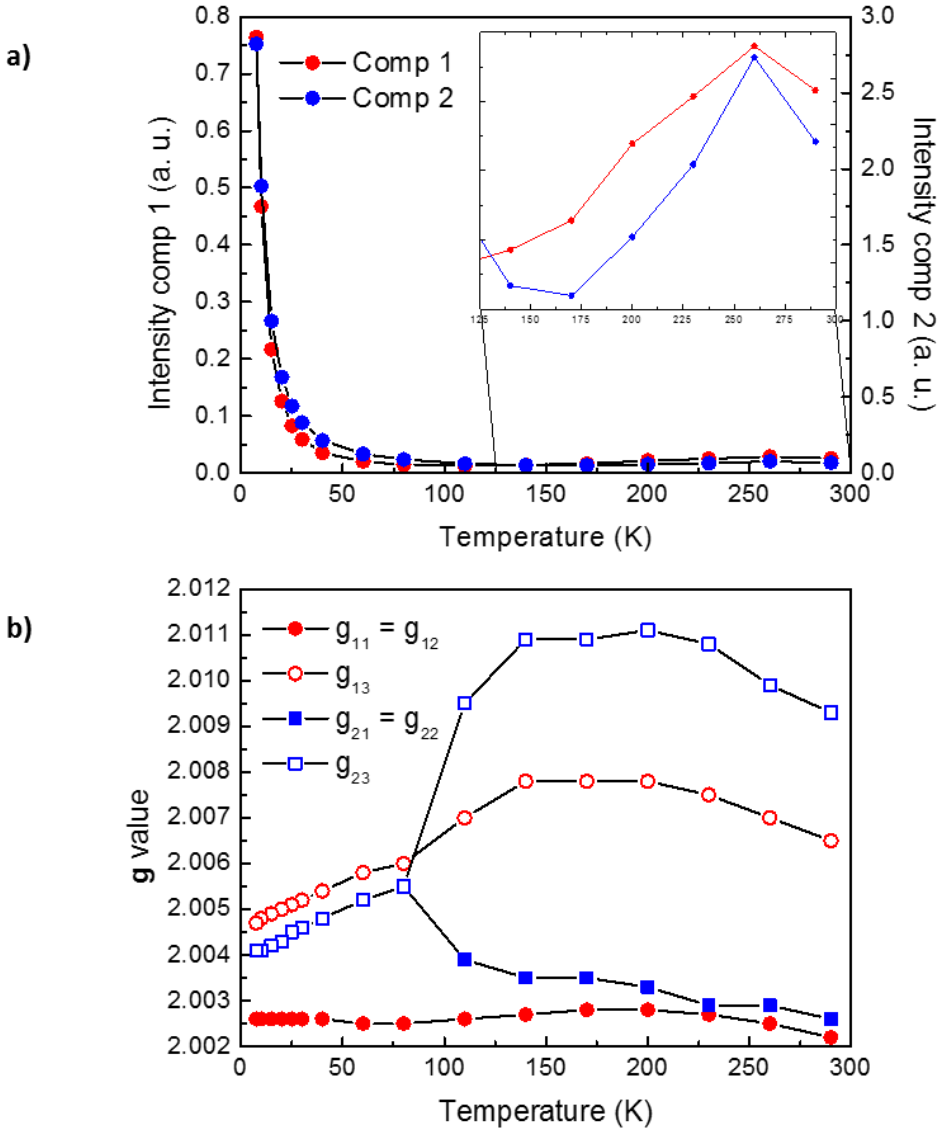

Figure 3.8 (a) intensity variation for each of the two components of the cw-EPR spectrum for sample EHK as function of the temperature (red points = EHK-1, blue points = EHK-2). The inset shows an enlargement of the graph at higher temperatures. (b) g-principal values variation for each of the two components of the cw-EPR spectrum as function of the temperature (red points = EHK-1, blue points = EHK-2).

For our samples, the parameters of the simulations are reported in Tables 3.3, 3.4, 3.5 and 3.6. EH is the only one which displays Dysonian lineshape, typical of conductive samples with particles, or clusters of particles with good electric contact and with dimension larger than the skin depth dependent on the microwave frequency [20] (about 3 µm at X band for bulk graphite [21]). Component EH-1 (82%) was even fitted with the typical lineshape for bulk graphite [21] but in which the anisotropy of the $\boldsymbol{g}$-tensor is lost. As for graphite, an indication of the good conductivity of the sample is given by the significant deterioration of the Q-factor value of the EPR cavity on introduction of a small amount of sample.
The other samples are also conductive, since during sample insertion the deterioration of the Q-factor was observed, but the cw-EPR spectra show Lorentzian lineshapes. This indicates that either the dimension of the crystallites is very small compared to the skin depth, or that the macroscopic conduction (the mobility of the electrons by jumping between crystallites) of the samples is much lower.
As regards the other samples, only EHK shows anisotropy of the $\boldsymbol{g}$-tensor, with typical values observed in nanographitic samples [22]; in the other cases (EK and commercial RGO) only isotropic signals were observed.
Further information on the nature of the signals is derived from the analysis of the temperature dependence of the cw-EPR spectra, and in particular of the intensity and the $\boldsymbol{g}$-tensor of the different components (Figures 3.5, 3.6, 3.7 and 3.8). As a matter of fact we can easily distinguish electrons in semiconductors bands from those in localized paramagnetic states, since on lowering the temperature the intensity of the EPR signals of the first ones decreases [23], whereas it increases for paramagnetic centers [18].
In general, starting from room temperature, the intensity of the spectra decreases till 100-150 K. For sample EH, below 140 K the signal-to-noise ratio is too weak to be detected. As already pointed out, we associate a decrease of EPR intensity to a decrease of unpaired electrons in the semiconductor band. A different behavior is shown by the component EK-1, whose intensity slightly increases, thus showing a small contribution from unpaired electrons in different states. Below 100-150 K the intensity increases for both components with Curie (non-interacting electrons) or Curie-Weiss (electron with spin-spin interactions) behavior [24,25].
The change in the trend between high and low temperature, is associated with a change of the g-values of the EPR lines. We must conclude that these are due to a complex superposition of signals from different species, whose relative intensity varies in opposite way.

3.3.4 - Pulsed EPR

At low temperatures we tried to separate contributions due to species with long spin relaxation times. An analogue attempt at room temperature was unsuccessful.

For samples EK, EHK and RGO we performed pulsed experiments at 80 K; for samples EH and for SM no echo signal could be detected because of the too low signal-to-noise ratio due to the high conductivity of both samples [26]. At first we have recorded ED-EPR spectra. Very similar spectra have been obtained for samples EK, EHK and RGO. In Figure 3.9a we report the spectrum for sample EHK. The ED-EPR spectra for samples EK and EHK are composed of two components with Gaussian profile and with axial $\boldsymbol{g}$-tensor, while for sample RGO one Gaussian component with isotropic $\boldsymbol{g}$ was enough to simulate the spectrum. The shape of the spectra was observed to be independent of the delay time between the two pulses. Gaussian lineshapes are normally obtained in the presence of unresolved weak hyperfine interactions. The parameters obtained from the fitting of the spectra are collected in Table 3.7.

The analysis has then been completed by acquiring the phase memory time (T_M), the spin-lattice relaxation time (T_1) and the hyperfine couplings of the unpaired electrons with magnetic nuclei (^{1}H, ^{13}C) for EK, EHK and RGO.

Hahn decays (HD) and inversion recovery (IR) experiments for the determination of T_M and T_1 gave exponential traces that were fitted by using biexponential decay functions:

$$I(t) = A_1 e^{-t/\tau_1} + A_2 e^{-t/\tau_2} \tag{3.3}$$

where A_i and τ_i are respectively the amplitude and the time constant of the i-th component. The parameters from the fitting of the traces are collected in Table 3.8.

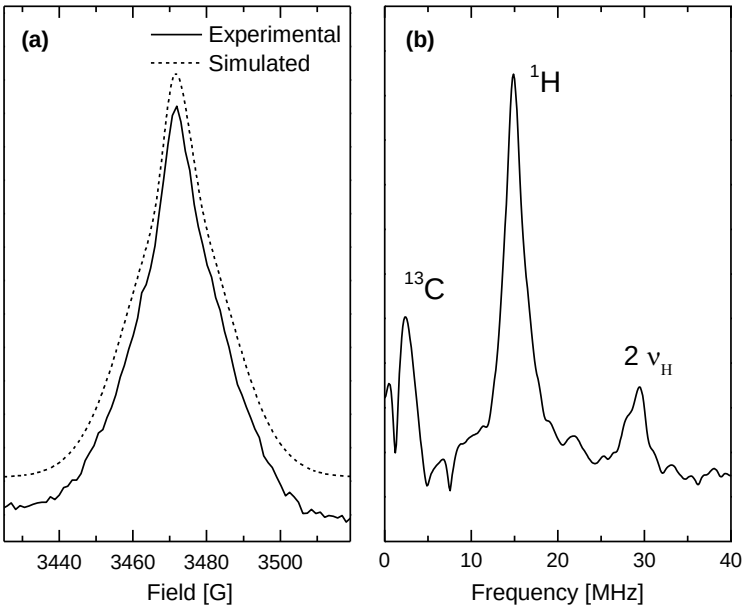

Figure 3.9 a) ED-EPR of the sample EHK with $\tau = 200$ ns. Two species are present with g-values typical of organic radicals. b) 2p-ESEEM spectrum of sample EHK, it shows the presence of coupled C and H atoms. The spectra are representative also of the samples EK.

Table 3.7 Relevant simulation parameters of the ED-EPR spectra at 80 K. For each contribution i, the linewidth Γ, the perpendicular (subscript label a) and parallel (subscript label b) components of the $\boldsymbol{g}$-tensors are reported (isotropic or parallel, g_{ia}, and perpendicular, g_{ib}). The relative abundance of the species (C_i) is indicated.

Sample	$\%C_1$	g_{1a}	g_{1b}	Γ_1 (G)	g_{2a}	g_{2b}	Γ_2 (G)
RGO	100	2.0038	/	1.6	/	/	/
EK	13	2.0059	2.0034	2.5	2.0020	2.0097	11.8
EHK	9.2	2.0058	2.0018	2.4	2.0040	2.0049	13.3

The HD traces show a modulation due to nuclear interactions with the electron spins. The Fourier transform (FT) of the modulation part resulted in the 2p-ESEEM spectra of the samples (see for example Fig. 3.9b). From these spectra we found the same type of signals for the three samples (EK, EHK and RGO). The spectrum shows two groups of signals, one centered at the resonance frequency of protons (centered at the Larmor frequency of 14.9 MHz) and the other at that of ^{13}C nuclei (3.9 MHz). The double frequency peak of protons is visible at 30 MHz. The proton signal, for all samples, has a width of about 5 MHz meaning that the hyperfine coupling constant with the protons is about 1.8 G.

3.4 - Discussion

A qualitative view of the EPR results clearly show that each system has peculiar characteristics ranging between those of the two reference materials: SM and RGO. A more careful overview, given by the use of XRD, Raman and EPR spectroscopies, shows that the samples are rather complex, presenting different structures. The aim was that of searching the presence of analogous signals in all the studied samples, to eventually identify correlated local structures to the observed signals.
First of all we rationalize the presented results, by discussing the presence of molecular structures and their properties.
Graphite: it represents the "bulk" boundary for the samples studied in this work. It was first studied by EPR techniques by Wagoner in 1960 [21] and with Raman spectroscopy by Tuinstra in 1970 [10]. The EPR signal of bulk graphite is due to electrons that are excited to the conduction band, leaving holes behind [21]. The statistics of this system determines a general linear decrease of the magnetization with the lowering of the temperature, reaching a non-zero value at $T = 0$ K because of a contribution from a Pauli-type magnetization that is temperature-independent [27]. For crystallites with dimension above about 3 μm, the value of the average skin depth for graphite [21], the mobile conduction electrons of the particles show a Dysonian EPR-lineshape, due to the motion of the electrons inside and outside the fraction of the sample accessible to the microwave radiation [19,20]. For graphitic

Table 3.8 Fitting parameters of the HD and IR traces at 80 K for samples RGO, EK and EHK.

Sample	Hahn Decay			Inversion Recovery		
	A_1/A_2	τ_1 (μs)	τ_2 (μs)	A_1/A_2	τ_1 (μs)	τ_2 (μs)
RGO	1.88	0.466	3.897	0.60	0.919	7.223
EK	1.09	0.316	1.780	0.67	3.160	30.10
EHK	1.36	0.228	1.180	0.55	1.830	17.20

materials the $\boldsymbol{g}$-tensor is highly anisotropic with axial symmetry. The g-components perpendicular to the crystal c-axis are almost temperature-independent and their values are near g_e. On the other hand, the parallel component of the tensor is strongly dependent on the temperature with typical values that can reach 2.10 at low temperature for bulk systems [21] and 2.02-2.03 for nano-scale systems [23]. In the latter case, an orientational disorder in the stacking of the graphenic planes can change the g-values. The parallel component of electrons in π-type orbitals is particularly affected, because of the interaction between graphene planes that is responsible for the spin-orbit coupling. For densely packed materials that present a good inter-particle contact, motional averaging can also affect the g-values.

Single layer graphene: in pure, single layer graphene, obtained by mechanical exfoliation of graphite, EPR signal due to mobile electrons were observed by Ćirić in 2009 [28]. Unlike graphite, this signal is symmetric (no skin effect) and it is characterized by an isotropic g-value of 2.003-2.004, closely matching the free electron value g_e. For graphene, as well as for graphite, it is well known that the limited extension of the π-system generates the so-called edge states, located, in terms of energy, at the contact points between the conduction and the valence bands [29]. These states are not extended throughout the whole π-system, being spatially localized in the proximity of the graphene border. Edge states bear unpaired electrons and are expected to strongly exchange with conduction electrons [30] and with other localized spins [31], thus giving raise to narrow Lorentzian lines.

Radicals: unpaired electrons attributable to radicals are expected to be produced in graphene-like materials, under strongly reducing conditions. By excluding carbon dangling bonds, observed in diamond-like materials [32] with $g = 2.0027$, the radicals are likely delocalized systems constituted by carbon, hydrogen and adventitious oxygen. Such radicals have generally isotropic or low-anisotropic $\boldsymbol{g}$-tensors with typical values of 2.003-2.004 [33] and can exhibit hyperfine interactions to paramagnetic internal atoms (^{1}H and ^{13}C) of the order of MHz to kHz, according to the extent of the delocalization.

In the light of the introduction to this section, from an easy inspection of the EPR spectra, it is clear that sample EH has rather different behavior with respect to the other exfoliated graphites. The peculiarity of this sample is the high mobility of the electrons through the material, giving rise to a strong decrease in the susceptibility on lowering of the temperature and to a clear Dysonian lineshape due to the larger

dimensions of the flakes, compared with the skin depth for graphitic materials. High conduction can be retained through two different mechanisms: delocalization, related to the extent of the wavefunction, and hopping. Because hopping mechanism is likely to be the same in all the materials, we conclude that extension of the wavefunction in large flakes, and likely π-stack interactions, must be responsible of the high mobility of electrons like in graphitic materials. The general reduction of the intensity of the EH-2 component, the dominant contribution to EPR intensity, sustains this hypothesis, backed by XRD and Raman results. The increase in the intensity of component EH-1 shows that some paramagnetic species are also present. Since the characteristics of this sample are closer to SM than to RGO, it is evident that the expansion by treatment with strong acids is not convenient as compared to other methods, for the production of materials with electronic properties resembling those of single layer graphene.

Samples EK and EHK have a more defective sp^2 structure, as suggested by their similar $A(D)/A(G)$ ratio in the Raman spectra, which is larger than that observed for sample EH. This means that they consist of smaller flakes and/or are characterized by a higher concentration of point defects. This becomes particularly evident for RGO. There is a discrepancy between lateral dimensions obtained by XRD and Raman, but that has already been reported [34].

Both Raman and XRD analyses highlight that samples EK and EHK are mixtures of structures, some of which display few-layers stacked graphene sheets, and these are of course the most interesting materials. XRD shows also that exfoliation is not a homogeneous process that leaves some unreacted graphitic structures. We then comment on the information coming out by EPR analysis. The two samples show a wider variety of EPR signals, with some analogies, but also differences, we focus mainly on sample EK.

The EPR intensity of sample EK shows an initial decrease with the lowering of the temperature, passing through a minimum, and quickly rising at the lowest temperatures. This trend can only be interpreted is one assumes the presence of both mobile charge carriers and localized electrons. Regarding the firsts, contributing to EPR at high temperatures, the spectra can be well reproduced using two components with Lorentzian lineshape and isotropic $\boldsymbol{g}$-tensor, close g_e. It is unlikely that this value is obtained by motional averaging, as it should be larger, moreover, the type of lineshape supports the hypotheses of a limited mobility of the electrons, still in the conduction band. We note that one of the two components (EK-2), by far the dominant one, corresponds closely to those found by Ćirić, and to those of RGO sample. In both cases, Lorentzian lineshapes in the range $g = 2.003$ - 2.004 have been found, with a decrease of the signal by lowering of the temperature. This component can be associated to the most exfoliated fraction of the sample, responsible for the broad, lower-angle contribution of the (002) reflection in the XRD diffractogram.

The other component of EK sample (EK-1) has an unusual g-value, lower than g_e. At the moment we have no clear explanation for this, but we note that such low values are present in other carbon allotropes, like fullerenes and carbon nanotubes, where even lower values can be found [35-37]. A low g-value has been observed also for component EK-1. These have been associated to the bending of the plane, but to confirm this hypothesis further investigations are required (see chapter 5). We can conclude that the signals of sample EK at high temperatures are likely due to electrons in graphene-like systems, with well separated layers display only little electronic interactions.

At low temperatures, EK resembles RGO better than scotch-tape graphene, the latter having a small Curie-like contribution. The similarity is likewise reflected in the $A(D)/A(G)$ ratio of the Raman spectra. This is not surprising, since it is known from literature that graphene produced by Hummers method is very defective [38]. Indeed, the rise of the intensity due to Curie contributions is much more evident, compared to the material obtained by Ćirić. The disentangling of the signal of sample EK at low temperature enabled to determine the presence of different contributions. Spin-echo pulse techniques allowed to identify the contributions due to slow relaxing spins, which are estimated to be minority as judged by the echo intensity with respect to cw-EPR intensity. They cannot be edge states, as electrons in these states exhibit strong interactions with other electrons in conduction band, resulting in spin relaxation times $T_1 = T_2$ [39]. Moreover, they cannot be the major contribution to the cw-EPR spectra.

Slow relaxing species give an inhomogeneously-broadened spectrum from which it is possible to extract hyperfine interactions with protons and ^{13}C, as determined by the ESEEM spectrum. Moreover, these species are characterized by g-values typical of π-conjugated molecules. We conclude that these signals must be due to sites that have been involved in reactions of the material with hydrides, likely during exposition to the strong reductive environment used for the preparation of the material.

The characteristics of the dominant contribution to the cw-EPR at low temperatures, unlike spin-echo, suggest that they are indeed fast relaxing electrons, and that the linewidth is affected by homogeneous broadening. In all, we propose that the signals of the cw-EPR spectra are then due mostly to electrons in edge states.

3.5 - Conclusions

We presented a comparative study of a single-layer commercial reduced graphene oxide and graphene-like materials produced by different exfoliation processes of graphite. EPR measurement highlighted profound electronic differences between the samples, determined by the different preparation routes. As expected, the samples presented characteristics intermediate between graphite and graphene.

We were able to separate the contribution to the final EPR spectra of conduction band electrons from electrons related to different types of defects. Both EPR and Raman analyses showed large contributions from defects.

The samples present some analogies. In all cases, signals due to localized electrons were observed in the cw spectra, expecially at lower temperatures, meaning that these electron are typical of such systems. Also the molecular like radicals highlighted by the pulsed techniques were present in all samples since all the ED-EPR spectra were similar and also the hyperfine coupling observed with ESEEM spectroscopy. The main differences observed concerned conduction electrons that were different according the degree of order and the interlayer separation of different materials.

Defects in the basal plane affect the electronic properties in different ways, in fact EPR showed that they derive both from edge states and molecular-type species, the latter characterised by the presence of nearby hydrogen, likely introduced in the structure during the production of the material in strong reductive conditions.

Acid exfoliation was the less effective method to obtain good separation of the graphene sheets. On the other hand, intercalation with potassium, followed by reaction with ethanol produced a sample with stronger affinity to RGO in that they display large contribution from conduction electrons and similar $\boldsymbol{g}$-values and lineshapes. This is an indication that the properties of conduction electrons of EK are closely related to those of graphene, that we associate to a better separation of the graphene layers.

References

[1] WS Hummers Jr, RE Offeman. Preparation of graphitic oxide, J.Am.Chem.Soc. 80 (1958) 1339-1339.

[2] D Chung. Exfoliation of graphite, J.Mater.Sci. 22 (1987) 4190-4198.

[3] MJ Allen, VC Tung, RB Kaner. Honeycomb carbon: a review of graphene, Chem.Rev. 110 (2009) 132-145.

[4] K Novoselov, AK Geim, S Morozov, D Jiang, Y Zhang, S Dubonos, et al. Electric field effect in atomically thin carbon films, Science. 306 (2004) 666-669.

[5] Y Hernandez, V Nicolosi, M Lotya, FM Blighe, Z Sun, S De, et al. High-yield production of graphene by liquid-phase exfoliation of graphite, Nature Nanotechnology. 3 (2008) 563-568.

[6] S Stankovich, DA Dikin, GH Dommett, KM Kohlhaas, EJ Zimney, EA Stach, et al. Graphene-based composite materials, Nature. 442 (2006) 282-286.

[7] G Parhasarathy, AS Collins, T Chetty. Natural graphite from neoproterozoic psammitic gneiss, Inanalo mountain, southern Madagascar, Journal of the Geological Society of India. 68 (2006) 176-180.

[8] N Kumar, A Shukla, J Singh, MK Patra, P Ghosal, SR Vadera. Simple Route for Synthesis of Multilayer Graphene Nanoballs by Flame Combustion of Edible Oil, Graphene. 1 (2013) 63-67.

[9] A Patterson. The Scherrer formula for X-ray particle size determination, Physical review. 56 (1939) 978.

[10] F Tuinstra, JL Koenig. Raman spectrum of graphite, J.Chem.Phys. 53 (1970) 1126.

[11] AC Ferrari, DM Basko. Raman spectroscopy as a versatile tool for studying the properties of graphene, Nature nanotechnology. 8 (2013) 235-246.

[12] I Calizo, S Ghosh, W Bao, F Miao, C Ning Lau, AA Balandin. Raman nanometrology of graphene: Temperature and substrate effects, Solid State Commun. 149 (2009) 1132-1135.

[13] MS Dresselhaus, A Jorio, M Hofmann, G Dresselhaus, R Saito. Perspectives on carbon nanotubes and graphene Raman spectroscopy, Nano letters. 10 (2010) 751-758.

[14] AC Ferrari. Raman spectroscopy of graphene and graphite: disorder, electron–phonon coupling, doping and nonadiabatic effects, Solid State Commun. 143 (2007) 47-57.

[15] D Graf, F Molitor, K Ensslin, C Stampfer, A Jungen, C Hierold, et al. Spatially resolved Raman spectroscopy of single-and few-layer graphene, Nano letters. 7 (2007) 238-242.

[16] Y Li, Z Li, PK Shen. Simultaneous Formation of Ultrahigh Surface Area and Three-Dimensional Hierarchical Porous Graphene-Like Networks for Fast and Highly Stable Supercapacitors, Adv Mater. (2013).

[17] PW Atkins, J De Paula, Atkins' physical chemistry, Oxford University Press Oxford 2006.

[18] NM Atherton, N Atherton, Electron spin resonance: theory and applications, Ellis Horwood Chichester 1973.

[19] G Feher, A Kip. Electron spin resonance absorption in metals. I. Experimental, Physical Review. 98 (1955) 337.

[20] FJ Dyson. Electron spin resonance absorption in metals. II. Theory of electron diffusion and the skin effect, Physical Review. 98 (1955) 349.

[21] G Wagoner. Spin resonance of charge carriers in graphite, Physical Review. 118 (1960) 647.

[22] M Tommasini, C Castiglioni, G Zerbi, A Barbon, M Brustolon. A joint Raman and EPR spectroscopic study on ball-milled nanographites, Chemical Physics Letters. 516 (2011) 220-224.

[23] A Barbon, M Brustolon. An EPR Study on Nanographites, Applied Magnetic Resonance. 42 (2012) 197-210.

[24] AF Orchard, Magnetochemistry, Oxford University Press 2003.

[25] M Ruitenbeek, A Barbon, E Van Faassen, J Geus. Evidence for a new type of vanadyl pairs in (VO) 2P2O7: an ESR and magnetisation study, Catalysis letters. 54 (1998) 101-104.

[26] M Brustolon, Electron paramagnetic resonance: a practitioner's toolkit, John Wiley & Sons 2009.

[27] NW Ashcroft, ND Mermin, Solid State Physics, Saunders College, Philadelphia, 1976.

[28] L Ćirić, A Sienkiewicz, B Nafradi, M Mionić, A Magrez, L Forro. Towards electron spin resonance of mechanically exfoliated graphene, physica status solidi (b). 246 (2009) 2558-2561.

[29] M Fujita, K Wakabayashi, K Nakada, K Kusakabe. Peculiar localized state at zigzag graphite edge, Journal of the Physical Society of Japan. 65 (1996) 1920-1923.

[30] VJ Joly, K Takahara, K Takai, K Sugihara, T Enoki, M Koshino, et al. Effect of electron localization on the edge-state spins in a disordered network of nanographene sheets, Physical Review B. 81 (2010) 115408.

[31] M Braun, P Struck, G Burkard. Spin exchange interaction with tunable range between graphene quantum dots, Physical Review B. 84 (2011) 115445.

[32] D Keeble, B Ramakrishnan. Electron paramagnetic resonance characterization of diamond films fabricated with different methane concentrations, Appl.Phys.Lett. 69 (1996) 3836-3838.

[33] BH Bielski, JM Gebicki, Atlas of electron spin resonance spectra, Academic Press 1967.

[34] HR Matte, K Subrahmanyam, C Rao. Novel magnetic properties of graphene: presence of both ferromagnetic and antiferromagnetic features and other aspects, The Journal of Physical Chemistry C. 113 (2009) 9982-9985.

[35] P Allemand, G Srdanov, A Koch, K Khemani, F Wudl, Y Rubin, et al. The unusual electron spin resonance of fullerene C60 anion radical, J.Am.Chem.Soc. 113 (1991) 2780-2781.

[36] MM Khaled, RT Carlin, PC Trulove, GR Eaton, SS Eaton. Electrochemical Generation and Electron Paramagnetic Resonance Studies of C60-, C602-, and C603, J.Am.Chem.Soc. 116 (1994) 3465-3474.

[37] A Thess, R Lee, P Nikolaev, H Dai, P Petit, J Robert, et al. Crystalline ropes of metallic carbon nanotubes, Science. 273 (1996) 483-487.

[38] V Singh, D Joung, L Zhai, S Das, SI Khondaker, S Seal. Graphene based materials: past, present and future, Progress in materials science. 56 (2011) 1178-1271.

[39] MA Augustyniak-Jabłokow, K Tadyszak, M Maćkowiak, S Lijewski. ESR study of spin relaxation in graphene, Chemical Physics Letters. (2012).

CHAPTER 4 - EPR CHARACTERIZATION OF GRAPHENE-LIKE MATERIALS: PURE AND N-DOPED GRAPHENE QUANTUM DOTS

4.1 - Introduction

In the previous chapter, we have reported a study with EPR techniques of chemically exfoliated graphites, that were composed essentially of carbon atoms, and of a RGO where we characterized the EPR-active defects that can be found in these materials. In this chapter, we study the defects that are created by introducing heteroatoms in the graphenic honeycomb structure, in particular nitrogen. By electrochemical methods it was possible to substitute carbon atoms with nitrogen atoms of graphene quantum dots (GQD). The resulting materials are highly defective, and the defects that we find here derive both from carbon structures as well as from the presence of the nitrogen. We then compared the results obtained by analogue materials with and without nitrogen doping.

Doping of graphene was considered by chemists because, by trying to exploit graphene as a support for chemical reaction, or even as a catalyst, they had to face the fact that pure graphene itself is not very reactive and all reactions that involve the presence of graphene-like materials exploit the defects or the edge states that are present in the materials. Then a countless number of studies has been published on functionalized or doped graphene and on composite materials (see for example ref.s [1-8]) showing that by chemically modifying graphene it's possible to tune many of its chemical and physical properties and, above all, its reactivity. Doping of graphene with nitrogen introduces in a stoichiometric manner a given number of extra electrons (n-doping), as each nitrogen substituting a carbon increase the number of π-electrons by one unit.

Indeed one of the most studied chemically modified graphene material is N-doped graphene [9]. This material can be obtained in several ways, for example by electrochemical reaction with NH_3 [10], exposure to nitrogen plasma [11], chemical vapor deposition on metals using a mixture of hydrocarbons, hydrogen, and nitrogen-containing molecules [12-14], pyrolysis of polymers [15], solvothermal synthesis [16], and the chemical reaction of GO [17]. N-doped GQDs is so important because, unlikely pure graphene, it is very active as catalyst in many reaction including oxygen reduction reaction [9,13].

Other heteroatoms have been proposed as dopant for graphene, in particular boron, sulfur and fluorine [18,19], and also a combination of them [20-22].

Another type of graphene-like materials that is currently studied because of its outstanding properties is graphene quantum dots (GQDs). This new materials can be

considered as small sp^2 carbon flakes with a thickness of few graphene layers and lateral dimension below 10 nm. These GQDs can be considered as large molecules. They behave as semiconductors with the HOMO-LUMO energy-gap that depends on the molecular size. GQDs, as well as other inorganic QDs, because of their tunable energy gap, have very interesting optical properties [23]. They also can be used to build nanocomposite materials with improved chemical and physical properties.
In the same way as graphene, also GQDs can be functionalized with different chemical species or doped with heteroatoms, like nitrogen, boron or sulfur. These doped GQDs have the properties of both chemical modified graphene (higher reactivity, solubility in polar solvents, catalytic activity, etc) and also of nanosized materials (tunable optical properties, can be used as building blocks to obtain other materials etc.)

4.2 - Experimentals

4.2.1 - Materials

Pure and doped graphene quantum dots (GQDs) were synthetized electrochemically. As a result of a collaboration with Prof. S. Agnoli at the Chemical Science Department of the University of Padua, the synthesis of the materials was developed and carried out by M. Favaro and is reported in [24,25]. At first graphene oxide (GO) microflakes were prepared using the modified Hummers reaction [26,27]. The size of the flakes ranges from 1 to 5 µm (SEM analysis).
The synthesis of the GQDs was then carried out in a standard three-electrode electrochemical cell using a Pt ring as the counter electrode and a saturated Ag/AgCl/Cl^- as the reference electrode. The potential was cycled between ±3.000 V at a scan rate of 500 mV/s. A GO thin film was deposited on a polished glassy carbon substrate to obtain the working electrode. All the procedure was done at 25 °C in an aqueous medium. To obtain the nitrogen-doped GQDs (N-GQDs) the dopant precursors (ethylenediamine and 1,10-phenantroline) were added to the electrolyte

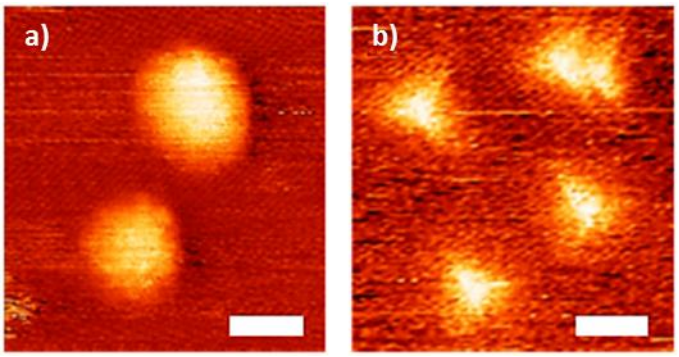

Figure 4.1 STM topographies (10 × 10 nm) of pure (a) and N-doped (b) GOQDs at the HOPG/air interface. The scale bar is 2 nm. Figure adapted from [26]

solution to provide the doping heteroatoms. The products (GQDs and N-GQDs) were finally purified and lyophilized to obtain a white-yellowish powder.
After the preparation, the quantum dots samples were analyzed with XPS to obtain their chemical composition and with STM to get information about the size of the flakes. From XPS measurements it was possible to determine the percentage of doping for the N-GQDs sample, that is 5.1 %. The STM images are reported in Figure 4.1. GQDs flakes have circular shape while the N-doped flakes have a triangular shape. All flakes have an average size of about 2 nm and a thickness between 0.4 and 0.6 nm typical of a single graphene layer.

4.2.2 - EPR measurements

The cw and pulse EPR measurements were obtained with an X-band Bruker ELEXSYS spectrometer, equipped with a dielectric resonator and a nitrogen/helium gas-flow cryostat for low temperature measurements. The powder samples were placed inside 2 mm ID quartz tubes and sealed under vacuum after the full removal of the adsorbed gases. The EPR signals were followed as function of temperature (290 - 300 K), from room temperature to about 40 K. The magnetic field was calibrated using a standard with a known g-factor (LiTCNQ).
The pulse experiments were performed using the standard pulse sequences: 2p-ESE for Hahn decay and for ESEEM, and inversion recovery (IR), for the measurement of T_1. The resonance field was set at the maximum of the EPR intensity. The echo-detected EPR (ED-EPR) spectra were obtained by recording the 2p-echo intensity as a function of the magnetic field at a delay of 200 ns. 2p-ESEEM spectra were obtained by Fourier transforming the modulation of the HD, after a proper reconstruction of the signal taking into account the instrumental dead time. The pulse ENDOR spectra were collected using an ENDOR dielectric resonator and an ENI A300RF power amplifier. The experiments were performed using the Davies sequence, $\pi - T - \pi/2 - \tau - \pi - \tau - echo$ with a RF π pulse applied during the delay T [28]. We used a mw $\pi/2$ pulse of 100 ns, a RF π pulse of 10000 ns, $\tau = 500$ ns and $T = 20000$ ns.

4.2.3 - Simulation of EPR spectra

The simulations were obtained by a homemade program, written in Matlab, that gives as output the relevant EPR parameters for a variable number of species.
We considered the presence of species with only $\boldsymbol{g}$--anisotropy, thus the simulations were done by using equation 2.16 (chapter 2), where the lineshape profile $f(B)$ for the different species could be either Lorentzian or Gaussian. Best fits were obtained by using two species.

4.2.4 - DFT calculations

All computational calculations have been carried out on isolated molecules based on DFT and adopting a B3LYP hybrid functional, which is known to provide reliable

equilibrium molecular structures for radicals [29], in particular all the equilibrium molecular geometries and the hyperfine coupling constants (hfccs) reported in our work have been obtained with the B3LYP/6-311G** method inside the *Gaussian09* package [30].

4.3 - Results

4.3.1 - cw-EPR

We recorded the cw-EPR spectra of sample GQDs and N-GQDs in the range 300-80 K. The spectra recorded at the highest and lowest temperature are reported in Figure 4.2. We determined the total spin concentration of the samples at room temperature

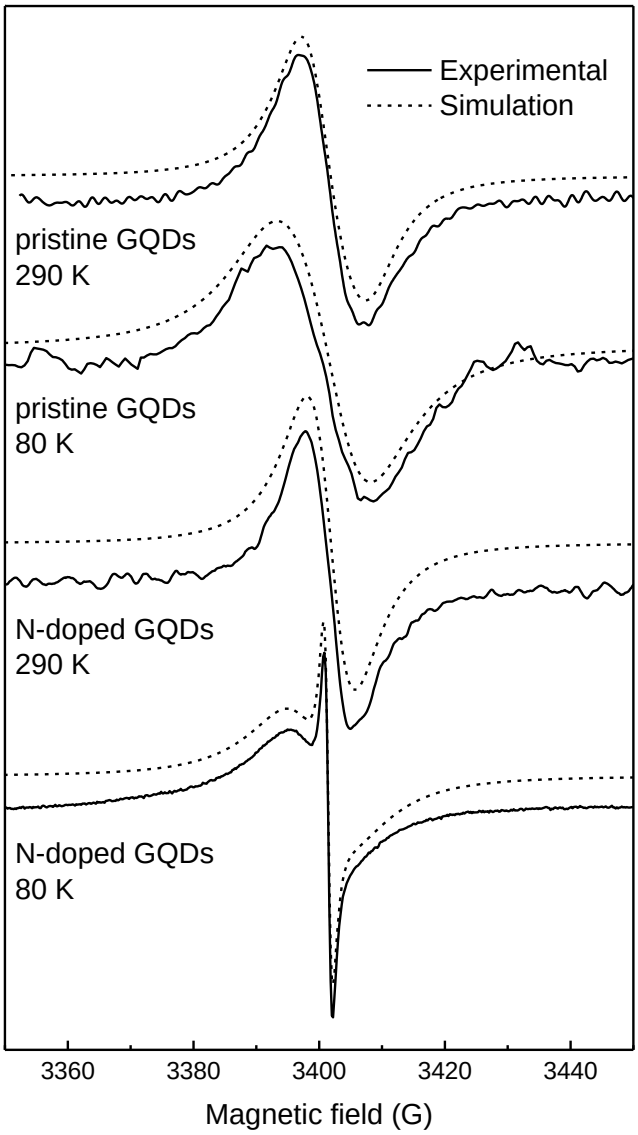

Figure 4.2 Representative cw-EPR spectra of samples GQDs and N-GQDs together with their simulations. the acquisition temperatures are reported on the spectra.

Table 4.1 Parameters obtained from the simulations of the cw-EPR spectra of samples GQDs and N-GQDs recorded at 290 K and 80 K. $\%\boldsymbol{C_1}$ is relative percentage of component 1, $\boldsymbol{\Gamma_1}$ and $\boldsymbol{\Gamma_2}$ are the linewidths and $\boldsymbol{g_1}$ and $\boldsymbol{g_2}$ are the $\boldsymbol{g}$-tensors. If one number is indicated in the $\boldsymbol{g}$-tensors column the tensor is isotropic, if two numbers are indicated the tensor is axial. For sample GQDs at 80 K it was not possible to determine carefully the $\boldsymbol{g}$-tensors.

Sample	N° comp.	Lineshape	$\%\boldsymbol{C_1}$	$\boldsymbol{\Gamma_1}$ (G)	$\boldsymbol{g_1}$	$\boldsymbol{\Gamma_2}$ (G)	$\boldsymbol{g_2}$
GQDs, 290 K	1	Lorentzian	100	11.9	2.0047 2.0028	---	---
GQDs, 80 K	1	Lorentzian	100	14.8	n.d.	---	---
N-GQDs, 290 K	1	Lorentzian	100	7.8	2.0044 2.0035	---	---
N-GQDs, 80 K	2	Lorentzian	96	11.0	2.0035	1.4	2.0045 2.0038

by comparing the total area of the cw spectrum with the spectrum of a standard sample of Mn(II). The value we found is $4.0 \cdot 10^{14}$ spin/g for the undoped sample and $3.7 \cdot 10^{14}$ spin/g for the doped one.

From the whole simulation of the spectrum we obtained the presence of different species and, for each of them, its lineshape, linewidth and the $\boldsymbol{g}$-tensor. The parameters obtained from the simulations of the cw-spectra at room temperature and at 80 K are collected in Table 4.1.

For the pure and the doped sample, we observed an increase of the EPR intensity by decreasing of the temperature, typical of a Curie-Weiss-like behavior [31]. On top of this, for the doped sample, at low temperature, another component in the cw-EPR spectra becomes evident, with linewidth of about 1.5 G, isotropic $\boldsymbol{g}$-tensor and same behavior with the temperature (see Fig. 4.2). This component is less saturable than the other, and becomes even more evident at high microwave powers.

4.3.2 - Pulsed EPR

All the pulsed measurements were performed at 80 K or below. For both samples we collected ED-EPR spectra at 80 K. They are reported in Figure 4.3. The spectra have been simulated with the same procedure as for the cw-EPR spectra, after verification that the spectra were not distorted by experimental acquisition conditions, like pulse distance or microwave power. To obtain a good reproduction of the experiments two components with Gaussian lineshape were used. All the parameters obtained from the simulations of the ED-EPR spectra are collected in Table 4.2.

At 80 K we also recorded the Inversion Recovery trace for the determination of the spin-lattice relaxation time (T_1), and the 2p-ESE decay (HD), from which both the phase memory time (T_M) and the ESEEM spectrum were obtained.

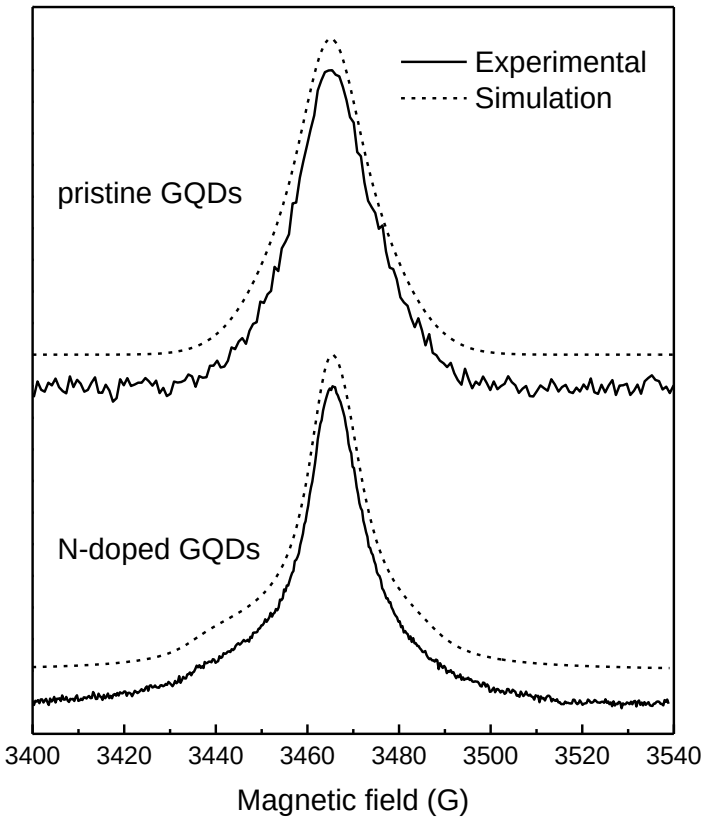

Figure 4.3 Normalized ED-EPR spectra of samples GQDs and N-GQDs recorded at 80 K together with their simulations.

The HD and IR traces were fitted using biexponential decay functions. The parameters obtained from the fitting of the traces are collected in Table 4.3. The 2p-ESEEM spectrum showed the coupling with protons and ^{13}C atoms. From the analysis of the proton signal in the ESEEM spectra we obtained an estimate of the hyperfine coupling constant relative to the coupling with the protons. For the undoped sample we found a value of about 0.7 G while for the doped one of about 1.9 G.

Table 4.2 Parameters obtained from the simulations of the ED-EPR spectra of samples GQDs and N-GQDs recorded at 290 K and 80 K. $\%C_1$ is relative percentage of component 1, Γ_1 and Γ_2 are the linewidths and $\boldsymbol{g_1}$ and $\boldsymbol{g_2}$ are the $\boldsymbol{g}$-tensors. One number is indicated for isotropic $\boldsymbol{g}$-tensors, two numbers are indicated for axial tensors.

Sample	N° comp.	Lineshape	$\%C_1$	Γ_1 (G)	g_1	Γ_2 (G)	g_2
GQDs, 290 K	2	Gaussian	27	10.1	2.0046	23.3	2.0042
GQDs, 80 K	2	Gaussian	17	13.0	2.0045	28.4	2.0041
N-GQDs, 290 K	2	Gaussian	35	7.1	2.0039 2.0052	16.8	2.0045
N-GQDs, 80 K	2	Gaussian	34	7.8	2.0044 2.0030	34.4	2.0042

Table 4.3 Fitting parameters of the HD and IR traces at 80K for samples GQDs and N-GQDs. All the traces were fitted using a biexponential function. $\%C_1$ is relative percentage of component 1, $T_{M,i}$ and $T_{1,i}$ are respectively the phase memory time and spin-lattice relaxation time for the i-th component.

Sample	Hahn Decay			Inversion Recovery		
	$\%C_1$	$T_{M,1}$ (µs)	$T_{M,2}$ (µs)	$\%C_1$	$T_{1,1}$ (ms)	$T_{1,2}$ (ms)
GQDs	31	0.17 ± 0.02	3.20 ± 0.08	29	0.24 ± 0.02	2.78 ± 0.08
N-GQDs	40	0.12 ± 0.01	1.02 ± 0.01	19	0.28 ± 0.01	2.58 ± 0.03

For the N-doped sample, we at first recorded the pulse Mims ENDOR spectrum at 80 K. The spectrum was lacking of the transitions at low frequency, typical of ^{13}C and ^{14}N (0-10 MHz), and only the transition of ^{1}H (around 14.5 MHz ca) was visible, likely because of a fast nuclear relaxation. We then collected the spectrum at 25 K. The 2p-

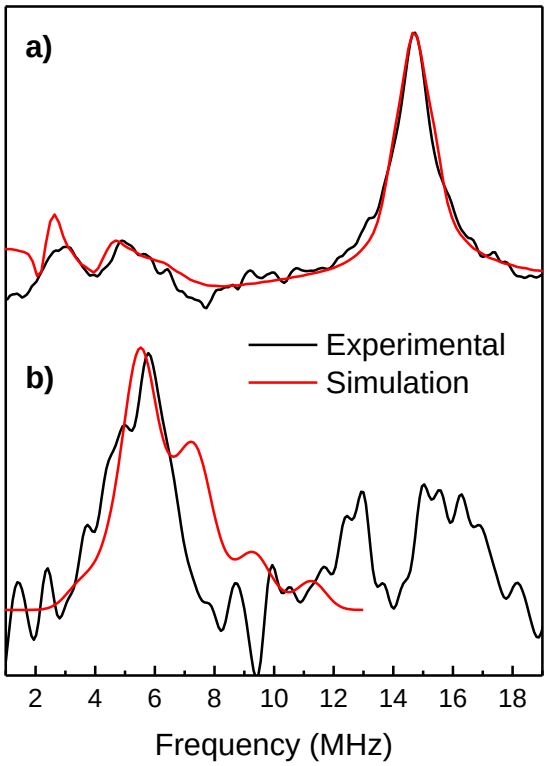

Figure 4.4 a) 2p-ESEEM spectrum of sample N-GQDs in which coupling with nitrogen and hydrogen nuclei are evident; the pulse sequence is 16-200-32-200; b) Davies ENDOR spectrum of sample N-GQDs in which coupling with nitrogen nuclei are evident; the pulse sequence is 200-20000-100-500-200-500 with a RF π pulse of length 10000 ns applied during the delay time of 20000 ns. The red lines are simulated spectra.

ESEEM spectrum and pulse Davies ENDOR spectra are reported in Figure 4.4. They show signals that are relative to the hyperfine coupling with the dopant atoms.
To extract the hyperfine coupling tensor relative to the coupling with the nitrogen atom we simulated both the ESEEM and the ENDOR spectra with home-made programs based on the paper by M. Brustolon et al. [32]. The portion of the 2p-ESEEM spectrum between 2 and 7 MHz was reproduced assuming the coupling with a nitrogen nucleus; attempts to fit this spectrum with a coupled ^{13}C nucleus gave much worse fit. We determined the hyperfine coupling tensor $\boldsymbol{A}$ of the nitrogen atom with the unpaired electron from the simulation of the ESEEM spectrum

$$\mathbf{A} = [6.1 \quad 6.1 \quad 11.5]\, MHz \qquad a_{iso} = 7.9 MHz$$

and we used this same tensor to reproduce the ENDOR spectrum reported in the figure without further optimization steps. The simulation reproduces quite well the shape and position of the nitrogen signals anyway.

4.4 - Discussion

The pure and N-doped graphene quantum dots described in this work have been extensively studied with different techniques in order to fully understand their chemical structure, physical properties and reactivity. All these results can be found in the works by Marco Favaro [24,25].
These systems have a quite small dimension determined by STM [25] between 1.5 and 2.5 nm. The thickness corresponds to that of a graphene single layer. Therefore they can be considered as complex large molecules and their properties are indeed typical of molecular systems rather than of bulk materials. They are semiconductive with a clear gap (HOMO-LUMO separation) which depends strongly on the geometrical size [33].
The samples are quite defective; they consist of a graphitic sp^2 core with edges decorated by several functional groups such as alcohols, carbonyl and carboxyl which is a characteristic of materials obtained by the Hummers method [26]. The pure GQDs have about 21 % of oxygen while the N-doped QDs have 18 % of oxygen and 5 % of nitrogen (values determined by XPS). XPS enabled the determination of the chemical nature of the nitrogen species that are formed during the doping. They are pyridine, pyrrole, graphite and pyridine oxide groups (Fig 4.5) [9,34-36]. Pyridine and pyrrole nitrogens are along the edges of the quantum dots, in hexagonal or pentagonal rings, and contribute to the π-conjugated system with respectively one and two p-electrons. When a nitrogen atom substitutes a carbon atom in the graphene honeycomb layer the nitrogen is called graphite nitrogen; it contribute to the π-system with two p-electron, one more than carbon. Pyridine-oxide nitrogen is along

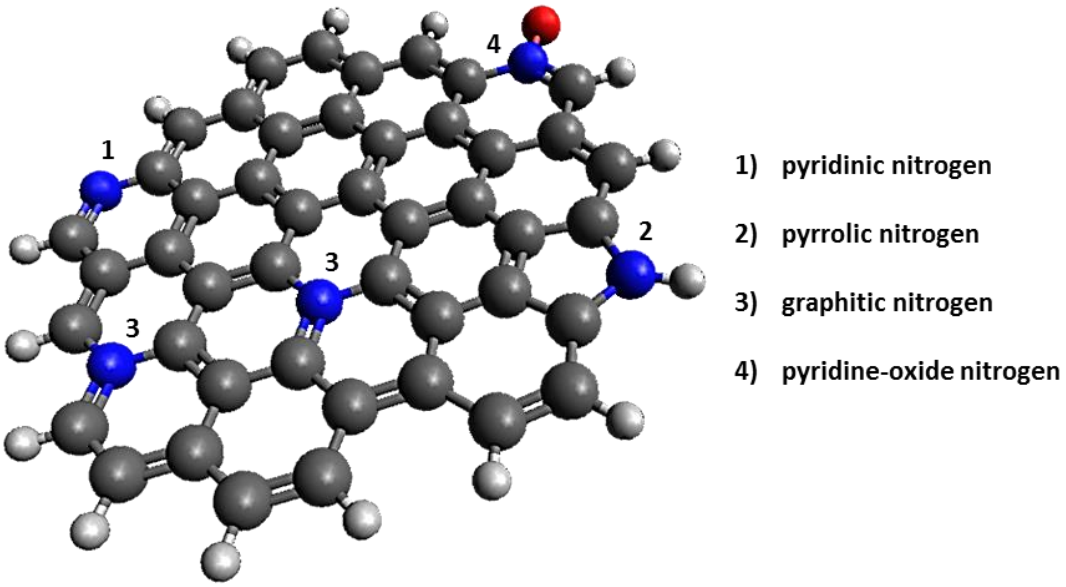

Figure 4.5 Pictorial model of a N-doped graphene quantum dot. The different types of nitrogen that can be present in the sample are enlightened.

the edges, like pyridine nitrogen, but with an oxygen atom directly bound to it; it contributes with one p-electron to the π-system.

Pyrrole nitrogens account for about 45 % of the total nitrogen in the N-doped GQDs, pyridine and graphite nitrogens for 25 and 23 % respectively, the remaining 7 % is nitrogen bound to oxygen.

Up to now, no EPR study on this kind of systems has been published. The interpretation of EPR spectra of carbon-based system such as graphite, graphene and similar compounds is not straightforward, so a careful analysis is required. It is known, from some previous works, that these type of compounds can give quite various EPR signals according to the dimension, shape, presence and type of defects [37-41]. Different types of electrons for large-scale graphene-like materials have been classified and characterized by EPR: mobile electrons (highly delocalized), electron localized at the edge of the flakes or in proximity of defects, whose energy level is at the contact point between the valence and conduction bands, and unpaired electron in molecular-like radicals [42,43]. All these systems have been extensively described in previous works by both a general point of view and focusing on their magnetic properties, so we will not go into detail here, but we will refer to them for our purposes.

GQDs cannot be considered as a bulk material since their size is in the nanometric range where the properties of a material cannot be described by the band theory. In particular, our sample have a lateral dimension of few nanometers [25], so that they can be considered simply al large conjugated molecules. In this case the type of electrons that are present in these systems and that can give rise to an EPR signal, are different. Due to the limited dimension of the particles we do not expect to

observe signals related to mobile charge carriers as we observed in Chapter 3 for the exfoliated graphites. Indeed we didn't find any EPR signal typical of (semi)conductive systems [37,38] with intensity increasing by increasing of the temperature. In our samples, we expected to observe electrons localized in edge states or in structural defects and unpaired electrons in molecular-like radicals. Tadyszak and coworkers [44] in similar systems reported EPR signals of non-interacting delocalized electrons, showing Curie-type paramagnetism. By using both cw and pulse EPR techniques, it was possible to determine the presence of species with different relaxation times and with different concentration, in fact in a cw-EPR spectrum all the signals due to EPR-active electrons are present, whereas in ED-EPR experiments with delay time $\tau = 200$ ns, all the components with relaxation times shorter than 200 ns were filtered away. In the temperature range between room temperature and 80 K pure and N-doped GQDs show cw-EPR spectra with broad components that are quite similar; at room temperature this is the only observable species with a g-factor of ca. 2, typical of organic aromatic systems with low spin-orbit coupling. The Curie-like trend of the EPR intensity with temperature confirms what we stated previously: the signals are not due to conduction electrons as pure graphite or graphene, in agreement with the small dimensions of our samples.

Then we could simulate properly the room temperature cw-spectra using a single Lorentzian line with slightly anisotropic $\boldsymbol{g}$-tensors whose values are between 2.003 and 2.005. These signals could be due to electrons localized in atomic or molecular orbitals, likely π orbitals with different extent [44]; edge states are included in these. The lineshape enables us to exclude the presence of molecular-like radicals since for these we would expect to observe hyperfine coupling with paramagnetic nuclei.

In order to discriminate between localized from delocalized electrons we analyzed the temperature dependence of the linewidth according to the procedure used by Tadyszak and coworkers [44]. For delocalized electrons, we expect an increase of the linewidth at low temperature caused by the fluctuations in the spin-orbit interaction for the electron associated to the scattering processes [44,45], like the scattering at the GQD edges. On the other hand, the linewidth of the EPR signal of localized electron is determined by structure dynamics which involve relaxation processes: such processes are slower at low temperatures, and consequently the lines are narrower.

The linewidths of our major component for both GQD and N-GQD get wider by going from room temperature to 80 K: for pure GQDs they go from 11.9 to 14.8 G whereas for the doped sample from 7.8 to 11.0 G. From these observations, it follows that the cw-EPR signals that we observe at room temperature are due to highly delocalized electrons, and these types of electrons are present in both the GQD and N-GQD.

A difference between the two type of samples is marked by the presence of a narrow signal at low temperature for sample N-GQDs, better visible at high microwave powers. This signal has the same lineshape and trend with the temperature of the

other component. Because of the very narrow linewidth (1.4 G) of this signal at low temperature, as we anticipated before, we assign it to localized electrons. Localization of the wavefunction can be induced by the presence of the nitrogen atoms, having a higher electronegativity. This might represent a kind of potential sink. With this respect, the presence of a nitrogen can be considered as an internal defect, which likely produces edge states inside the graphene structure at a higher concentration than for GQD (see further the results found from DFT calculation). That supports our assignment since we found no narrow line for the undoped GQD sample, even at 80 K. Likely, some localized electrons signal would be observed if we had studied the sample at even lower temperature. For pure graphene, signals due to localized electrons becomes indeed evident for temperatures lower than 50 K [38].

Let's move now to the discussion of the results obtained with the pulsed techniques. As stated before, spin-echo pulse techniques enabled the separation and identification of the species with slow relaxing spin, as fast relaxing spins decay within the instrumental dead time, so that they are not recorded. From the comparison between the ED-EPR spectra (see simulation parameters in Table 4.2) and those used for the cw-EPR (Table 4.1) it is clear that the species observed by ED-EPR are not the same observed by cw-EPR. The species that appear in the pulsed spectra have much lower intensities with respect to the species that appears in the cw spectra, ED-EPR spectra have only slightly different $\boldsymbol{g}$-tensors with respect to the cw ones but their major difference, beyond the intensity, is the lineshape, in fact, ED-EPR spectra were simulated using only Gaussian components while Lorentzian lineshape were used for the cw spectra. Gaussian lineshapes tipically hide unresolved hyperfine interactions. We then used pulse techniques to further characterize these contributions. From the HD and IR measurements we noticed that the species observable with the pulse techniques have T_1 that is three order of magnitude higher than T_M. This applies both for the wide and narrow components of pure and doped samples. This observation, together with the Gaussian lineshape, means that these species are not due to edge or defect states, since for these systems it was reported $T_1 = T_M$ [46]. Therefore, we must conclude that they are molecular-type radicals; this is also in agreement with the results of other pulsed experiments done for similar samples [39,42,43]. In order to confirm this statement we performed hyperfine spectroscopy experiments. If they are indeed molecular radicals and they Gaussian lineshape is due to unresolved hyperfine coupling, with ESEEM and ENDOR techniques we should be able to observe these couplings. The spectra recorded at 80 K indeed show coupling with protons and with ^{13}C nuclei for both samples.

In the ESEEM and ENDOR spectra of the N-doped sample we also expected to observe signals due to the coupling with the nitrogen atoms, but that was not the case, at least at 80 K. To obtain such signals we had to lower further the temperature to 25 K and then we managed to obtain signals of the coupling with the dopant and, from

them, the hyperfine coupling tensor. The knowledge of the tensor gives us very important information about the nature of the nitrogen dopants. To get this, we calculated with DFT the hyperfine coupling tensor for some model molecules that are supposed to be similar to the N-GQDs and compared them with the experimental one.

We considered particles of dimension of about 2 nm and a number of carbon atoms of about 50-70, as determined from STM. We started our calculations on smaller models for sake of computational rapidity and then we kept on with larger systems. We modified the dimension, shape, type of edges and position of the nitrogen dopant inside the molecule. The structure of the molecules that we investigated are collected in Figure 4.6. We tried to include a wide variety of molecules; some of them have a pyridine or pyrrole nitrogen (N01, N02, N06, N07 and N12) others have graphite nitrogen (N03, N04, N05, N08, N09, N10 and N11). Some molecules have only zigzag-type edges while molecules N065, N07 and N09 have also armchair-type edges. Molecules N02 and N12 have the nitrogen atom in a five-membered ring, while all the other have the typical graphene-like structure with all six-membered rings. All molecule have an uneven number of electrons, so are in a doublet state; the only exception is molecule N07 which have 46 π-electron and can be either in a singlet or a triplet state, the geometry and the EPR calculation were done assuming a triplet

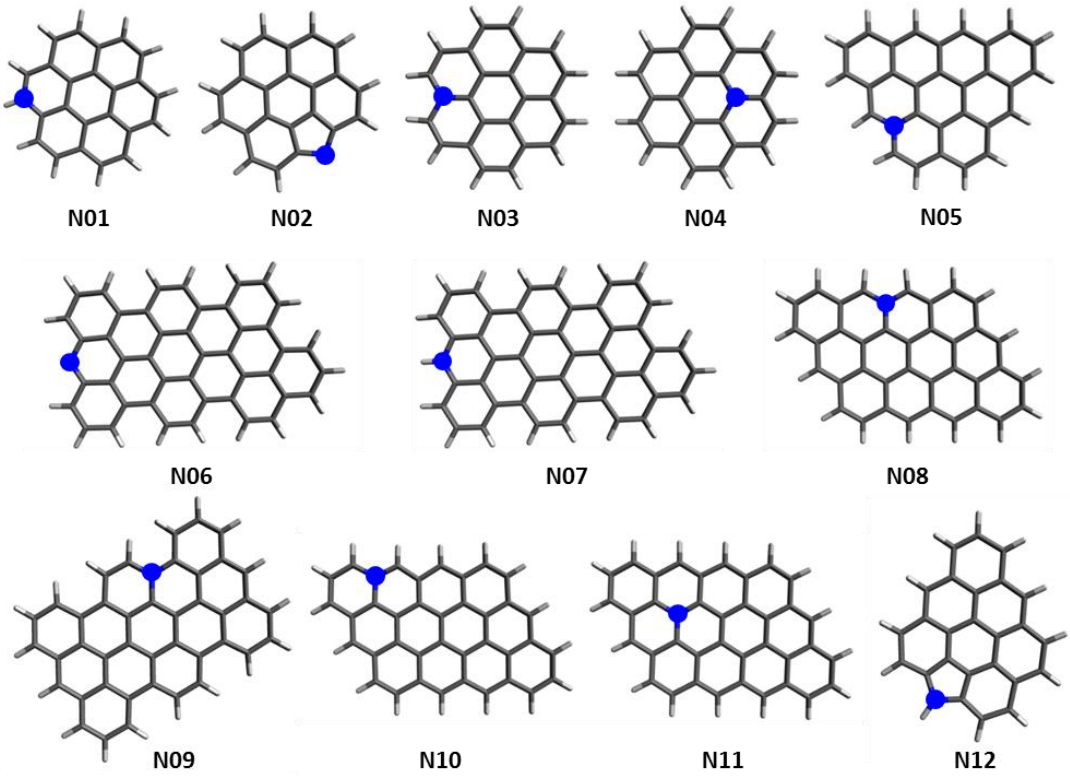

Figure 4.6 Structures of the molecules used as models of the N-GQDs for the DFT calculations. The N atom are represented with the blue circles. The geometries have been optimized with DFT at the B3LYP/6-311G** level. All these molecule have at least one unpaired π electron.

Table 4.4 Hyperfine coupling constants obtained from the DFT calculations. In the table are reported the principal values of the $\boldsymbol{A}$-tensor and the isotropic value.

Molecule	$\boldsymbol{A}$ (MHz)	$\boldsymbol{a_{iso}}$ (MHz)
N01	[-2.69 -2.48 26.70]	7.18
N02	[-1.76 -2.02 55.20]	17.14
N03	[-0.72 -0.66 26.60]	8.41
N04	[-0.87 -0.81 29.88]	9.40
N05	[0.00 0.12 -0.80]	0.23
N06	[-1.36 -1.55 37.52]	11.53
N07	[-0.18 -0.23 5.15]	1.58
N08	[-1.36 -1.20 1.36]	-1.20
N09	[-0.20 -0.15 3.38]	1.01
N10	[-1.90 -1.10 -1.02]	-1.34
N11	[-1.15 -1.06 4.52]	0.77
N12	[-0.93 -0.85 2.46]	0.22

state. For all molecules we obtained the minimum geometries and, starting from them, we computed the hfccs of the unpaired electron with the nitrogen atom. The values are collected in Table 4.4.

One major finding is that the largest constants have been obtained for molecules in which the nitrogen atom is along an edge, but not bound with a hydrogen atom. For molecule N02 we found $a_{iso} = 17.4$ MHz and for molecule N06 $a_{iso} = 11.53$ MHz. In these two molecules, the nitrogen atoms contribute to the π-conjugated system with only one p-electron, regardless of whether they are in a pentagonal or hexagonal ring (pyridine-type nitrogen). The only molecule, between our models, that has pyridine nitrogen is molecule N012 and it turned to have a very small isotropic hfcc, equal to 0.22 MHz. Regarding the molecules with graphite-like nitrogen, their isotropic hfccs depend on the molecular size. We found values between 7 and 9 MHz for the smaller molecules (N01, N03 and N04) and very low values of about 1 MHz or lower for the larger ones (N05, N07, N08, N09, N10 and N11). The triplet-state molecule N07 showed a_{iso} value of 1.58 MHz, similar to the other molecules with same dimension. For molecules N08 and N10 we found negative a_{iso}, but we could not correlate this result with any geometrical characteristic of the molecules, since they are equal to molecule N11 which has a positive coupling constant. Finally, also the position of the nitrogen atom within the molecule seems not to affect strongly a_{iso} (except for molecules N02 and N06, already described) since similar values were found when N

was on the edges, both zigzag (N01, N03, N05, N07, N08, N10) and armchair (N09), and within the molecules (N04, N11).
The computational calculations enabled us to conclude that the hyperfine coupling constant with the nitrogen atom depend heavily on the size of the molecule and not much on its shape and structure. The only exception to this is for molecules with pyridine-like nitrogen that show higher hfccs regardless to the size.

By comparing the hyperfine coupling tensor found with hyperfine spectroscopies for the N-doped sample ($a_{iso} = 8.1$ MHz) with the values in Table 4.4 obtained from the DFT calculations we found a close similarity between the N-GQDs and the smallest models, N01, N03 and N04. A possible interpretation is that the N-doped GQDs that we can observe with pulsed EPR techniques, namely those with molecular-type radicals coupled with nitrogen atoms, have a structure that is composed by about 25-30 carbon atoms, and have not pyridine-like nitrogen, otherwise we would have observed larger hfccs. That does not mean that there are no molecules with pyridine-like nitrogen; they were indeed observed with XPS [25], but likely they are EPR-inactive or their signal has very low intensity.
If assuming round shape, 25-30 carbon atoms correspond to a GQD of size that is about 0.7 - 1.0 nm. STM gave a larger size distribution, centered at 2.0 nm. This difference between the dimension determined by STM and those that we found with pulsed EPR measurement could be explained by invoking the presence of molecules with different dimensions. The pulsed EPR signal is very low with respect to the signal that we observed with cw-EPR; in fact, we did not observe the molecular-like radicals in the cw-spectra. This is an indication that only a small fraction of molecule in the sample has undergone doping in such a way to give rise to a pulse EPR signal.
In other words, in the cw spectrum we observe all quantum dots, regardless of whether they have reacted because of the doping with nitrogen atoms. The majority of these probably is not doped and has dimension of about 2 nm. The doping caused the molecules to break in smaller portion of about 0.7 - 1.0 nm, but this happened only for few of them. Those few are responsible for the pulsed EPR signal.

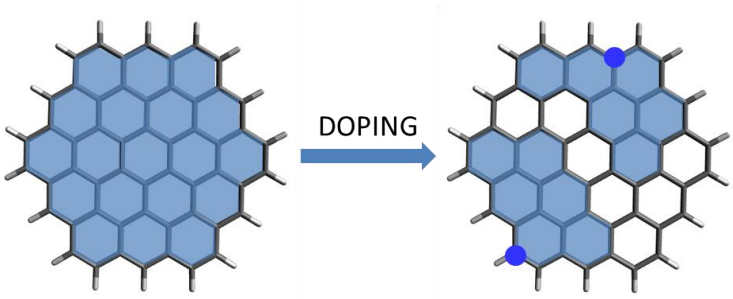

Figure 4.7 Pictorial representation of a GQD. After the doping with nitrogen atoms (blue cirlces) the π-conjugated regions (light blue) do not correspond to the whole molecule, but are extended to 20 - 25 atoms.

Another possibility to explain the discordance of results between STM and EPR is that the doping in the GQDs does not break the molecules, but can modify the extent of the delocalization, resulting in small conjugated portions of about 25 - 30 atoms (see Fig. 4.7). Thus, all the molecules have the same size of about 2 nm, but the π-conjugated system is not extended over the whole molecules, but only in portions that have smaller dimension.

4.5 - Conclusions

In this chapter we have reported a full EPR characterization of defect states in undoped and doped graphene quantum dots. Such a characterization was lacking for this kind of systems and could help in understanding their electronic and magnetic properties. By a careful analysis of the cw spectra we found for both samples signals that are characteristic of delocalized non-interacting electrons showing a Curie-like behavior with the temperature. At low temperature, the N-doped samples showed also a very narrow signal, typical of localized electrons, that was not observed in the undoped sample. That indicates an higher concentration of defect states in the doped sample that are generated by the presence of the heteroatoms in the graphene lattice.

Pulsed EPR measurements enabled us to characterize the molecular-like radicals, that are present in both samples at low concentration by filtering away the signals due to the fast relaxing species that dominate the cw spectra. With hyperfine spectroscopies we observed directly signals due to the nitrogen atoms in the doped sample and could extract the hyperfine coupling tensor of these species.

The comparison of the experimental tensor with the results from DFT calculation on some selected molecules gave us clear indication on the nature of the nitrogen signals that we observed and on the geometries of the doped GQDs. The EPR signals that we observed in the pulsed spectra are relative to electrons coupled with pyrrole and graphite nitrogens and these electrons are delocalized in a π-system extended on about 25-30 carbon atoms.

References

[1] L Gong, IA Kinloch, RJ Young, I Riaz, R Jalil, KS Novoselov. Interfacial stress transfer in a graphene monolayer nanocomposite, Adv Mater. 22 (2010) 2694-2697.

[2] V Singh, D Joung, L Zhai, S Das, SI Khondaker, S Seal. Graphene based materials: past, present and future, Progress in materials science. 56 (2011) 1178-1271.

[3] S Stankovich, DA Dikin, GH Dommett, KM Kohlhaas, EJ Zimney, EA Stach, et al. Graphene-based composite materials, Nature. 442 (2006) 282-286.

[4] S Stankovich, DA Dikin, RD Piner, KA Kohlhaas, A Kleinhammes, Y Jia, et al. Synthesis of graphene-based nanosheets via chemical reduction of exfoliated graphite oxide, Carbon. 45 (2007) 1558-1565.

[5] S Agnoli, G Granozzi. Second generation graphene: Opportunities and challenges for surface science, Surf.Sci. 609 (2013) 1-5.

[6] MJ McAllister, J Li, DH Adamson, HC Schniepp, AA Abdala, J Liu, et al. Single sheet functionalized graphene by oxidation and thermal expansion of graphite, Chemistry of Materials. 19 (2007) 4396-4404.

[7] T Ramanathan, A Abdala, S Stankovich, D Dikin, M Herrera-Alonso, R Piner, et al. Functionalized graphene sheets for polymer nanocomposites, Nature nanotechnology. 3 (2008) 327-331.

[8] HC Schniepp, J Li, MJ McAllister, H Sai, M Herrera-Alonso, DH Adamson, et al. Functionalized single graphene sheets derived from splitting graphite oxide, The Journal of Physical Chemistry B. 110 (2006) 8535-8539.

[9] H Wang, T Maiyalagan, X Wang. Review on recent progress in nitrogen-doped graphene: synthesis, characterization, and its potential applications, Acs Catalysis. 2 (2012) 781-794.

[10] X Wang, X Li, L Zhang, Y Yoon, PK Weber, H Wang, et al. N-doping of graphene through electrothermal reactions with ammonia, Science. 324 (2009) 768-771.

[11] Y Shao, S Zhang, MH Engelhard, G Li, G Shao, Y Wang, et al. Nitrogen-doped graphene and its electrochemical applications, Journal of Materials Chemistry. 20 (2010) 7491-7496.

[12] D Usachov, O Vilkov, A Gruneis, D Haberer, A Fedorov, V Adamchuk, et al. Nitrogen-doped graphene: efficient growth, structure, and electronic properties, Nano letters. 11 (2011) 5401-5407.

[13] L Qu, Y Liu, J Baek, L Dai. Nitrogen-doped graphene as efficient metal-free electrocatalyst for oxygen reduction in fuel cells, ACS nano. 4 (2010) 1321-1326.

[14] Z Jin, J Yao, C Kittrell, JM Tour. Large-scale growth and characterizations of nitrogen-doped monolayer graphene sheets, Acs Nano. 5 (2011) 4112-4117.

[15] Z Sun, Z Yan, J Yao, E Beitler, Y Zhu, JM Tour. Growth of graphene from solid carbon sources, Nature. 468 (2010) 549-552.

[16] D Deng, X Pan, L Yu, Y Cui, Y Jiang, J Qi, et al. Toward N-doped graphene via solvothermal synthesis, Chemistry of Materials. 23 (2011) 1188-1193.

[17] Z Sheng, L Shao, J Chen, W Bao, F Wang, X Xia. Catalyst-free synthesis of nitrogen-doped graphene via thermal annealing graphite oxide with melamine and its excellent electrocatalysis, ACS nano. 5 (2011) 4350-4358.

[18] JP Paraknowitsch, A Thomas. Doping carbons beyond nitrogen: an overview of advanced heteroatom doped carbons with boron, sulphur and phosphorus for energy applications, Energy & Environmental Science. 6 (2013) 2839-2855.

[19] Y Xue, D Yu, L Dai, R Wang, D Li, A Roy, et al. Three-dimensional B, N-doped graphene foam as a metal-free catalyst for oxygen reduction reaction, Physical Chemistry Chemical Physics. 15 (2013) 12220-12226.

[20] S Wang, L Zhang, Z Xia, A Roy, DW Chang, J Baek, et al. BCN graphene as efficient metal-free electrocatalyst for the oxygen reduction reaction, Angewandte Chemie International Edition. 51 (2012) 4209-4212.

[21] J Liang, Y Jiao, M Jaroniec, SZ Qiao. Sulfur and nitrogen dual-doped mesoporous graphene electrocatalyst for oxygen reduction with synergistically enhanced performance, Angewandte Chemie International Edition. 51 (2012) 11496-11500.

[22] CH Choi, MW Chung, HC Kwon, SH Park, SI Woo. B, N-and P, N-doped graphene as highly active catalysts for oxygen reduction reactions in acidic media, Journal of Materials Chemistry A. 1 (2013) 3694-3699.

[23] SN Baker, GA Baker. Luminescent carbon nanodots: emergent nanolights, Angewandte Chemie International Edition. 49 (2010) 6726-6744.

[24] M Favaro, S Agnoli, M Cattelan, A Moretto, C Durante, S Leonardi, et al. Shaping graphene oxide by electrochemistry: From foams to self-assembled molecular materials, Carbon. 77 (2014) 405-415.

[25] M Favaro, L Ferrighi, G Fazio, L Colazzo, C Di Valentin, C Durante, et al. Single and Multiple Doping in Graphene Quantum Dots: Unraveling the Origin of Selectivity in the Oxygen Reduction Reaction, ACS Catalysis. 5 (2014) 129-144.

[26] WS Hummers Jr, RE Offeman. Preparation of graphitic oxide, J.Am.Chem.Soc. 80 (1958) 1339-1339.

[27] DC Marcano, DV Kosynkin, JM Berlin, A Sinitskii, Z Sun, A Slesarev, et al. Improved synthesis of graphene oxide, ACS nano. 4 (2010) 4806-4814.

[28] A Schweiger, G Jeschke, Principles of pulse electron paramagnetic resonance, Oxford, UK, 2001.

[29] M Kaupp, M Bühl, VG Malkin, Calculation of NMR and EPR parameters: theory and applications, John Wiley & Sons 2006.

[30] MJ Frisch, GW Trucks, HB Schlegel, GE Scuseria, MA Robb, JR Cheeseman, et al., Gaussian 09, revision E. 01, Gaussian Inc., Wallingford, CT. (2010).

[31] NW Ashcroft, ND Mermin, Solid State Physics, Saunders College, Philadelphia, 1976.

[32] M Brustolon, AL Maniero, S Jovine, U Segre. ENDOR and ESEEM study of the radical obtained by γ irradiation of a single crystal of ammonium tartrate, Research on chemical intermediates. 22 (1996) 359-368.

[33] KA Ritter, JW Lyding. The influence of edge structure on the electronic properties of graphene quantum dots and nanoribbons, Nature materials. 8 (2009) 235-242.

[34] L Lai, JR Potts, D Zhan, L Wang, CK Poh, C Tang, et al. Exploration of the active center structure of nitrogen-doped graphene-based catalysts for oxygen reduction reaction, Energy & Environmental Science. 5 (2012) 7936-7942.

[35] T Sharifi, G Hu, X Jia, T Wågberg. Formation of active sites for oxygen reduction reactions by transformation of nitrogen functionalities in nitrogen-doped carbon nanotubes, ACS nano. 6 (2012) 8904-8912.

[36] Z Sheng, L Shao, J Chen, W Bao, F Wang, X Xia. Catalyst-free synthesis of nitrogen-doped graphene via thermal annealing graphite oxide with melamine and its excellent electrocatalysis, ACS nano. 5 (2011) 4350-4358.

[37] G Wagoner. Spin resonance of charge carriers in graphite, Physical Review. 118 (1960) 647.

[38] L Ćirić, A Sienkiewicz, B Nafradi, M Mionić, A Magrez, L Forro. Towards electron spin resonance of mechanically exfoliated graphene, physica status solidi (b). 246 (2009) 2558-2561.

[39] A Barbon, M Brustolon. An EPR Study on Nanographites, Applied Magnetic Resonance. 42 (2012) 197-210.

[40] S Rao, A Stesmans, D Kosynkin, A Higginbotham, J Tour. Paramagnetic centers in graphene nanoribbons prepared from longitudinal unzipping of carbon nanotubes, New Journal of Physics. 13 (2011) 113004.

[41] BS Paratala, BD Jacobson, S Kanakia, LD Francis, B Sitharaman. Physicochemical characterization, and relaxometry studies of micro-graphite oxide, graphene nanoplatelets, and nanoribbons, PLoS One. 7 (2012) e38185.

[42] M Tommasini, C Castiglioni, G Zerbi, A Barbon, M Brustolon. A joint Raman and EPR spectroscopic study on ball-milled nanographites, Chemical Physics Letters. 516 (2011) 220-224.

[43] F Tampieri, S Silvestrini, R Riccò, M Maggini, A Barbon. A comparative electron paramagnetic resonance study of expanded graphites and graphene, Journal of Materials Chemistry C. 2 (2014) 8105-8112.

[44] K Tadyszak, MA Augustyniak-Jabłokow, AB Więckowski, L Najder-Kozdrowska, R Strzelczyk, B Andrzejewski. Origin of electron paramagnetic resonance signal in anthracite, Carbon. 94 (2015) 53-59.

[45] D Huber, R Urbano, M Sercheli, C Rettori. Fluctuating field model for conduction electron spin resonance in graphite, Physical Review B. 70 (2004) 125417.

[46] MA Augustyniak-Jabłokow, K Tadyszak, M Maćkowiak, S Lijewski. ESR study of spin relaxation in graphene, Chemical Physics Letters. (2012).

CHAPTER 5 - THEORETICAL CALCULATION OF EPR PARAMETERS: STUDY OF THE GEOMETRIC EFFECTS ON THE g-TENSOR OF EXTENDED π-SYSTEMS BY DFT

5.1 - Introdction

This chapter is devoted to the computational study of some EPR parameters by Density Functional Theory (DFT) methods. This study has been carried out because some experimental spectra of carbon-based materials show very low **g**-tensor values (sometimes lower than 2.000 [1], see chapter 3) and some authors claim that these values are due to the non-planarity of some systems. For example, very low g-values are reported for fullerenes and nanotubes, [2,3]. This computational study is limited to small molecules (max 100 atoms).
The major aspect that is considered in particular is then the dependence of the $\boldsymbol{g}$-tensor for some selected molecules from their shape and from the effects of curvature.

5.1.1 - $\boldsymbol{g}$-tensors of carbon systems

The g-factor of organic radicals is relatively close to the free-electron value of $g_e = 2.0023$. It generally lies within the rather narrow range of 2.00 to 2.01 in the absence of atoms heavier than chlorine. Deviations of g from g_e are due an admixture between the magnetic orbital and the spin moments. Such an admixture is brought about by spin-orbit coupling, which is particularly effective in heavy atoms. Thus, within the narrow range of 2.00 to 2.01 the majority of deviations from 2.0023 occur when the radical contains heteroatoms.
Alkyl radicals have a g-factor 2.0026 [4], whereas hydrocarbon π radicals have a g-factor between 2.0025 and 2.0028: typically, for the radical cations of anthracene, tetracene, pentacene, and perylene, this factor is close to 2.00257, and for the corresponding radical anions, it is about 2.00267 [4]. The anions thus exhibit a larger g-factor than the cations. The g-factor of neutral π radicals lies in between. Exceptions are π radicals with a degenerate ground state, such as the radical anions of benzene and coronene, for which the g-factor is somewhat higher, namely 2.00284 and 2.00305, respectively [4].
The anisotropy of the $\boldsymbol{g}$ -tensor is usually very small for hydrocarbon radicals. For example, the principal values g_Z, g_Y, and g_X of the $\boldsymbol{g}$-tensor for the ethyl radical are 2.0016, 2.0031, and 2.0031, respectively, and the isotropic g-value is 2.0026 [4]. The z direction is the axis of the $2p$-orbital of the methylene atom bearing the spin, and x and y are perpendicular to it. Therefore, g_Z can be denoted $g_{\parallel}$, and $g_{\perp} = g_X = g_Y$

for an axial $\boldsymbol{g}$-tensor. This rule remains the same for π radicals in which the z direction is parallel to the p_z axes of the π system, and x and y lie in the molecular plane perpendicular to these axes. The g_Z component is generally the lowest one, being closest to the free-electron value g_e, so that $\Delta g = g_{\parallel} - g_{\perp}$ is negative. For π radicals of hydrocarbon, $|\Delta g|$ is usually smaller than 0.001, and its effect on the spectrum becomes evident only when combined with that of hyperfine anisotropy.

Regarding carbon-based materials, the $\boldsymbol{g}$-tensors are quite different from case to case, anyway, in most cases their values are similar to those observed for organic radicals.
Diamonds and nanodiamonds have EPR signals due to sp^3 dangling bonds or vacancies. Isotropic $\boldsymbol{g}$-tensors are reported for these system, with values very near to g_e: 2.0023-2.0025 [5-7].
For extended π molecules or materials, the spin orbit coupling is more effective and deviation from the g_e value can be more pronounced.
Whether for graphene the anisotropy of the tensor is small and the $\boldsymbol{g}$-tensor has principal values similar to the free electron [8], the $\boldsymbol{g}$-tensor of graphite is rather anisotropic with a strong deviation from the g_e value of the $g_{\parallel}$ component because of a strong spin-orbit interaction along the direction perpendicular to the graphite basal plane [8]. $g_{\parallel}$ is strongly temperature-dependent because of the contribution of orbital angular momentum in the electronic states of spins giving rise to the resonance. Typical values for a single crystal go from 2.05 at room temperature, up to 2.1 at low temperature. By reducing the dimensions of the particles, lower values with respect of the bulk graphite are found. For nanographites with size of about 100-200 nm values between 2.015 and 2.030 have been reported [9]. $g_{\perp}$ is generally similar to g_e and doesn't vary with temperature.

For carbon nanotubes an anisotropy of the $\boldsymbol{g}$-tensor, similar to graphite, has been observed. For multi-walled carbon nanotubes Likodimos and coworkers [10] report an average g-factor of about 2.013 at room temperature, that gets lower upon cooling. Dinse and cokorkers [11] studied a sample of single-walled nanotubes and observed two resonances centered with $g = 2.07$ and 2.00 of comparable amplitude at room temperature. By lowering the temperature, the lower field component disappears and the intensity of the other grows. Thess at al. [3] for a sample of metallic single-walled carbon nanotubes found a quite low g-value of about 2.001.
Among the carbon systems, fullerene is probably the one with the most strange $\boldsymbol{g}$-tensor. Allemand et al. [12] measured the solid-state electron spin resonance signal at 300 K and found a symmetric line with $g = 1.9991$, to be contrasted with the typical, free-electron value of 2.0023. This very low value is usually observed in transition metal and rare earth compounds and could be due to a large spin-orbit coupling resulting from the electronic structure of the fullerene.

For amorphous carbon the $\boldsymbol{g}$-tensor can vary according to the effective nature of the material, but generally it is almost isotropic with value between 2.003 and 2.004 [13-16].

5.1.2 - $\boldsymbol{g}$-tensor calculation with DFT methods

The $\boldsymbol{g}$-tensor elements can be obtained by computational methods. Several approaches have been presented for the calculations of tensors that can be applied to a wide variety of species. Many of these approaches are based on DFT [17-22]. The theory for the calculation of EPR g-tensors with DFT has been well described by Patchkovskii and Schreckenbach in [18]; here we report only some basic concepts.

Any theoretical treatment on the $\boldsymbol{g}$-tensor uses a microscopic Hamiltonian operator to determine the separation between the two spin states induced by the magnetic field. The simplest Hamiltonian operator of such type, that neglects relativistic effects, is composed by monoelectronic operators that describe the Zeeman interaction of the spin magnetic moment ($\widehat{\mathcal{H}}_Z$), of the orbital magnetic moment ($\widehat{\mathcal{H}}_L$) and the nuclear spin-orbit coupling ($\widehat{\mathcal{H}}_{SO(N)}$)

$$\widehat{\mathcal{H}}_Z = \sum_j \hat{h}_Z^j = \sum_j \frac{g_e}{2c} \boldsymbol{B} \cdot \hat{\boldsymbol{s}}_j \tag{5.1}$$

$$\widehat{\mathcal{H}}_L = \sum_j \hat{h}_L^j = \sum_j \frac{1}{2c} \boldsymbol{B} \cdot \left(\boldsymbol{r}_j \times \widehat{\boldsymbol{p}}_j\right) \tag{5.2}$$

$$\widehat{\mathcal{H}}_{SO(N)} = \sum_j \hat{h}_{SO}^j = \sum_j \frac{g'}{4c^2} \sum_A Z_A \, \hat{\boldsymbol{s}}_j \cdot \frac{\left(\boldsymbol{r}_j - \boldsymbol{R}_A\right) \times \widehat{\boldsymbol{p}}_j}{\left|\boldsymbol{r}_j - \boldsymbol{R}_A\right|^3} \tag{5.3}$$

the summations are relative to each electron j and each nucleus A; $\boldsymbol{r}_j$ and $\widehat{\boldsymbol{p}}_j$ are the position and the linear momentum operators of the j-th electron and $\boldsymbol{R}_A$ and Z_A are the position and charge of the A-th nucleus. $g' = 2g_e - 2$. Calculations that require a good agreement with the experimental data should take into account also for other operators: the two-electron spin-orbit operator ($\widehat{\mathcal{H}}_{SO(2e)}$), the spin-other orbit operator ($\widehat{\mathcal{H}}_{SOO}$), the spin Zeeman kinetic energy correction ($\widehat{\mathcal{H}}_{ZKE}$) and the diamagnetic contributions that enable to obtain gauge-invariant results (nuclear spin-orbit $\widehat{\mathcal{H}}_{SO(N)}^{dia}$, two-electron spin-orbit $\widehat{\mathcal{H}}_{SO(2e)}^{dia}$ and spin-other orbit $\widehat{\mathcal{H}}_{SOO}^{dia}$)

$$\widehat{\mathcal{H}}_{SO(2e)} = \sum_j \sum_{k \neq j} -\frac{g'}{4c^2} \hat{\boldsymbol{s}}_j \cdot \frac{\left(\boldsymbol{r}_j - \boldsymbol{r}_k\right) \times \widehat{\boldsymbol{p}}_j}{\left|\boldsymbol{r}_j - \boldsymbol{r}_k\right|^3} \tag{5.4}$$

$$\widehat{\mathcal{H}}_{SOO} = \sum_j \sum_{k \neq j} -\frac{1}{c^2} \hat{\boldsymbol{s}}_j \cdot \frac{\left(\boldsymbol{r}_k - \boldsymbol{r}_j\right) \times \widehat{\boldsymbol{p}}_k}{\left|\boldsymbol{r}_k - \boldsymbol{r}_j\right|^3} \tag{5.5}$$

$$\widehat{\mathcal{H}}_{ZKE} = \sum_j -\frac{g_e}{4c^2} \hat{p}_j^2 \boldsymbol{B} \cdot \hat{\boldsymbol{s}}_j \tag{5.6}$$

In a Kohn-Sham formulation the total energy can be written as

$$E^{KS} = \sum_i \langle \psi_i | \hat{f} | \psi_i \rangle - \frac{1}{2} \int v_{ee}(\boldsymbol{r}) \rho(\boldsymbol{r}) d\boldsymbol{r} - \int v_{xc}(\boldsymbol{r}) \rho(\boldsymbol{r}) d\boldsymbol{r} + E_{xc} \qquad (5.7)$$

$\hat{f}$ is the Kohn-Sham-Fock operator and contains the main terms for the calculation of the $\boldsymbol{g}$-tensor:

$$\hat{f} = \hat{T} + v_{ext} + v_{ee} + v_{xc} + \hat{h}_Z + \hat{h}_L + \hat{h}_{SO} + \hat{h}_{SO}^{dia} \qquad (5.8)$$

$\hat{T}$ is the kinetic energy operator, v_{xc} is the exchange and correlation potential (XC), v_{ext} and v_{ee} are respectively the external potential and the interelectronic interaction potential, $\hat{h}_{SO}^{dia}$ is a diamagnetic correction to the spin-orbit interaction operator.
Because of the small energies that are involved in the EPR transitions, the field-dependent terms can be treated as perturbations in the calculation of the total energy of the system. The approach to treat the spin-orbit interaction is less clear, for light nuclei a perturbation theory is still available but not for heavy nuclei. Two distinct and complementary methods for the $\boldsymbol{g}$-tensor calculation have been developed to overcome these complications:

- In the two-component approach the spin-orbit coupling is treated by using the variational theory and the $\boldsymbol{g}$-tensor is calculated as first derivative of the energy. This method can be applied to radicals that have an arbitrarily large deviation of the $\boldsymbol{g}$-tensor from g_e but doesn't work with systems that have arbitrary multiplicity and doesn't treat correctly the spin polarization.
- In the one-component approach both the field dependent terms and the spin-orbit interaction can be treated as perturbations; that enables to obtain second-order expressions for the $\boldsymbol{g}$-tensor. This method can be applied to radicals with any multiplicity and has some terms that take into account for the spin polarization. The drawback is the applicability limited only to radicals with small deviations of the $\boldsymbol{g}$-tensor.

The analysis of the $\boldsymbol{g}$-tensors obtained with DFT show a good agreement with the experimental ones. The values depend poorly by the choice of the basis set and of the XC functionals mostly for light atoms. For systems with transition metals the dependence of the results from the functionals is more evident and it's typical of each system; in general better results are obtained if hybrid potentials are used instead of LDA or GGA approaches.

5.2 - Models

All calculations have been carried out on isolated molecules with a limited number of carbon atoms (less than 100 atoms) in order to avoid too high computational costs. All molecules are pure conjugated hydrocarbons.
The first class of molecules that we studied is composed by neutral Poly Aromatic Hydrocarbons (PAH) with an unpaired electron in a non-bonding molecular orbital. We examined molecules with only zig-zag edges, since is known from many experimental and theoretical studies that the unpaired electrons are localized mostly in these kind of edges with respect to the armchair edges [23,24]. The molecules are represented in Scheme 5.1.

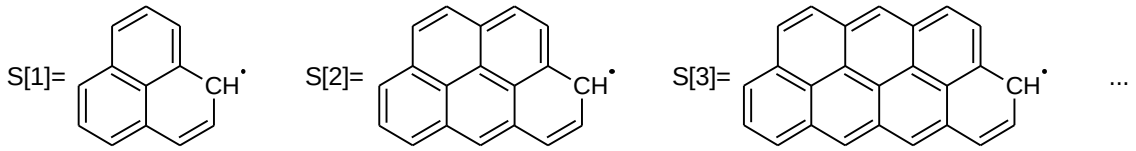

Scheme 5.1

We labelled these radicals as $S[k]$ where k is the number of hexagonal rings in the upper part. We studied planar $S[k]$ with k going from 1 to 9 and $S[14]$. The shortest radical $S[1]$ is the phenalenyl radical that has been extensively studied recently both by an experimental and a theoretical point of view [4,25-27]. Some experimental work can be find also for $S[2]$ that is more commonly called benzo[cd]pyrenyl or olympicenyl. For $k > 2$ no experimental work has been done [28].
For these radicals we studied also the effect of the curvature on the $\boldsymbol{g}$-tensor. To obtain a bent structure we attached a methylene bridge to both ends of the molecule and optimized the geometry (Scheme 5.2).

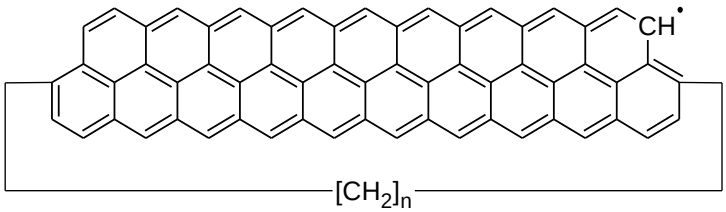

Scheme 5.2

By varying the number of methylenes it's possible to tune the curvature. These bent structures are labelled $S[k]\_b[CH_2]_n$ or $S[k]\_[CH_2]_n$ where n is the number of methylene in the bridge. The presence or absence of the letter b in the label indicates if the bridge has been kept or removed after the optimization of the geometry and

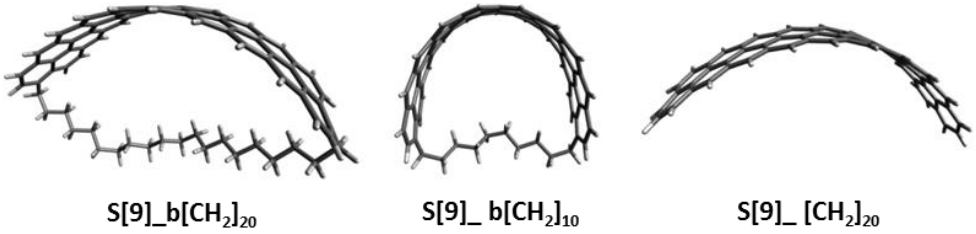

Figure 5.1 Chemical structure of some of the bent stripes that have been studied in this work. The difference between the first and the second molecules is the length of the methylene bridge. The third molecule come from the first but the bridge has been removed without further optimizations.

prior to the calculation of EPR parameters. Some exempla of bent structure are reported in Figure 5.1.

The second type of radicals that we studied are the radical ions of coronene and corannulene. These were chosen in order to have a different type of curvature with respect of the ribbons. In fact, corannulene is a bent molecule and its curvature is due to the presence of a central pentagonal ring instead of the hexagonal one that is in the planar coronene. Pentagonal rings in graphene-like structure can be formed after rearrangement of some $C-C$ bonds that are associated to some types of defects like Stone-Wall defects or carbon vacancies. The presence of pentagonal rings in experimental graphene samples has been observed with TEM [29] and its tendency to cause the bending of the plane is known. Therefore, we studied first coronene and corannulene (Scheme 5.3)

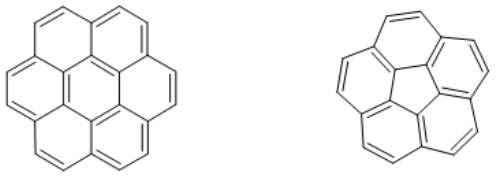

Scheme 5.3

Then we examined molecules with increasing number of pentagonal rings. To do so we started with corannulene and added carbon atoms in 5-membered rings. We kept the pattern of pentagonal and hexagonal rings that are in fullerene (each pentagonal ring surrounded by 5 hexagonal rings, each hexagonal ring surrounded by 3 pentagonal and 3 hexagonal rings). Doing so we have molecules with increasing curvature. The most curved molecule is fullerene with 12 pentagonal rings. The molecules are labelled with their molecular formula and the number of pentagonal rings. All carbon atoms are in a sp^2 configuration (Fig. 5.2).

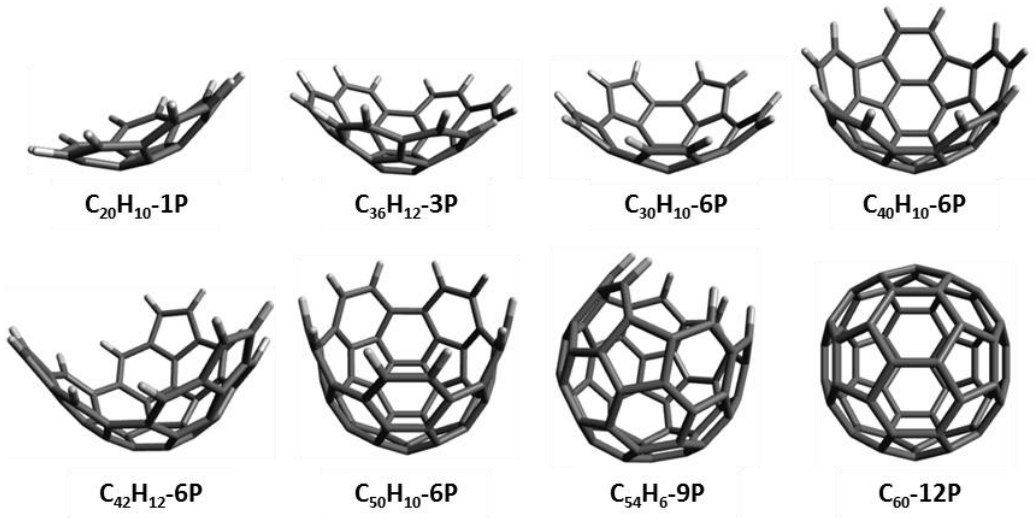

Figure 5.2 Chemical structures of the fullerene fragments that have been studied. Their curvature depends on the presence of pentagonal rings.

5.3 - Experimentals

All calculations have been carried out on isolated molecules based on DFT considering the widely adopted B3LYP hybrid functional, which is known to provide reliable equilibrium molecular structures [18]. All the equilibrium molecular geometries reported in our work have been obtained with *Gaussian09* [30] with the B3LYP/6-311G(d,p) method. We have calculated the vibrational frequency for all the optimized structures in order to assess that they were actually energy minima. When imaginary frequencies were obtained from the Hessian evaluation, we displaced the structure along the normal mode associated with the negative eigenvalue and carefully and repeatedly re-optimized the structure until no negative eigenvalues were observed anymore. Coronene and corannulene have degenerate HOMOs and LUMOs, so that pairs of Jahn-Teller (JT) distorted structures are expected in their mono-ions. For each cation (anion) we optimized the geometry of one JT form by removing (adding) one electron from (to) one of the degenerate HOMO (LUMO) orbitals. The second JT form was obtained by selecting the other degenerate HOMO (LUMO) orbital in building the electronic structure of the cation (anion). In this way, by also carefully controlling the geometry optimization process (see above), we obtained for each ion two different JT structures, corresponding to two different minima. This procedure was not used for the optimization of the fullerene fragments even if JT distortion is expected for their ions too. The reason for this choice will be explained later.
All EPR-related calculations were carried out (on the structures determined above) by means of the Gaussian09 and the ORCA quantum chemistry package [31] with the B3LYP functional and the EPR-II basis set [32].

Table 5.1 Computed $\boldsymbol{g}$-tensor principal values for planar $S[k]$ radicals. For radical $S[1]$ the experimental value is reported.

Radical	$\boldsymbol{g_X}$	$\boldsymbol{g_Y}$	$\boldsymbol{g_Z}$	$< g >$
$S[1]$	2.00275 2.00278[exp]	2.00275 2.00278[exp]	2.00230 2.00226[exp]	2.00260 2.00261[exp]
$S[2]$	2.00277	2.00276	2.00233	2.00262
$S[3]$	2.00281	2.00276	2.00236	2.00264
$S[4]$	2.00285	2.00275	2.00238	2.00266
$S[5]$	2.00287	2.00276	2.00240	2.00268
$S[6]$	2.00287	2.00277	2.00243	2.00269
$S[7]$	2.00287	2.00278	2.00247	2.00271
$S[8]$	2.00286	2.00279	2.00251	2.00272
$S[9]$	2.00286	2.00280	2.00254	2.00274
$S[14]$	2.00286	2.00286	2.00273	2.00282

[exp]: experimental values from [26]

5.4 - Results and discussion

5.4.1 - Ribbons

Let us consider first the neutral PAH with unpaired electrons in non-bonding molecular orbital. First, the influence of the dimension of the molecule on the $\boldsymbol{g}$-

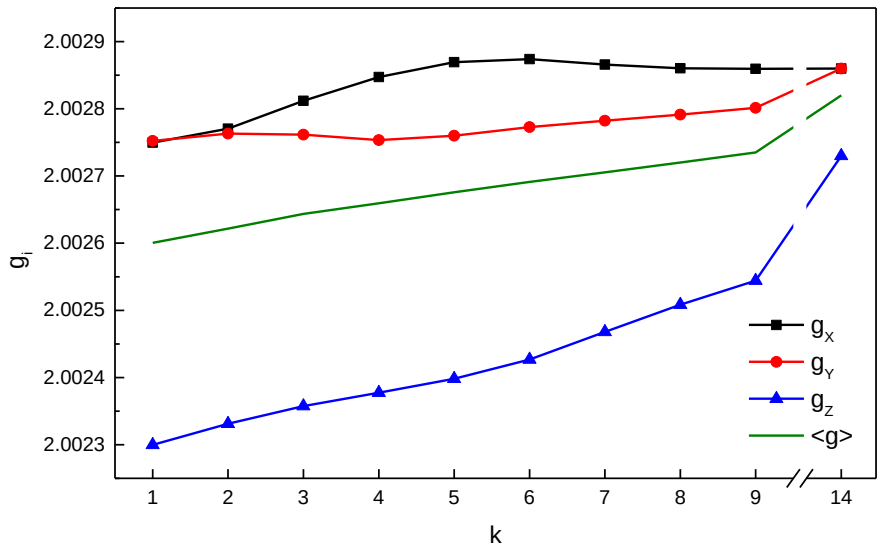

Figure 5.3 Trend of the computed $\boldsymbol{g}$-tensor principal values and average value ($< g >$) for the planar $S[k]$ radical as function of the length of the radicals.

tensors has been investigated. For this reason DFT calculation have been performed on some planar PAH varying the length of the molecules. The results are collected in Table 5.1 and in Figure 5.3. For radical $S[1]$ is reported also the experimental value, taken from [25]. We obtained an excellent reproduction of the experimental data with our calculations.

The X and Y components are equal for radical $S[1]$ since it has a higher symmetry with respect to the longer radicals. For the others the X and Y components are slightly different. The difference between them grows going from $S[2]$ to longer ribbons, reach a maximum of about 0.00011 for radical $S[5]$ and then decreases slowly. There is no significant variation of the values by increasing the length of the ribbons. Regarding the Z component, it has the value of g_e (free electron value, 2.0023) for $S[1]$, then it increases almost linearly by increasing the length of the ribbon. Also the average value of the $\boldsymbol{g}$-tensor grows almost linearly with increasing of the length. Assuming that this linear dependence between $< g >$ and k will be valid also for higher values of k, we can estimate how long the ribbon should be to have the same g-factor as pure graphene (2.0040 at 0 K [33]). From a quick calculation we found k between 70 and 100.

For some of these planar radicals we computed also the spin densities. Some exempla are reported in Figure 5.4. From that, we had a confirmation that the unpaired spins tend to be localized along the zig-zag edges of the carbon planes.

Then, using the longest radical $S[9]$ as starting point, we studied the influence of the curvature of the ribbon on the $\boldsymbol{g}$-tensor. To bend the molecule we used a methylene bridge as described in the models section. We performed some calculation varying the number of methylenes of the bridge and, consequently, the curvature. In some cases, we removed the bridge after the geometry optimization in order to check the possible influence of the bridge itself on the $\boldsymbol{g}$-tensor. The results of the calculations are collected in Table 5.2.

From a quick examination of the numbers, it is clear that the curvature, induced by the bridge, doesn't affect appreciably the $\boldsymbol{g}$-tensor of the ribbon. In fact, a marked increase of the curvature, going from a bridge composed of 20 methylenes to a bridge of 10 (see Figure 5.1 for a pictorial view of the two radicals) induces a variation in the average g values of only 0.0001 that, from an experimental point of view, is almost negligible. The comparison of the planar radical $S[9]$ ($< g >= 2.00274$) with the bent

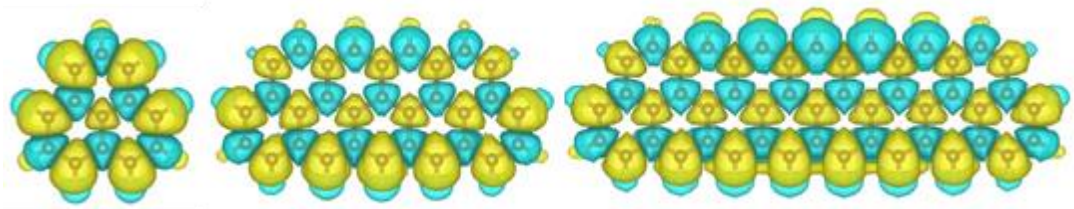

Figure 5.4 Spin density for some of the studied radical stipes. The major density is localized along the zig-zag edges

Table 5.2 Computed $\boldsymbol{g}$-tensor principal values for some bent $S[9]$ radicals.

$\boldsymbol{Radical}$	$\boldsymbol{g_X}$	$\boldsymbol{g_Y}$	$\boldsymbol{g_Z}$	$< g >$
$S[9]\_b[CH_2]_{20}$	2.00274	2.00317	2.00283	2.00291
$S[9]\_b[CH_2]_{18}$	2.00269	2.00328	2.00280	2.00292
$S[9]\_b[CH_2]_{10}$	2.00251	2.00342	2.00272	2.00288
$S[9]\_[CH_2]_{20}$	2.00267	2.00327	2.00235	2.00276
$S[9]\_[CH_2]_{10}$	2.00245	2.00249	2.00346	2.00280

one without the bridge ($S[9]\_[CH_2]_{20}$ and $S[9]\_[CH_2]_{10}$) lead to the same conclusion. The presence of the methylene bridge itself has a more evident effect on the $\boldsymbol{g}$-tensor with respect to the curvature, causing slightly higher values.
By analyzing the values of the $\boldsymbol{g}$-tensor of these molecules, we can conclude that they are not affected from the curvature induced by the methylene bridge.

5.4.2 - Coronene and corannulene

Another way to induce a curvature in a graphene sheet is to substitute some of the hexagonal rings that form the conjugated plane with pentagonal rings. In this way the structure becomes naturally distorted; fullerene, for example, is curved because of the presence of 12 pentagonal rings. This is a different type of curvature from that discussed in the previous part, caused by the methylene bridge. Therefore, we want to study the possible dependence of the $\boldsymbol{g}$-tensor from the curvature induced by the presence of pentagonal rings.
The simplest model for this kind of study is corannulene that has a pentagonal carbon ring, surrounded by five hexagonal rings and its planar counterpart, coronene. Coronene and corannulene have been extensively studied in the past, both experimentally and theoretically, so we can compare the results of our calculation with previous calculations and with experimental data.

Table 5.3 Comparison between the bond lengths of neutral coronene obtained from our calculations, from the calculations by Kato [34] and from the crystal structure [47].

Bond	Calculated ours (Å)	Calculated Kato (Å)	Crystal structure (Å)
a	1.372	1.372	1.346
b	1.424	1.424	1.415
c	1.421	1.422	1.433
d	1.428	1.428	1.425

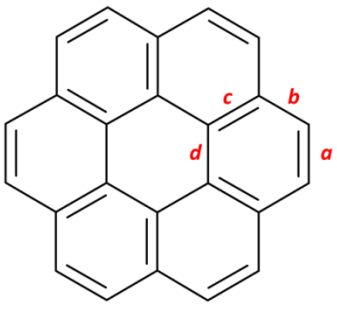

Table 5.4 Comparison between the bond lengths of neutral corannulene obtained from our calculations, from the calculations by Yamabe [38] and from the crystal structure [48].

Bond	Calculated ours (Å)	Calculated Yamabe (Å)	Crystal structure (Å)
a	1.386	1.390	1.402
b	1.446	1.448	1.440
c	1.383	1.385	1.391
d	1.416	1.417	1.413

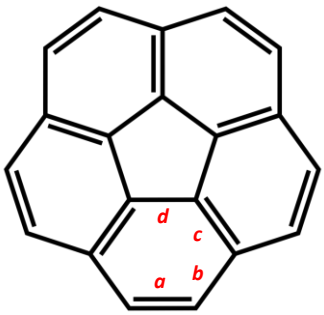

We first obtained the equilibrium geometries for neutral coronene and corannulene. The bond length are reported in Tables 5.3 and 5.4 together with the experimental crystal data [47,48] and the values obtained from previous DFT studies by Kato [34] and Yamabe [38]. Our results are very similar to those from previous calculations and also reproduce quite well the crystal data in particular the difference between different type of bonds (external bonds a and b, radial bonds c, internal bonds d, see the figures on the side of the tables)

Neutral coronene and corannulene are diamagnetic. To study their magnetic properties we need to consider their radical cations and radical anions, but in doing so, there is a significant feature that has to be taken into account. Coronene and corannulene are highly symmetric molecules (D_{6h} and C_{5v} point group) and possess degenerate HOMO and LUMO levels, thus the ions undergo Jahn-Teller (JT) distortion (Figure 5.5).

The theorem bearing this name predicts that, to lower its energy, a nonlinear molecule in a degenerate ground state will deform to species in which the symmetry is reduced and the degeneracy is removed. Such molecule is a neutral radical or a radical ion, like the benzene anion, which has an axial symmetry, i.e., a rotational axis C_n with $n \geq 3$. In general, for each radical, two or more deformed species of lower

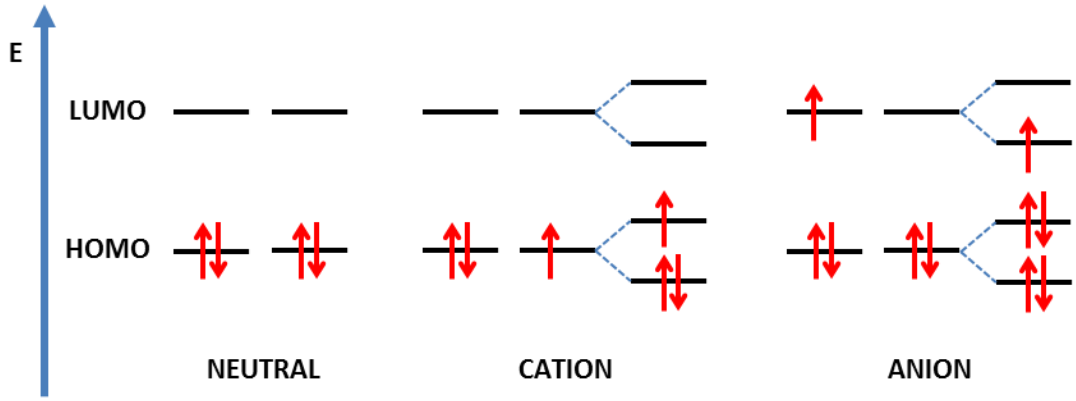

Figure 5.5 Frontier energy levels for neutral coronene and corannulene, radical cation and radical anions. For the ions, Jahn-Teller distortion lowers the overall energy.

symmetry must be considered, which differ in their geometry, symmetry, and spin distribution. This issue has been stated in the 60's for a series of highly symmetric aromatic ions, including coronene [49]. Forty years later more accurate DFT calculations showed that the inclusion of JT distortion affords excellent agreement with experiment in the vibrational frequencies of coronene and corannulene [34]. However, even if particularly careful and accurate, this studies still show the presence of a slight instability in the potential energy surface with associated imaginary wavenumber modes [34,38]. Corannulene has been also studied by Galué et al. [50], and it has been shown the importance of the JT effect with respect to coronene.

Our present investigation aims at providing fully stable energy minima of the JT distorted structures of corannulene and coronene ions. Furthermore, we investigate the effect of the JT distortion on the $\boldsymbol{g}$-tensor of both molecules in both anionic and cationic forms.

We have optimized the geometries of the JT couple for all ions; our geometries correspond to actual energy minima, no imaginary frequency was observed from the Hessian evaluation. That is an improvement of the data reported in literature [34,38]. From the geometries, we calculated the percentage variations of the bond lengths with respect to the neutral molecules. Some important considerations can be made by comparing these with the form of the frontier spin-orbitals (see Figures 5.6, 5.7, 5.8 and 5.9, upper part). Indeed, for the anions, we found that the nodes in the highest occupied spin-orbital correspond to the bonds that becomes longer (blue in the figures), that means that the extra electron introduces an antibonding contribution that is localized at the bonds that experience JT distortion toward longer equilibrium length. On the other hand, for the cations, we observed nodes in the lowest unoccupied spin-orbitals correspond to bonds that shrink (red bonds). In this case, we removed an electron from a bonding state, thus removing a bonding contribution. So the nodes are localized along the bonds that, after JT distortion, are shorter.

In the lower part of Figures 5.6-5.9 are reported the bond lengths for both JT forms for each ion and the percentage variation with respect to the neutral molecule, divided among external, radial and internal bonds.

For coronene ions the two JT forms have almost D_{2h} symmetry and their structure are significantly different from the neutral D_{6h} molecule. Regarding the anions, we can see that the internal bonds are not much affected by the distortion; their variation is of the order of 0.5 %. JT distortion affects more the radial and external bonds with variations between 1 and 2 %. We found similar results for the cations. The energy difference between the two JT forms of coronene anion is 0.0002 eV, the same difference has also been obtained for the two forms of the cation (see Table 5.5 for the energies).

The JT forms of the corannulene ions have almost C_s symmetry (actually they belong to the C_1 symmetry group), so also for them there are significant difference from the

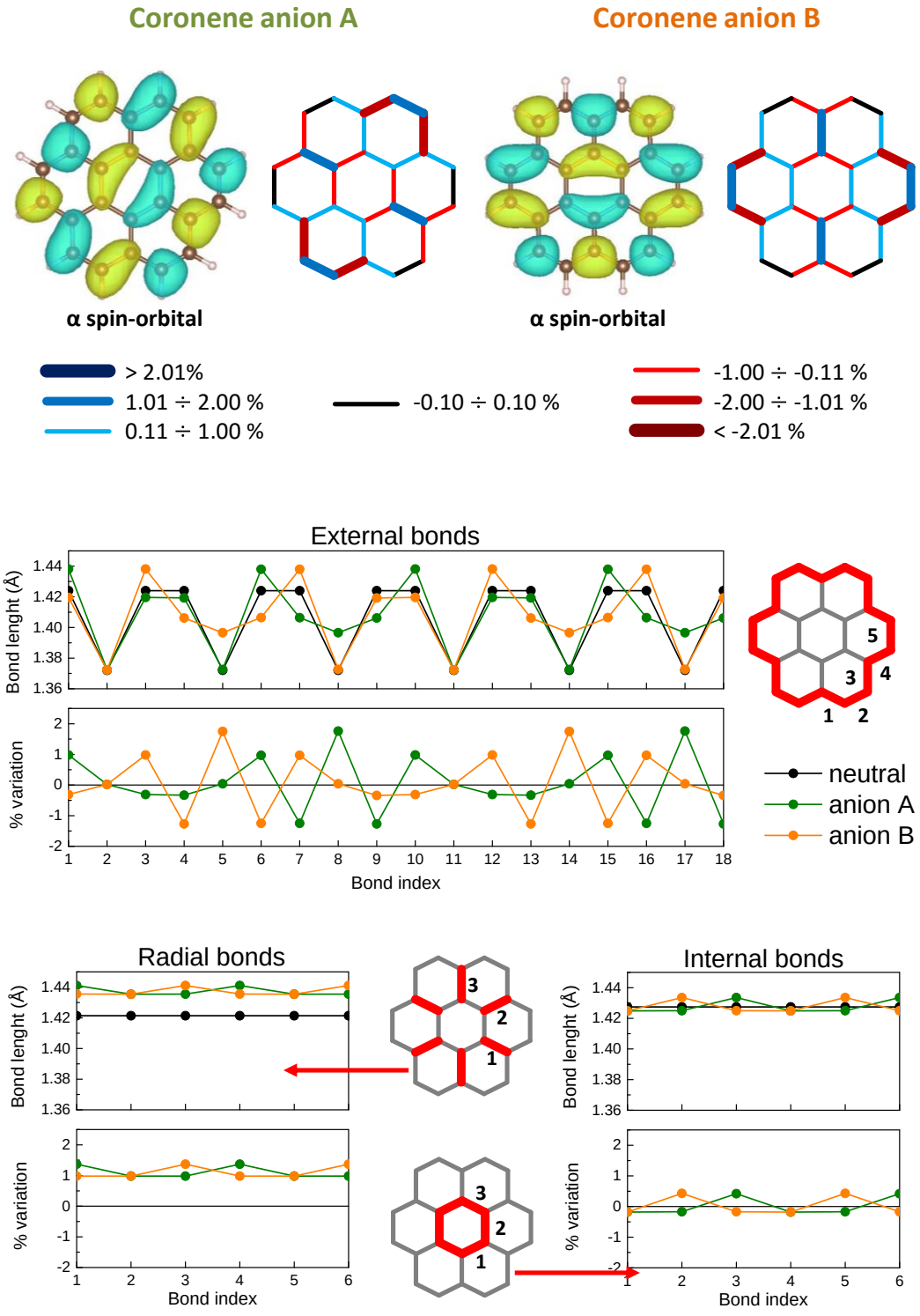

Figure 5.6 Jahn-Teller analysis of coronene anions. In the upper part is reported a comparison between the highest occupied spin-orbital and the variation of the bond length with respect to the neutral form (red bonds correspond to a shortening and blue bonds to an elongation). In the lower part is reported in a more explicit way the bond length for both the JT forms and the percentage variation with respect to the neutral. External, radial and internal bonds are reported in different graphs.

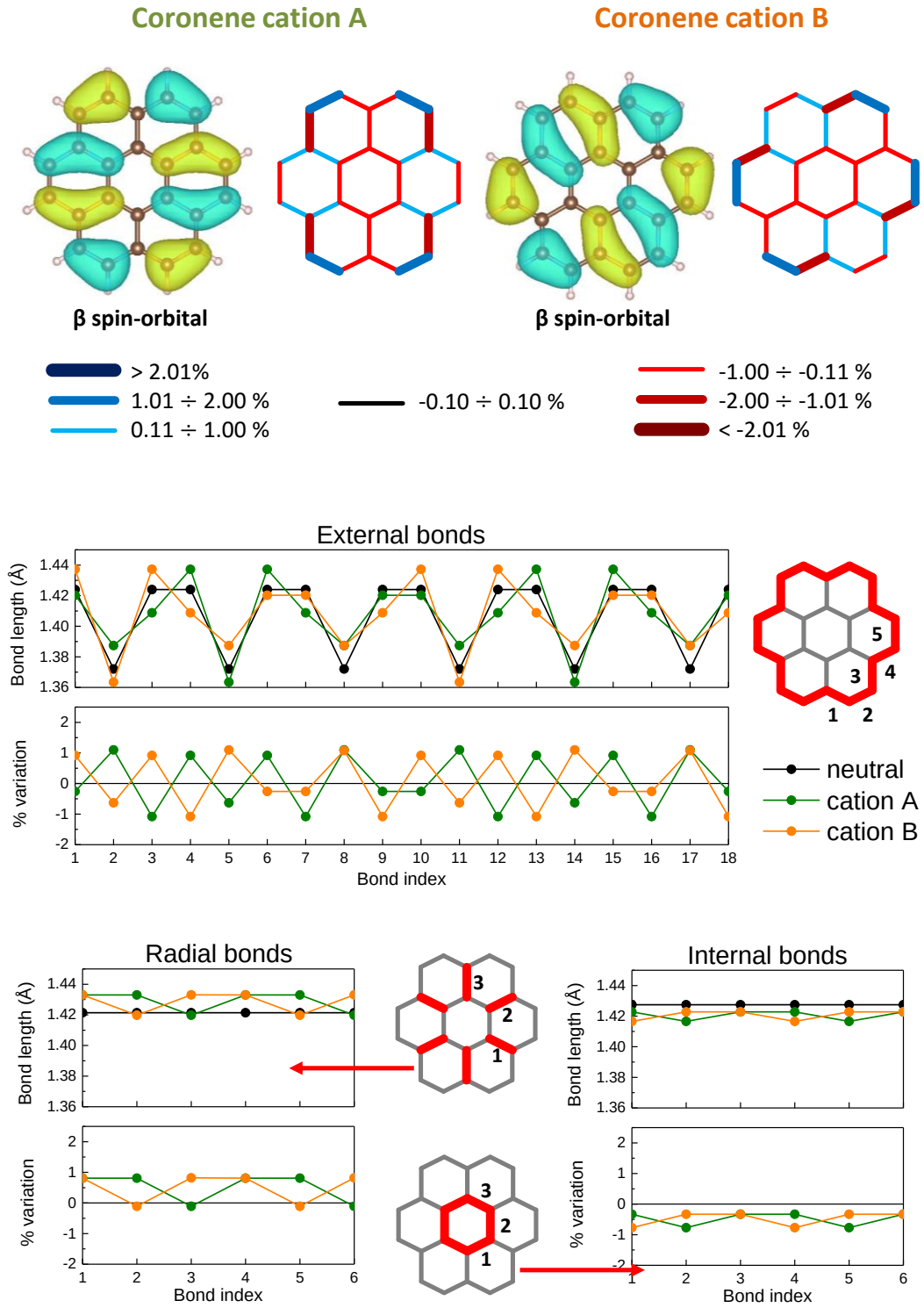

Figure 5.7 Jahn-Teller analysis of coronene cations. In the upper part is reported a comparison between the lowest unoccupied spin-orbital and the variation of the bond length with respect to the neutral form (red bonds correspond to a shortening and blue bonds to an elongation). In the lower part is reported in a more explicit way the bond length for both the JT forms and the percentage variation with respect to the neutral. External, radial and internal bonds are reported in different graphs.

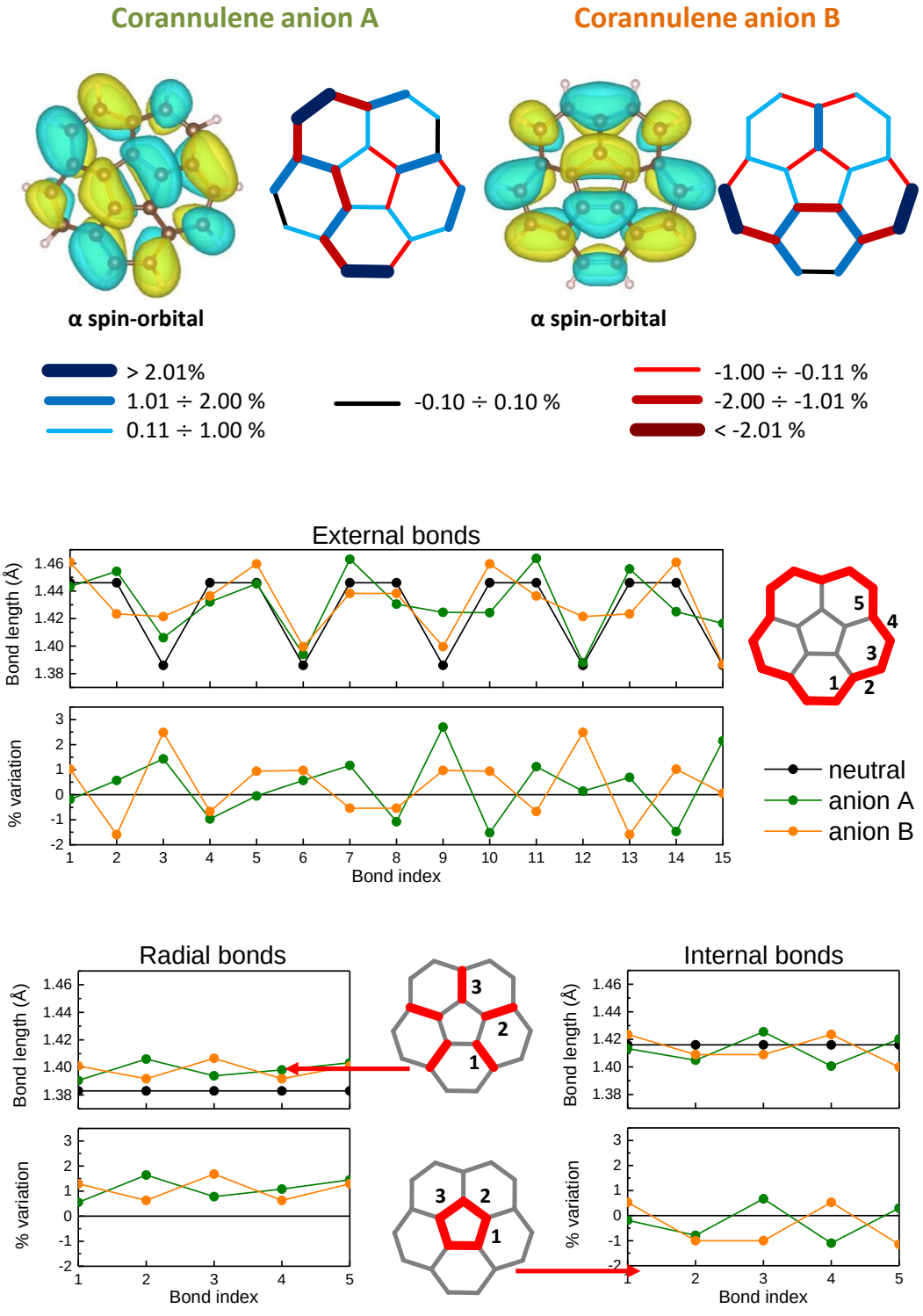

Figure 5.8 Jahn-Teller analysis of corannulene anions. In the upper part is reported a comparison between the highest occupied spin-orbital and the variation of the bond length with respect to the neutral form (red bonds correspond to a shortening and blue bonds to an elongation). In the lower part is reported in a more explicit way the bond length for both the JT forms and the percentage variation with respect to the neutral. External, radial and internal bonds are reported in different graphs.

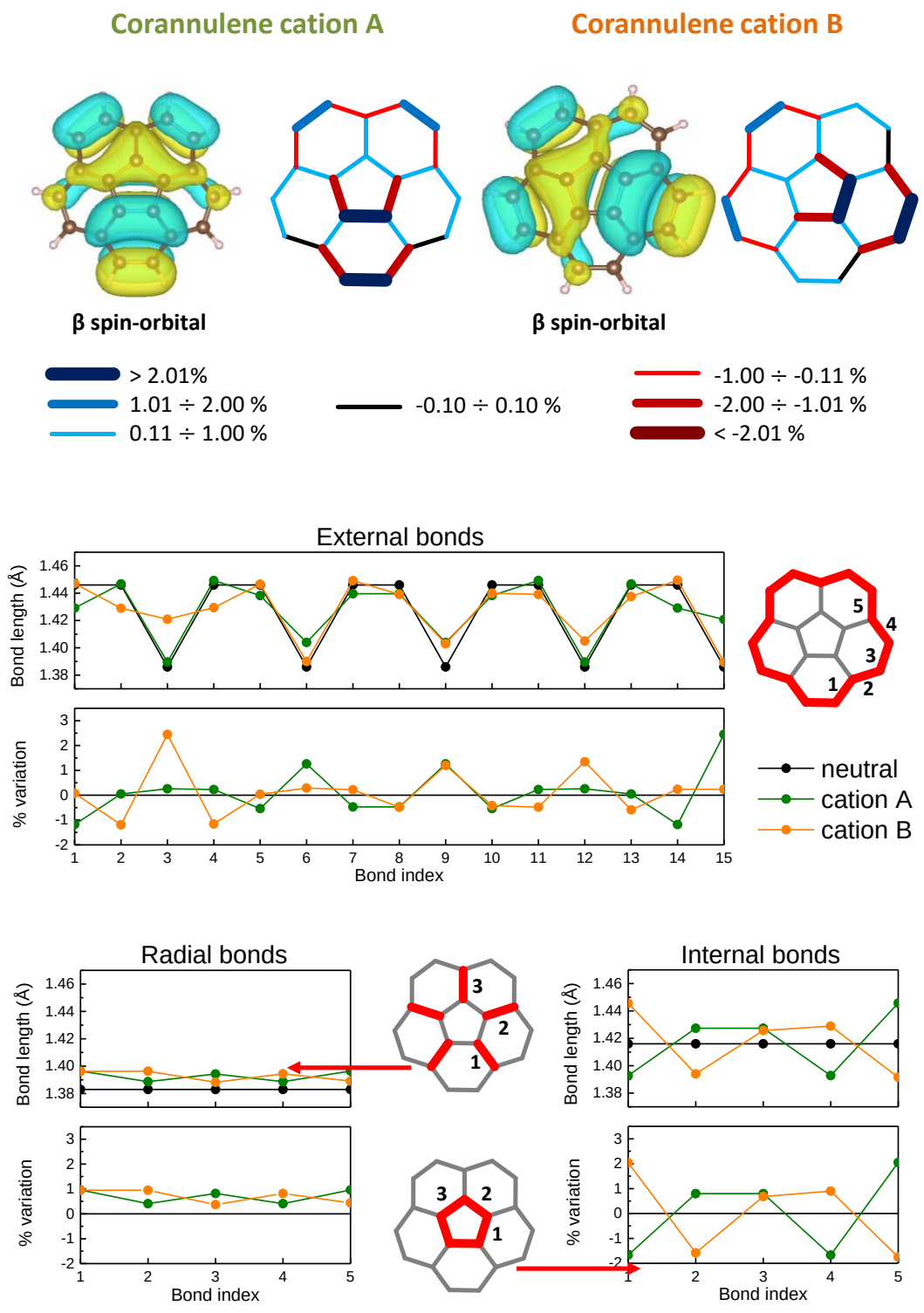

Figure 5.9 Jahn-Teller analysis of corannulene cations. In the upper part is reported a comparison between the lowest unoccupied spin-orbital and the variation of the bond length with respect to the neutral form (red bonds correspond to a shortening and blue bonds to an elongation). In the lower part is reported in a more explicit way the bond length for both the JT forms and the percentage variation with respect to the neutral. External, radial and internal bonds are reported in different graphs.

Table 5.5 Calculated energies and $\boldsymbol{g}$-tensor components for the ions of coronene and corannulene.

Radical	Energy (eV)	$\boldsymbol{g_X}$	$\boldsymbol{g_Y}$	$\boldsymbol{g_Z}$	$< \boldsymbol{g} >$
Coronene cation A	-25066.0579	2.00318	2.00207	2.00229	2.00252
Coronene cation B	-25066.0581	2.00207	2.00318	2.00229	2.00252
Corannulene cation A	-20883.9246	2.00289	2.00224	2.00233	2.00249
Corannulene cation B	-20883.9251	2.00224	2.00289	2.00233	2.00249
Coronene anion A	-25073.2549	2.00223	2.00326	2.00213	2.00254
Coronene anion B	-25073.2551	2.00326	2.00223	2.00212	2.00254
Corannulene anion A	-20891.8576	2.00242	2.00312	2.00169	2.00241
Corannulene anion B	-20891.8579	2.00312	2.00241	2.00169	2.00241

neutral C_{5v} molecule. The bond variations with respect of the neutral form are slightly higher than for coronene. In the anions the internal bonds varies up to 1 %, the radial bonds to 1.5 % and the external bonds to 2.5 %. For the cations, the larger variations for the internal bonds are about 2 %, for the radial 1 % and for the external 2.5 %. All the variations of radial bonds in corannulene ions are positive. The energy difference between the two anions is 0.0005 eV and between the two cations is 0.0003 eV (Table 5.5)

What we can see from the graphs of the bond length is that for coronene, anion and cation, the geometries of the two JT distorted form are very similar to each other, it is possible to obtain one by rotating the other by 60 degrees. For corannulene we have the same behavior, but with a rotation by 72 degrees.

After all the Jahn-Teller analysis, we studied the effects of the JT distortion on the $\boldsymbol{g}$-tensors. We calculated the $\boldsymbol{g}$-tensors for coronene and corannulene ions, taking into account the different JT forms. The results are collected in Table 5.5. The two JT forms, for each ion, have the same average g value and also the same z-component, as expected, since JT distortion is in the XY plan. The X and Y components indeed swap passing from a form to the other. The influence of the JT distortion on the $\boldsymbol{g}$-tensors is evident only if the X and Y components are considered.

One potentially interesting results is that corannulene has slightly smaller $\boldsymbol{g}$-tensors with respect to coronene. That could be an indication that the presence of the pentagonal ring in corannulene (that induces the curvature) causes a lowering of the tensor values.

This statement must be confirmed with other calculations on molecules with more than one pentagonal rings.

Table 5.6 Average g values for the radical anions and cations of the fullerene fragments. We have put into the table also the number of pentagonal rings in the molecules and the curvature parameters calculated according Equation x.x

Radical	N° 5-membered rings	C	<g> anion	<g> cation
C20H10	1	0.0206	2.0014	2.0025
C36H12	3	0.0105	2.0012	2.0025
C30H10	6	0.0070	2.0025	2.0032
C40H10	6	0.0028	2.0018	2.0026
C42H12	6	0.0163	2.0017	2.0027
C50H10	6	0.0031	1.9999	2.0024
C54H6	9	0.0016	2.0004	2.0018
C60	12	0.0000	1.9969	2.0016

5.4.4 - Fullerene fragments

The molecule that we have chosen to study the influence of the curvature induced by pentagonal rings on the $\boldsymbol{g}$-tensors can be considered as fragments of a Buckminsterfullerene with at least a C_3 or C_5 symmetry axis. Because of this symmetry, for the ions of all these molecule, JT distortion is expected, as in coronene and corannulene. Before calculating the $\boldsymbol{g}$-tensors we should, in principle, isolate each JT form. However, that would be very expensive from a computational point of view, since some of these radicals are quite large. Luckily, for coronene and corannulene we observed that the JT distortion affects only the X and Y components of the $\boldsymbol{g}$-tensor, so we decided to neglect the effects of the distortion and to consider only the average values. They are collected in Table 5.6.

In order to analyze the dependence of the g values from the curvature, we have to define a parameter that describes it. To do so, we first obtained the radius r of the fullerene, that is the molecule that have the higher curvature between those that we choose and the only one for which a radius can be defined. Then, for the other

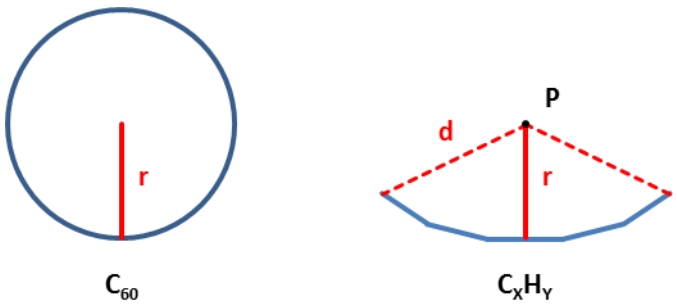

Figure 5.10 Geometrical definition of the procedure to calculate the curvature for our molecules.

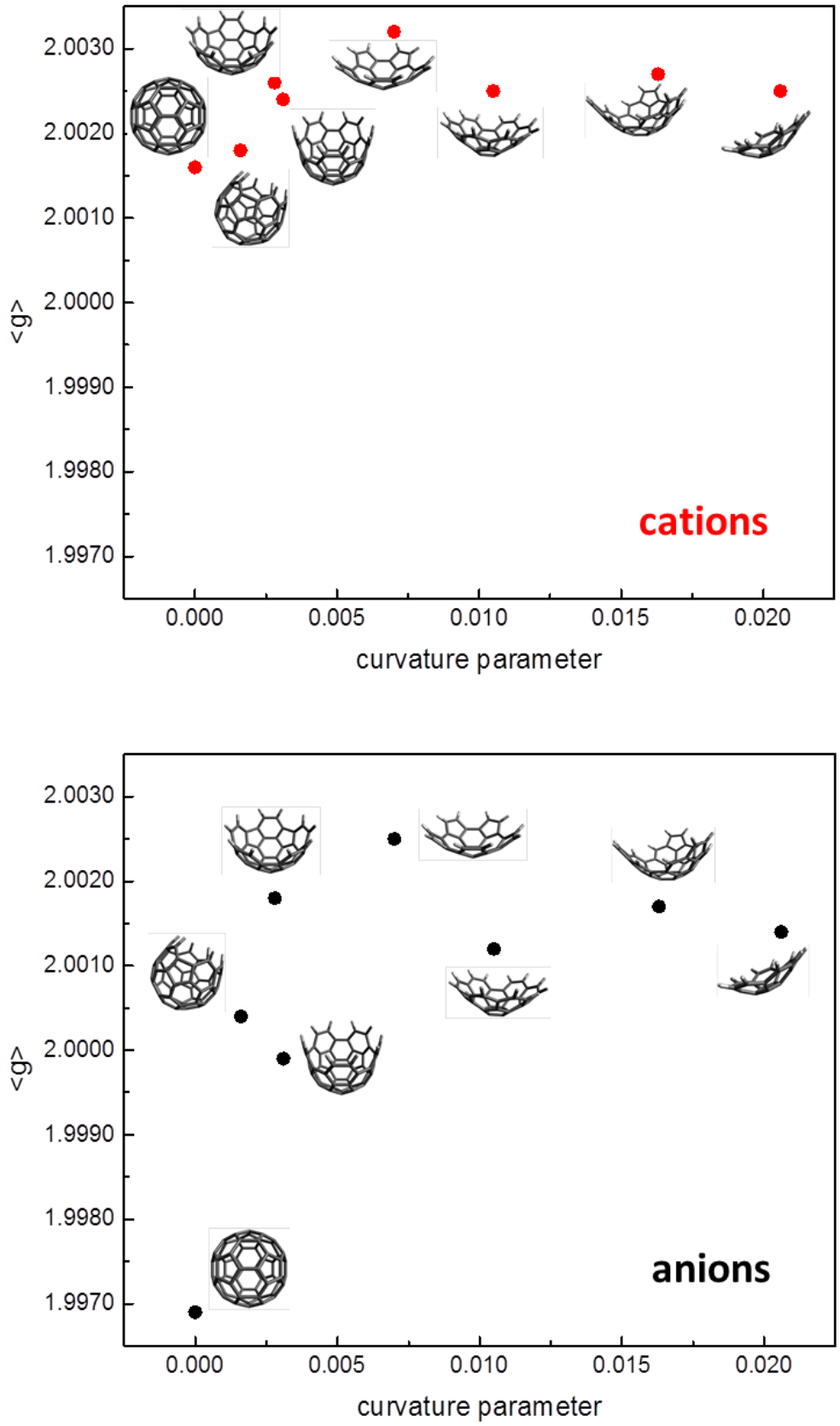

Figure 5.11 g-factor for cations (up) and anions (down) of the fullerene fragments as function of the curvature parameter defined from Equation 5.9. The structures are also reported.

molecules, we find the point P that is located on the straight line normal to the surface of the central ring of the molecule at a distance r from the plane of that ring (see Figure 5.10). Finally, we calculated the distances d_i between P and each carbon atom of the molecule. The curvature parameter C is then defined in according Equation 5.9

$$C = \frac{1}{n}\sum_{i=1}^{n}\frac{(d_i - r)^2}{r^2} \tag{5.9}$$

In this way we have $C = 0$ for fullerene and $C > 0$ for less curved molecules. The values of C for our molecules are collected in Table 5.6.

In Figure 5.11 are shown the g-values for the cations and anions as function of the curvature parameters. Going from lower to higher curvature, the g-value tends to decrease, both for cations and for anions. This tendency of the g-value to diverge from the free electron value can be explained by looking at the distances between the HOMO and the immediately higher energy levels in our molecules (Fig. 5.12). The energy difference decreases by increasing the curvature of the molecules. A lower energy difference implies a higher spin-orbit contribution to the $\boldsymbol{g}$-tensor, and therefore a higher deviation from g_e.

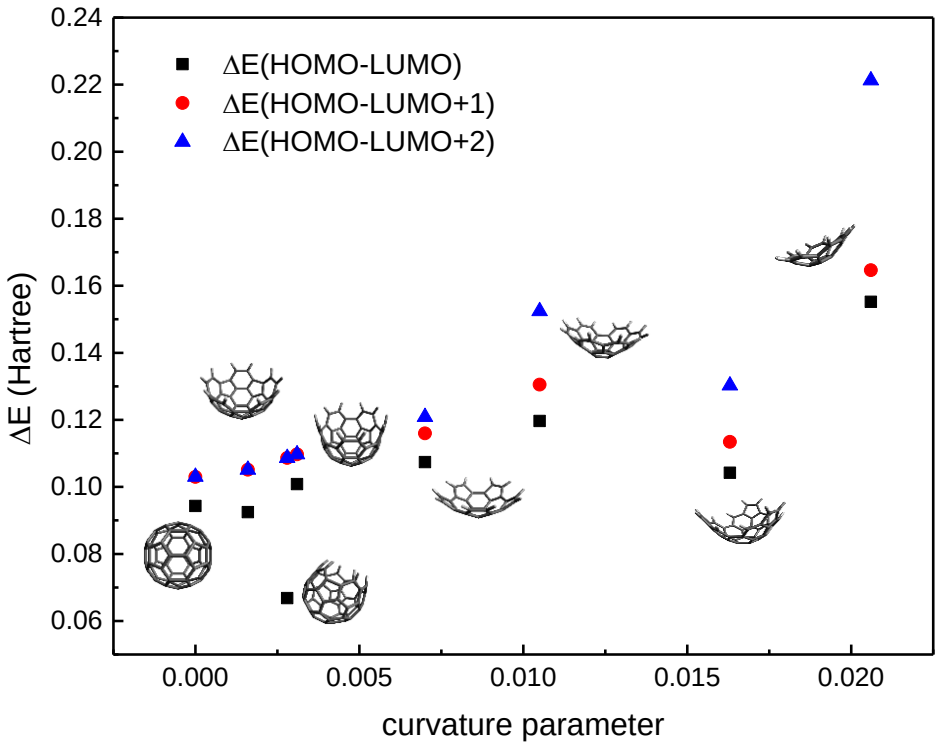

Figure 5.12 Energy difference between the HOMO and LUMO, LUMO+1 and LUMO+2 levels as function of the curvature parameter for the radicals cations. For the radical anions the trend is the same.

Moreover, from Figure 5.11, we observed that the anions of our models have always a lower g-value with respect to the corresponding cations. That is in contrast with what has been observed for smaller planar molecules [4], for which the g-factor is lower in the cations with respect to the anions. These different trends could be due to the curvature, but currently we do not have a clear explanation for this. Attempts to find a theory that describes our findings is underway.

5.5 - Conclusions

In this chapter we reported a DFT study on the $\boldsymbol{g}$-tensor of different molecular systems varying their shape and dimension.
Regarding the ribbons, we found that by increasing the length the $\boldsymbol{g}$-tensor values tend to those of ideal graphene. The curvature introduced by the methylene bridge instead does not affect appreciably the tensor. We can extend this finding to the analysis of the EPR spectra of graphene-like materials by affirming that the bending of the planes seems not to be related to the presence of low $g$values.
For coronene and corannulene, in addition to the calculation of the $\boldsymbol{g}$-tensor, we performed a full Jahn-Teller analysis of the radical cations and anions. This analysis was aimed at improving previous calculation reported in literature and to check the influence of the JT distortion on the tensor principal values. We found that the average value of the tensor is not affected by the distortion, so we neglected it in the calculation of the subsequent structures.
Than we studied a series of fullerene fragments with increasing curvature induced by the presence of pentagonal rings. In this case we found a correlation between the curvature and the $\boldsymbol{g}$-tensor values. The average values of the tensor become smaller by going from planar to curved structure and that explained by invoking a larger spin orbit contribution for the last. For the most curved structures we found g-values substantially lower than g_e. We found also that for our system, the radical anions have a lower $\boldsymbol{g}$-tensor with respect to the corresponding radical cations.

References

[1] F Tampieri, S Silvestrini, R Riccò, M Maggini, A Barbon. A comparative electron paramagnetic resonance study of expanded graphites and graphene, Journal of Materials Chemistry C. 2 (2014) 8105-8112.

[2] P Allemand, G Srdanov, A Koch, K Khemani, F Wudl, Y Rubin, et al. The unusual electron spin resonance of fullerene C60 anion radical, J.Am.Chem.Soc. 113 (1991) 2780-2781.

[3] A Thess, R Lee, P Nikolaev, H Dai, P Petit, J Robert, et al. Crystalline ropes of metallic carbon nanotubes, Science. 273 (1996) 483-487.

[4] F Gerson, Electron Spin Resonance Spectroscopy of Organic Radicals, Wiley-VCH, Weinham, 2003.

[5] JA Baldwin Jr. Electron paramagnetic resonance investigation of the vacancy in diamond, Phys.Rev.Lett. 10 (1963) 220.

[6] A Fionov, A Lund, W Chen, N Rozhkova, I Buyanova, G Emel'yanova, et al. Paramagnetic centers in detonation nanodiamonds studied by CW and pulse EPR, Chemical Physics Letters. 493 (2010) 319-322.

[7] A Shames, A Panich, W Kempiński, A Alexenskii, M Baidakova, A Dideikin, et al. Defects and impurities in nanodiamonds: EPR, NMR and TEM study, Journal of Physics and Chemistry of Solids. 63 (2002) 1993-2001.

[8] L Ćirić, A Sienkiewicz, B Nafradi, M Mionić, A Magrez, L Forro. Towards electron spin resonance of mechanically exfoliated graphene, physica status solidi (b). 246 (2009) 2558-2561.

[9] A Barbon, M Brustolon. An EPR Study on Nanographites, Applied Magnetic Resonance. 42 (2012) 197-210.

[10] V Likodimos, S Glenis, N Guskos, C Lin. Magnetic and electronic properties of multiwall carbon nanotubes, Physical Review B. 68 (2003) 045417.

[11] K Dinse, J van Tol, A Ozarowski, B Corzilius. Multi-Frequency EPR and DC Conductivity of Itinerant Spins in Single-Wall Carbon Nanotubes, Applied Magnetic Resonance. 37 (2010) 595-603.

[12] P Allemand, G Srdanov, A Koch, K Khemani, F Wudl, Y Rubin, et al. The unusual electron spin resonance of fullerene C60 anion radical, J.Am.Chem.Soc. 113 (1991) 2780-2781.

[13] R Barklie, M Collins, J Cunniffe, S Silva. An EPR study of defects in hydrogenated amorphous carbon thin films, Diamond and related materials. 7 (1998) 864-868.

[14] R Barklie. Characterisation of defects in amorphous carbon by electron paramagnetic resonance, Diamond and Related Materials. 12 (2003) 1427-1434.

[15] A Sadki, Y Bounouh, M Theye, J Von Bardeleben, J Cernogora, J Fave. Studies by electron paramagnetic resonance experiments of defects in hydrogenated amorphous carbon films as a function of annealing, Diamond and related materials. 5 (1996) 439-444.

[16] H Von Bardeleben, J Cantin, K Zellama, A Zeinert. Spins and microstructure of amorphous carbon, Diamond and related materials. 12 (2003) 124-129.

[17] M Kaupp, C Remenyi, J Vaara, OL Malkina, VG Malkin. Density functional calculations of electronic g-tensors for semiquinone radical anions. The role of hydrogen bonding and substituent effects, J.Am.Chem.Soc. 124 (2002) 2709-2722.

[18] M Kaupp, M Bühl, VG Malkin, Calculation of NMR and EPR parameters: theory and applications, John Wiley & Sons 2006.

[19] OL Malkina, J Vaara, B Schimmelpfennig, M Munzarova, VG Malkin, M Kaupp. Density functional calculations of electronic g-tensors using spin-orbit pseudopotentials and mean-field all-electron spin-orbit operators, J.Am.Chem.Soc. 122 (2000) 9206-9218.

[20] F Neese. Efficient and accurate approximations to the molecular spin-orbit coupling operator and their use in molecular g-tensor calculations, J.Chem.Phys. 122 (2005) 034107.

[21] G Schreckenbach, T Ziegler. Calculation of the G-tensor of electron paramagnetic resonance spectroscopy using Gauge-Including Atomic Orbitals and Density Functional Theory, The Journal of Physical Chemistry A. 101 (1997) 3388-3399.

[22] G Schreckenbach, T Ziegler. Density functional calculations of NMR chemical shifts and ESR g-tensors, Theoretical Chemistry Accounts. 99 (1998) 71-82.

[23] M Fujita, K Wakabayashi, K Nakada, K Kusakabe. Peculiar localized state at zigzag graphite edge, Journal of the Physical Society of Japan. 65 (1996) 1920-1923.

[24] Y Kobayashi, K Fukui, T Enoki, K Kusakabe, Y Kaburagi. Observation of zigzag and armchair edges of graphite using scanning tunneling microscopy and spectroscopy, Physical Review B. 71 (2005) 193406.

[25] B Kirste. Endor investigations of phenalenyl in polycrystalline durene and in liquid crystals, Chemical Physics Letters. 83 (1981) 465-468.

[26] Y Morita, S Suzuki, K Sato, T Takui. Synthetic organic spin chemistry for structurally well-defined open-shell graphene fragments, Nature chemistry. 3 (2011) 197-204.

[27] V Zaitsev, S Rosokha, M Head-Gordon, J Kochi. Steric modulations in the reversible dimerizations of phenalenyl radicals via unusually weak carbon-centered π-and σ-bonds, J.Org.Chem. 71 (2006) 520-526.

[28] A Reddoch, D Paskovich. The EPR spectrum of benzo [cd] pyrenyl, Chemical Physics Letters. 3 (1969) 351-352.

[29] F Banhart, J Kotakoski, AV Krasheninnikov. Structural defects in graphene, ACS nano. 5 (2010) 26-41.

[30] MJ Frisch, GW Trucks, HB Schlegel, GE Scuseria, MA Robb, JR Cheeseman, et al., Gaussian 09, revision E. 01, Gaussian Inc., Wallingford, CT. (2010).

[31] F Neese. The ORCA program system, Wiley Interdisciplinary Reviews: Computational Molecular Science. 2 (2012) 73-78.

[32] D Chong, Recent AdVances in Density Functional Methods, Part I, World Scientific: Singapore 1995.

[33] L Ćirić, A Sienkiewicz, B Nafradi, M Mionić, A Magrez, L Forro. Towards electron spin resonance of mechanically exfoliated graphene, physica status solidi (b). 246 (2009) 2558-2561.

[34] T Kato, K Yoshizawa, T Yamabe. Jahn–Teller effects in the coronene anions and cations, J.Chem.Phys. 110 (1999) 249-255.

[35] T Kato, T Yamabe. Jahn–Teller effects and charge transfer in the positively charged triphenylene and coronene, Chemical physics letters. 403 (2005) 113-118.

[36] T Sato, A Yamamoto, T Yamabe. Electronic and vibrational structures of corannulene anions, The Journal of Physical Chemistry A. 104 (2000) 130-137.

[37] T Sato, H Tanaka, A Yamamoto, Y Kuzumoto, K Tokunaga. Jahn–Teller effect in coronene monoanion: A comparative study with corannulene monoanion, Chem.Phys. 287 (2003) 91-102.

[38] T Yamabe, K Yahara, T Kato, K Yoshizawa. Vibronic coupling and Jahn-Teller effects in negatively charged corannulene, The Journal of Physical Chemistry A. 104 (2000) 589-595.

[39] K Komaguchi, K Nomura, M Shiotani, A Lund, M Jansson, S Lunell. ESR and theoretical studies of trimer radical cations of coronene, Spectrochimica Acta Part A: Molecular and Biomolecular Spectroscopy. 63 (2006) 76-84.

[40] P Krusic, E Wasserman. Coronene dication: a thermally accessible triplet, J.Am.Chem.Soc. 113 (1991) 2322-2323.

[41] BG Segal, M Kaplan, GK Fraenkel. Measurement of g values in the electron spin resonance spectra of free radicals, J.Chem.Phys. 43 (1965) 4191-4200.

[42] H Van Willigen, E De Boer, J Cooper, W Forbes. ESR Study of the Dimer Cation of Coronene, J.Chem.Phys. 49 (1968) 1190-1192.

[43] RJ Angelici, B Zhu, S Fedi, F Laschi, P Zanello. Electrochemical and EPR Studies of the Corannulene Ruthenium (II) Sandwich Complex [(η6-C6Me6) Ru (η6-C20H10)](SbF6) 2, Inorg.Chem. 46 (2007) 10901-10906.

[44] M Baumgarten, L Gherghel, M Wagner, A Weitz, M Rabinovitz, P Cheng, et al. Corannulene reduction: spectroscopic detection of all anionic oxidation states, J.Am.Chem.Soc. 117 (1995) 6254-6257.

[45] FB Bramwell, J Gendell. ESR Studies of Phosphorescent Corannulene; Evidence for Pseudorotation, J.Chem.Phys. 52 (1970) 5656-5661.

[46] G Zilber, V Rozenshtein, P Cheng, LT Scott, M Rabinovitz, H Levanon. Electron Spin Dynamics of Photoexcited Corannulene-Lithium Complexes in Tetrahydrofuran. Fourier Transform Electron Paramagnetic Resonance, J.Am.Chem.Soc. 117 (1995) 10720-10725.

[47] J Fawcett, J Trotter, The crystal and molecular structure of coronene, 289 (1966) 366-376.

[48] JC Hanson, C Nordman. The crystal and molecular structure of corannulene, C20H10, Acta Crystallographica Section B: Structural Crystallography and Crystal Chemistry. 32 (1976) 1147-1153.

[49] R Moss, A Perry. g-factor deviations in degenerate aromatic hydrocarbon radicals: the benzene anion, Mol.Phys. 22 (1971) 789-798.

[50] HA Galué, CA Rice, JD Steill, J Oomens. Infrared spectroscopy of ionized corannulene in the gas phase, J.Chem.Phys. 134 (2011) 054310.

CHAPTER 6 - REACTIVITY OF DEFECTS: SPIN TRAPPING STUDY OF THE CATALYTIC PROPERTIES OF LOCALIZED ELECTRONS IN CARBON-BASED MATERIALS

6.1 - Introduction

In this chapter a case-study for the reactivity of defects in carbon-based materials is reported. In particular we study the ability of localized electron to act as catalyst in a reaction of production of reactive oxygen species (ROS). We show that carbon particles can catalyze the reaction of formation of ROS, in particular of the superoxide/perhydroxyl radical. By using different kind of carbon materials with different sizes, we prove also the correlation between the particle sizes, that is related to the total concentration of defects, and the reaction rate. Since the radicals that we study in this chapter are very reactive, with very short half-lives, we used the spin trapping technique to detect them.

6.1.1 - Generation of reactive oxygen species

The effects of the airborne fine particulate matter (PM) on the human health is currently a hot debated topic in many scientific field [1]. Exposure to PM is one of the main causes of respiratory diseases such as asthma, decreased pulmonary function, lung cancer [2]. Particles inhalation has also adverse cardiovascular effects like hypertension, thrombus formation, myocardial infarction and many other cardiovascular diseases [3-6]. All this has a strong worldwide impact on the economy and is a high social burden in term of health care costs and quality of life [7,8].

For about fifteen years, many researchers have studied which components of PM are effectively responsible for the adverse effects on human health [9]. Recent evidences outline that these effects are strongly related with the chemical composition of the particles and not with their concentration [10-12]. Airborne particulate matter is a very complex by a chemical point of view [13]. Among the constituents of the fine fraction of PM (PM2.5), there are elemental carbon soot particles (carbon core), various organic aromatic compounds such as polycyclic aromatic hydrocarbons (PAH), inorganic ions and trace elements. Diesel exhaust particulate matter (DEPM) is largely representative of PM2.5 above all in highly polluted areas [14,15].

The adverse effects of PM on the human health have been often related to oxidative stress due to production of ROS inside the tissue. ROS, in particular superoxide and perhydroxyl radicals ($\cdot O_2^-$ or $\cdot O_2H$), were indeed measured, in biological and non-biological samples, in presence of particulate matter and of a proper initiator, with several techniques, including EPR, since they are paramagnetic [16]. Many studies have also shown that PAH and some of their quinone derivatives play a primary role

in the reaction of formation of these ROS [17]. Different types of quinones are commonly present in PM and DEPM, as combustion products or chemical PAHs derivatives. These species, among the PM components, were considered up to now to be the main source of ROS production. The reaction of ROS production catalyzed by quinones is reported in Scheme 6.1.

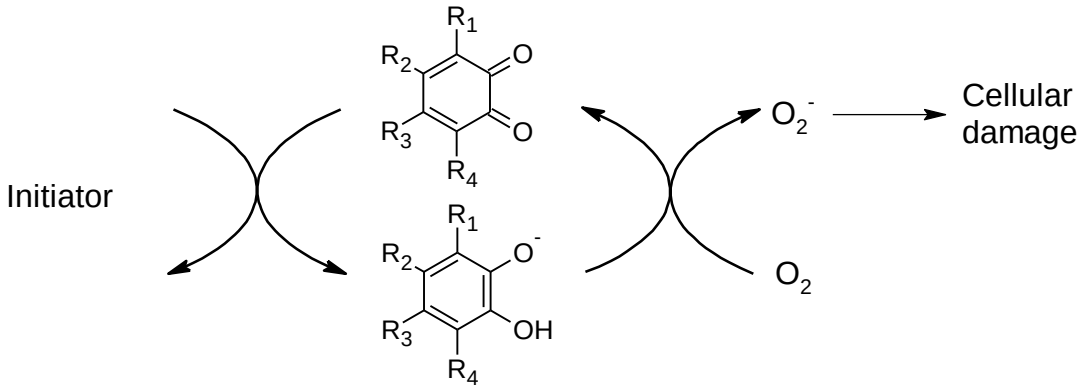

Scheme 6.1

The inorganic carbon that is present in the PM is characterized by lots of defects, vacancies, dangling bonds, etc. [18] and most of them are paramagnetic [19]. These species are in principle quite reactive and could catalyze the reaction depicted above together or in place of the quinones. The ROS that we want to study, due to their high reactivity, have very short lifetimes [20,21] and are therefore impossible to be detected as free radicals with standard techniques. In the next section, some of the most used techniques to detect ROS are described.

6.1.2 - Detection of oxygen free radicals

Free radicals are often very reactive and in liquid systems they are usually transient species that undergo very fast unimolecular (e.g., fragmentation and rearrangement) and/or bimolecular (e.g., dimerization, coupling, addition) termination reactions. If the reaction leading to the formation of a given radical in solution has a rate comparable to those leading to its termination, a steady-state concentration can be reached that is large enough to enable its detection. In most of cases, it is very rare that the steady-state concentration of transient radicals intervening in chemical reactions exceeds the detection threshold. Several methods have been developed to detect these highly reactive radicals. All these methods involve the transformation of the reactive radical into another more stable specie that can achieve a steady state concentration high enough to be detected.

Several ways have been developed and described to detect highly reactive radicals. Here we will examine the methods for the detection of the superoxide radical and the hydroxyl radical, since they are the radicals of interest in this work.

The most used methods for the detection of superoxide radicals include cytochrome c reduction, nitroblue tetrazolium reduction, spin trapping, etc. They are based on the ability of superoxide to reduce some compounds by one-electron transfer mechanism because such processes have high rates [22]

$$O_2^{\cdot -} + A \Longrightarrow O_2 + A^{\cdot -} \tag{6.1}$$

The reaction has to be exothermic to have a sufficiently high reaction rate. In this case, it is possible to have a quantitative superoxide detection.
The most frequently used method for superoxide detection is the one-electron reduction of ferric cytochrome c

$$O_2^{\cdot -} + cyt.c(III) \Longrightarrow O_2 + cyt.c(II) \tag{6.2}$$

This is an exothermic process and therefore, the equilibrium is completely shifted to the right; the re-oxidation of reduced cytochrome c by dioxygen is impossible. The oxidized and reduced forms of cytochrome c have different spectroscopic properties (different electronic and vibrational spectra), so can be easily detected and recognized. The rate if reaction 6.2 however is relatively low ($2.6 \cdot 10^5$ L mol^{-1} s^{-1}) if compared with similar reactions (usually 10^8-10^9 L mol^{-1} s^{-1}) and that limits the ability of cytochrome c to compete with other electron acceptors. Another drawback of the use of cytochrome c arises in the detection of superoxide in cells and tissue. Cytochrome c is unable to penetrate cell membranes and therefore, can be used only for the measurement of extracellular superoxide.
Another method to detect superoxide exploit chemiluminescence. One of the most used is the lucigenin-amplified chemiluminescence. The reactions are

$$O_2^{\cdot -} + Luc^{2+} \Longrightarrow O_2 + Luc^{+} \tag{6.3}$$
$$O_2^{\cdot -} + Luc^{+} \Longrightarrow LucO_2(decomposition) \Longrightarrow h\nu \tag{6.4}$$

Chemiluminescence is produced during the decomposition of excited dioxetane intermediate $LucO_2$. This is probably the most specific assay for superoxide detection; the efficiency and specificity of this method depends on the irreversibility of the whole process due to a high rate constant and a favorable thermodynamics of reaction 6.3 and a high rate of subsequent reaction 6.4. This method has been widely applied for superoxide detection in cell-free, cellular systems and in tissue [23-25]. Other chemiluminescent methods use luminol instead of lucigenin [26].
One of the oldest methods of superoxide detection is the oxidation of epinephrine. This method has the disadvantage of oxidizable compounds due to the possibility of the nonsuperoxide-mediated oxidation of epinephrine. However, sometimes this method is still used [27].

Nitroblue tetrazolium (NBT, 3,3'-(3-3'-dimethoxy-1,1'-biphenyl-4,4'-diyl)bis-2-(4-nitrophenyl)-5-phenyl-2H-tetrazolium dichloride) can be reduced by superoxide radical to form formazan as a final product, which can be measured spectrophotometrically [28]. The rate of the reaction is moderately high ($5.88 \cdot 10^4$ L mol^{-1} s^{-1} [29]), the production of formazan is not a one-electron process, the product comes from a disproportionation of intermediate free radicals. Similar to cytochrome c, NBT is easily reduced by other species that makes this method not widely used.
Two fluorescent probes dihydroethidium (DHE) and dichlorodihydrofluorescein (DCFH) are used for superoxide detection in biological systems [30]. Both assays have some drawbacks. Some studies concluded that these methods could not be reliable assays of superoxide detection in cells [31,32].
The only direct method of superoxide identification as free radical in solutions and in biological systems is the spin-trapping. This method will be described in details in the next section.

The detection of hydroxyl radical is more easy with respect to superoxide radical, since it is much more stable. The most used method is spin trapping that is described in the next section, but several other methods exist. Some of them are based on the ability of hydroxyl radicals to hydroxylate aromatic compounds, degrade deoxyribose, decarboxylate ^{14}C-benzoic acid, and produce ethylene from methionine [28]. These methods cannot differentiate between free hydroxyl and hydroxyl-like radicals (such as ferryl and perferryl ions). Recently some chemiluminescent methods have been proposed to detect hydroxyl radicals, but in most cases, the lifetime of the radical is too short to produce a meaningful level of chemiluminescence [33].

6.1.3 - Spin trapping technique

The spin-trapping technique enables to detect very reactive radicals, whose steady state concentration is too low to be detected with the conventional EPR techniques. This technique consists of adding to the system a small amount of a diamagnetic molecule (a spin-trap) to the solution where reactive radicals are produced. These molecules rapidly react with the radicals to form a persistent radical specie, whose concentration accumulates and can reach detectable levels. The resulting radical is called spin-adduct. The process can be schematized by the following reaction, where ST and SA stand for spin trap and spin adduct

$$ST + radical \Longrightarrow SA \qquad (6.5)$$

The spin-trapping techniques has been introduced in the late 1960s, and since then it has been applied to a huge number of systems with a high variety of conditions. Spin trapping can be carried out in liquid, gaseous or solid phase, but it is mostly exploited in the liquid phase. Some information about spin trapping in solid and

gaseous phase can be find in [34].
A spin trap is a molecule that can undergo homolytic addition, but that alone is not enough. A good spin-trap should have the following properties:

- Should be stable under the reaction conditions
- Should not participate to any side-reaction leading to unwanted paramagnetic species
- Should react rapidly with the radical of interest
- Should form spin adducts that are as much stable as possible
- Should form spin adduct with simple EPR spectra
- Should provide the largest possible structural information on the trapped species

Over the years, a great variety of spin-trapping agents has been developed. For each situation, it is necessary to choose carefully the most suitable one. The most commonly used spin traps are aliphatic or aromatic nitroso and open-chain or cyclic nitrones. In both cases, the resulting spin adducts are nitroxides [34].
The spin adducts from the two types of compounds are different. In those from nitroso derivatives, the trapped radical is directly bound to the nitrogen of the nitroxidic function, whereas in those from nitrones it is bound to the carbon atom adjacent to it. In the case of nitroxides deriving from nitrones, the nitrogen hyperfine splitting does not depend much on the nature of the trapped radical and useful information can be derived only from the variations of the α-hydrogen hyperfine coupling constant (hfcc). Nitrogen splitting is slightly indicative also in nitroxides from cyclic nitrones, which exhibit variations of the α-hydrogen hfcc that are larger than those observed for nitroxides from open chain nitrones.
Here we will focus on cyclic nitrones, since the spin trap that we used in this work belongs to this type, but there are also many other spin traps. Most of them are described in [34]. A variety of cyclic nitrones has been successfully exploited in spin trapping experiments, and those belonging to the 1-pyrroline family are by far the most widely employed. The most used spin trap of the family is 5,5-dimethyl-1-pyrrolyne N-oxide (DMPO, Scheme 6.2).

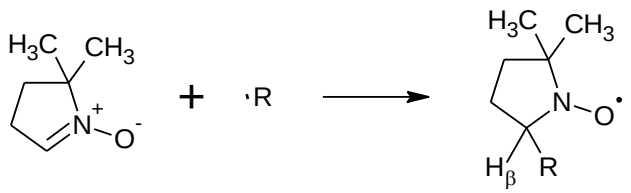

Scheme 6.2

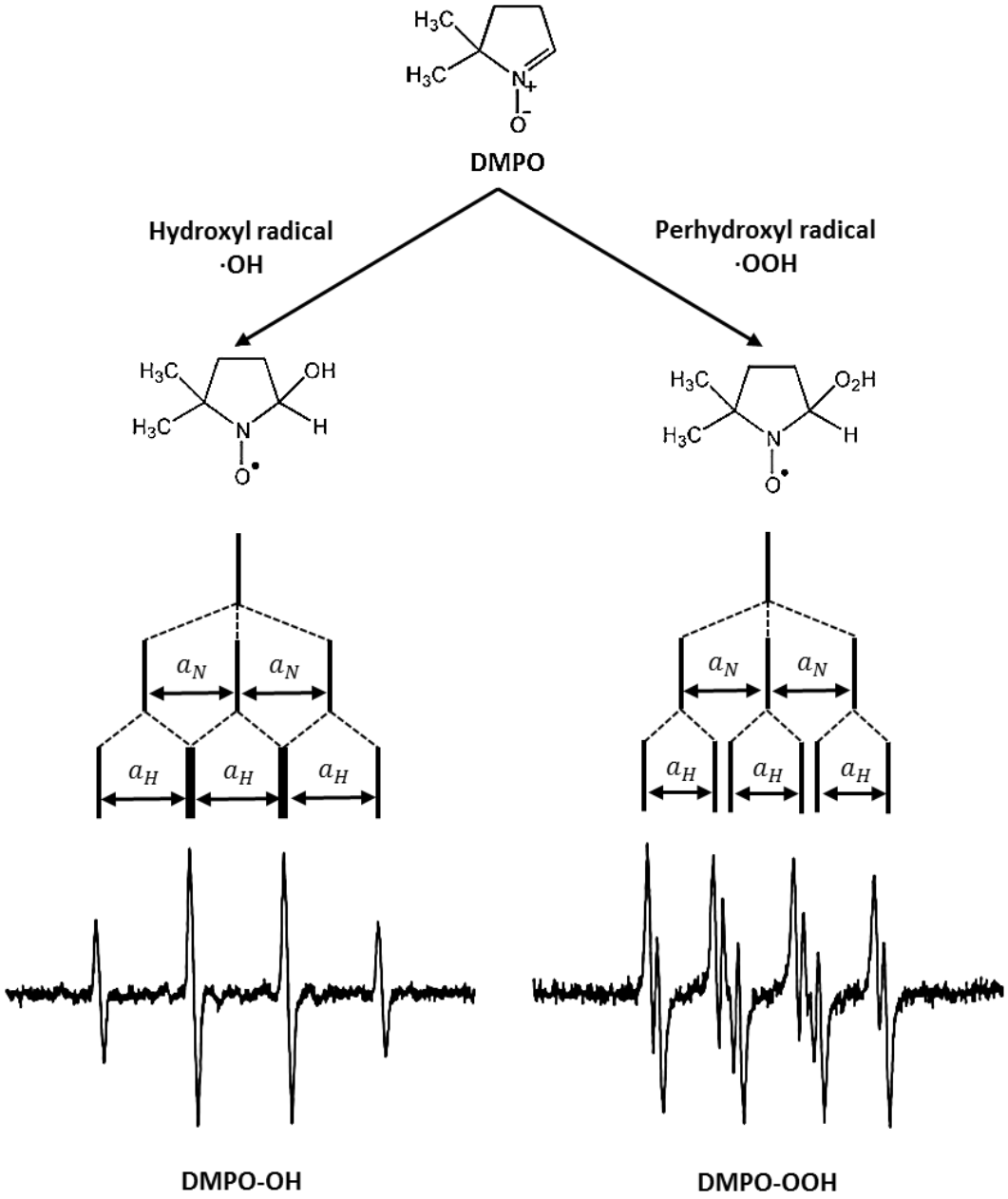

Figure 6.1 Structures, stick-plots and experimental spectra of the spin adducts of DMPO with hydroxyl and perhydroxyl radicals.

The presence of the two β-methyl groups disfavor disproportionation of the resulting spin adducts, that consequently are more persistent. For the spin adduct derived from DMPO the main information about the nature of the trapped radicals comes from the value of the hyperfine coupling constant of the β-hydrogen atom. The β-hydrogen splittings in the DMPO spin adducts vary with the nature of the trapped radical over a much wider range than that of the corresponding nitroxides from acyclic nitrones, although not so much within a single family of radicals. Thus, the β-hydrogen hyperfine splitting constant is $a_{\beta H} \geq 20$ G for the adducts of alkyl radicals, $15 \leq a_{\beta H} \leq 20$ G for those of thiyl radicals, and $6 \leq a_{\beta H} \leq 8$ G for those of alkoxy

radicals. The spectra of these last species generally exhibit an additional small splitting due to one of the γ-hydrogen atoms.
DMPO is widely used for spin-trapping experiments in biological systems since it is water-soluble, can pass through the cell membranes, it is easy available and relatively cheap. In particular it's used for detection of oxygen radicals (the hydroxyl radical, the perhydroxyl radical and its conjugated base, the superoxide radicals) whose spin adducts have very distinctive EPR spectra. The structure of the spin adducts and the relative EPR spectra are reported in Figure 6.1.
The spectrum of the DMPO-OH spin adduct is made of four lines with relative intensity 1:2:2:1 due to the hyperfine coupling with the nitrogen atom (a_N =14.87 G) and the β-hydrogen atom ($a_{\beta H}$ =14.81 G). The spectrum of the DMPO-OOH adduct instead is compose of six lines all with the same intensity due to the hyperfine coupling with the nitrogen atom (a_N =14.3 G) and the β-hydrogen atom ($a_{\beta H}$ =11.7 G); each line is also splitted in two by the small coupling with one of the γ-hydrogen atoms ($a_{\gamma H}$ =1.25 G).
The spin adduct DMPO-OOH is rather unstable (the half-life of DMPO-OOH ranges from 27 s at pH 9 to 91 s at pH 5 [35]). Another disadvantage of using DMPO is a low rate of reaction with superoxide. Nonetheless the spin trapping of superoxide is the only direct method to identify this radical in biological systems. It has been used widely in various in vitro systems [36]. The DMPO-OOH adduct decomposes quickly yielding the DMPO-OH adduct (Scheme 6.3), the latter is frequently used for the measurement of superoxide formation.

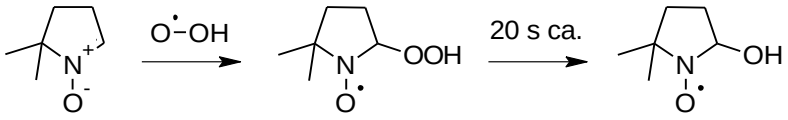

Scheme 6.3

As already said before, the adduct of DMPO with the perhydroxy radical has a very short half-life, of about 20 s [37], so in the majority of the cases the EPR spectrum of superoxide adduct is hardly seen as it interconverts rapidly to the hydroxyl adduct, so that it' s experimentally more easy to determine the concentration of the hydroxyl adduct.

6.2 - Experimentals

In this work we studied different types of carbon-based materials as possible catalyst in the reaction of generation of ROS: ball milled nanographites, nanosized amorphous carbon and Diesel exhaust particulate matter (DEPM).
Pure crystalline graphite powder was obtained from Aldrich (100 mesh, 99.99% purity, CAS no. 7782-42-5, catalog no. 49,658-8). The graphite was milled in

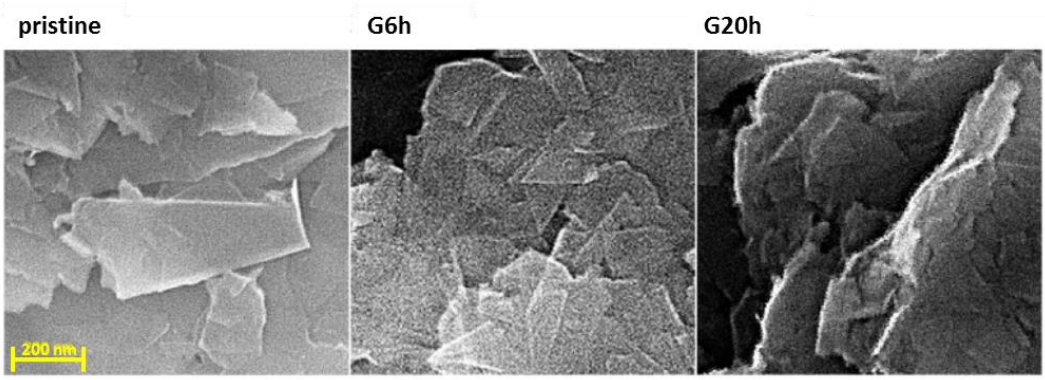

Figure 6.2 SEM images of crystalline graphite powder samples pristine and subsequently ball-milled for increasing times.

Dipartimento di Chimica, Materiali e Ingegneria Chimica, Politecnico di Milano in a Retsch MM301 ball miller (30 Hz oscillation frequency, steel balls and vials). Three types of nanographites were used, corresponding to different grinding times of 90, 360 and 1200 min (G1.5h, G6h, G20h). Their size decreases by increasing the milling time and consequently the amount of defects increases (Fig. 6.2). The characterization of these nanographites has been published in [38] and in [39].

Nanosized carbon (NC) has been purchased from Sigma Aldrich and used as received. It has an amorphous structure, particle size less than 50 nm (TEM measurements) and degree of purity ≥ 99%. Before using this sample as catalyst, we characterized it by cw-EPR. The results of the characterization are reported in the first part of the result section.

Standard reference DEPM was purchased from NIST (USA).

We used DMPO as spin trap and DTT (Dithiotreitol) and TCEP (*tris*(2-carboxyethyl)phosphine) (Scheme 6.4) as initiators for the reaction; all of them were purchased from Sigma Aldrich and used as received.

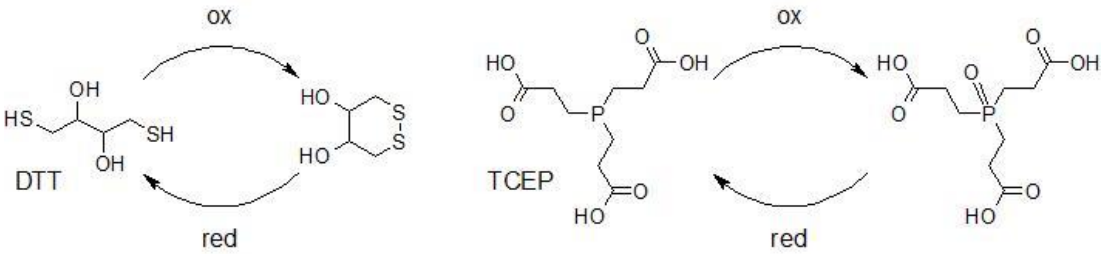

Scheme 6.4

The solutions for the spin trapping experiments were prepared in TRIS buffer 50 mM. For the preliminary EPR characterization, NC powder was put inside a 2x3 ID quartz tube and sealed under vacuum. The cw-EPR measurements were obtained with an X-band Bruker ELEXYS spectrometer, equipped with a dielectric resonator and a nitrogen gas-flow cryostat for low temperature measurement. The determination of the spin concentration was done using a Mn(II) standard as a reference.

For the spin trap experiments we prepared the following solutions:

- 500 µL of DMPO (200 mM in buffer) + 5 µL of DTT (or TCEP) (10 mM in buffer)
- 500 µL of DMPO (200 mM in buffer) + 5 µL of DTT (or TCEP) (10 mM in buffer) + 20 µL of DEPM (1 mg/mL suspension in buffer)
- 500 µL of DMPO (200 mM in buffer) + 5 µL of DTT (or TCEP) (10 mM in buffer) + 20 µL of G20h (1 mg/mL suspension in buffer)
- 500 µL of DMPO (200 mM in buffer) + 5 µL of DTT (or TCEP) (10 mM in buffer) + 20 µL of G6h (1 mg/mL suspension in buffer)
- 500 µL of DMPO (200 mM in buffer) + 5 µL of DTT (or TCEP) (10 mM in buffer) + 20 µL of G1.5h (1 mg/mL suspension in buffer)
- 500 µL of DMPO (200 mM in buffer) + 5 µL of DTT (or TCEP) (10 mM in buffer) + 20 µL of NC (1 mg/mL suspension in buffer)

The carbon materials do not suspend well in aqueous solution, we sonicated them in order to obtain a good dispersion and then quickly transferred it prior deposition of the powder. We didn't use DMSO to suspend the materials because it interferes with the EPR measurements generating a paramagnetic adduct with DMPO (DMPO-Me).
The order in which the reagents were included is the following: 1) DMPO; 2) carbon material (if present); 3) initiator. Each solution, immediately after the preparation, was transferred in a flat cell and it was rapidly introduced in the EPR spectrometer. The spin trap measurements were done at room temperature with a X-band Bruker ELEXSYS spectrometer equipped with a ER 4103TM cylindrical mode resonator for aqueous and high-dielectric samples. We collected single-scan spectra at different delays after the mixing of all the reagents in order to follow the evolution of the EPR signals in time.
All the EPR spectra were reproduced with proper simulation programs written using Easyspin [40] in order to isolate and identify all the radicals.

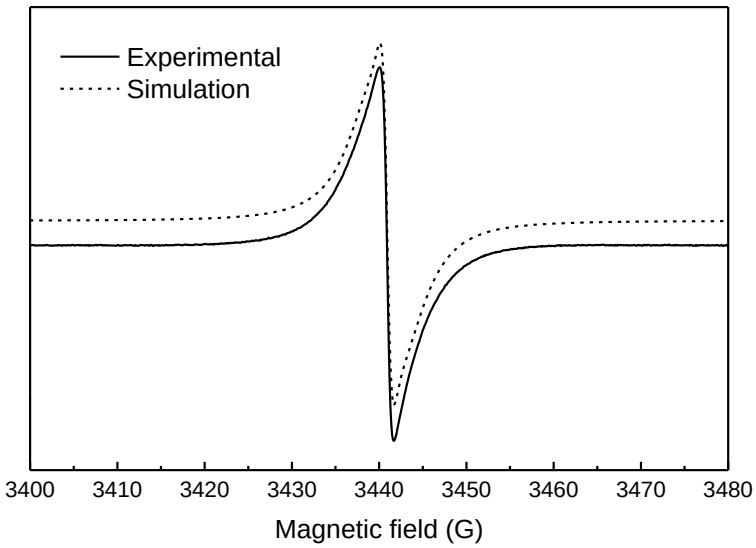

Figure 6.3 Experimental (black) and simulated (red) cw-EPR spectrum of Nanocarbon powder at room temperature.

Table 6.1 Parameters obtained from the simulation of the cw-EPR spectra of sample NC at different temperatures. C_1 and C_2 are the intensities of the two components and Γ_1 and Γ_2 are their linewidth. Both the components have Lorentzian lineshape.

T (K)	C_1	C_2	Γ_1 (G)	Γ_2 (G)
290	0.173	1.977	1.07	3.99
260	0.215	2.405	1.09	4.06
230	0.232	2.588	1.12	4.13
200	0.259	2.911	1.20	4.24
170	0.288	3.592	1.26	4.30
140	0.282	3.998	1.29	4.45

6.3 - Results

6.3.1 - cw-EPR characterization of sample NC

The cw-EPR spectra for the NC sample alone were collected between room temperature and 140 K. In Figure 6.3 the spectrum at room temperature is reported. The absolute concentration of spins for this sample, determined by comparison of the spectrum of a standard with known spin concentration, is $2.5 \cdot 10^{15}$ spins/g (30% error).

The spectra collected at different temperatures have been simulated using two components with Lorentzian lineshape without any constraint. All the simulations reproduced perfectly the experimental spectra. The parameters obtained from the simulations are collected in Table 6.1. The trend of the intensity of the two components with respect to the temperature is in Figure 6.4.

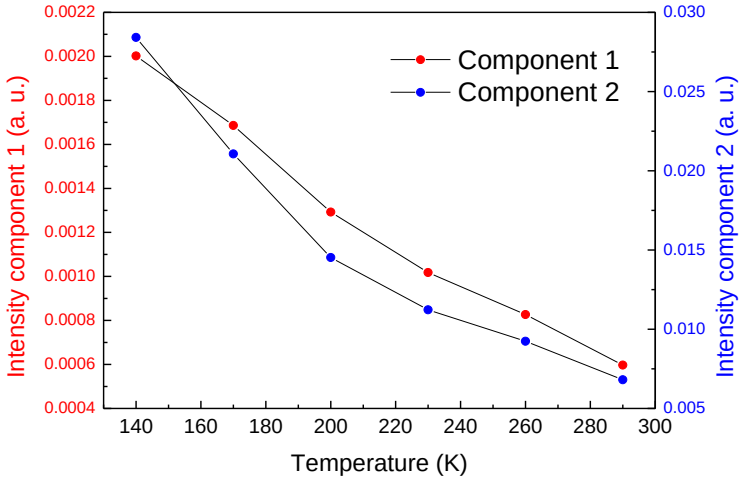

Figure 6.4 Intensity of the two components of the cw-EPR spectra of sample NC as function of the temperature.

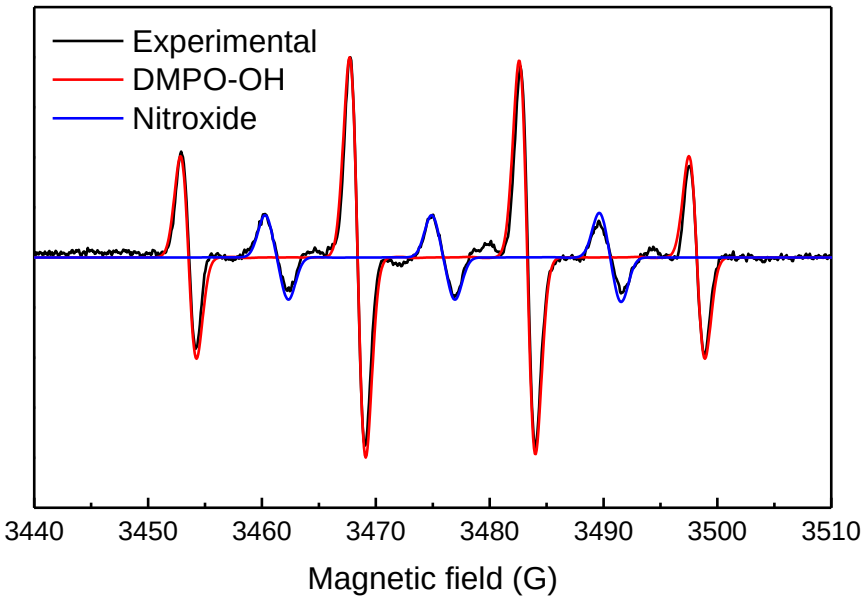

Figure 6.5 Typical cw-EPR spectrum obtained in presence of the initiator (DTT or TCEP) and DMPO. Two species are evident: a free nitroxide (blue) and the adduct DMPO-OH (red).

6.3.2 - Spin-trapping measurements

We performed many spin trapping experiments, with and without the carbon-based materials, varying the type of carbon material used (Nanographites, NC or DEPM) and varying the initiator (DTT or TCEP). In Figure 6.5 is reported a typical cw-EPR spectra that we obtained. Two species are evident. One is the spin adduct of DMPO with the hydroxyl radical DMPO-OH and the second one has the typical EPR characteristic of a free nitroxide (three lines with same intensity separated by 15 G ca.). With EPR we could observe the time-variation of the intensity of the adduct DMPO-OH. We followed the growth of the signal of DMPO-OH, supposing that this adduct is

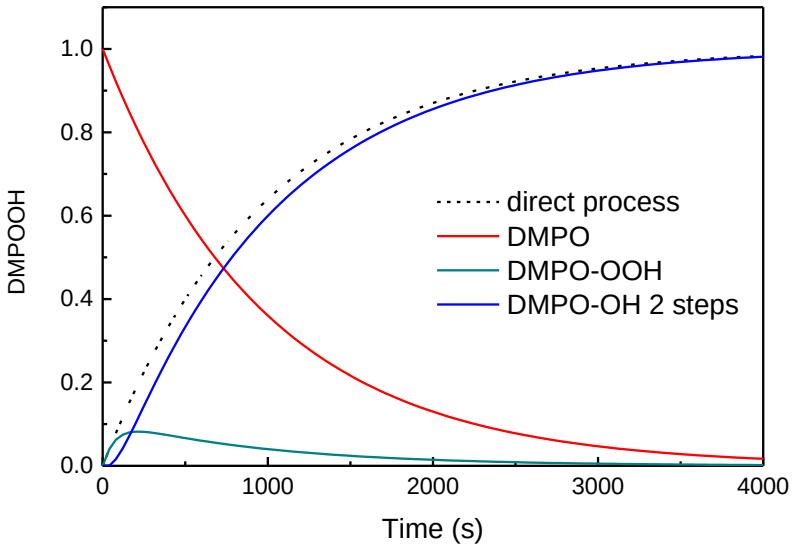

Figure 6.6 Simulation of the kinetics of the species involved in the decomposition reaction of the spin adduct DMPO-OOH. The rate constants are similar to the experimental ones.

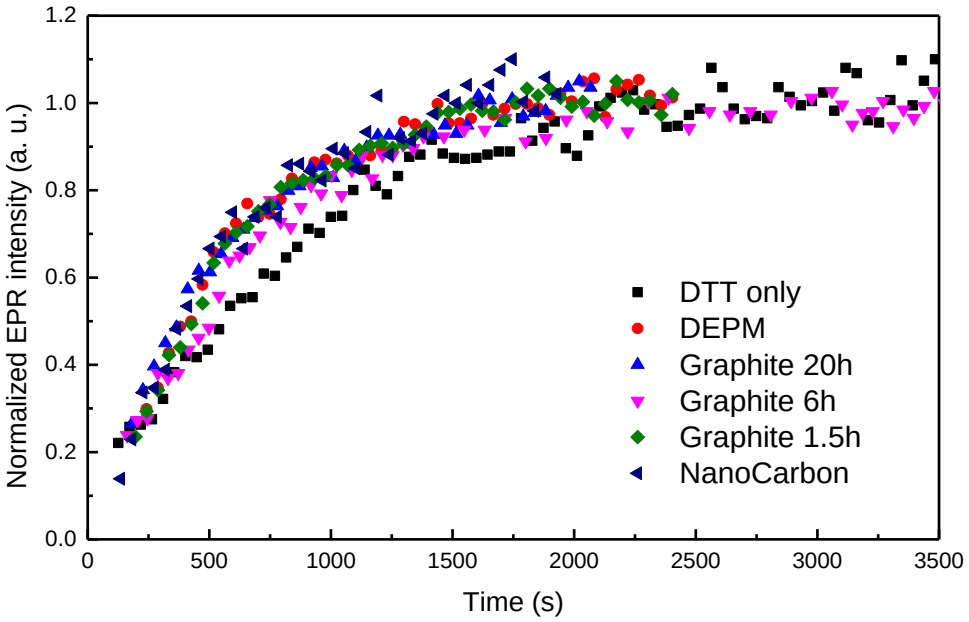

Figure 6.7. Intensities of the EPR spectra for all the solutions studied recorded at different delays from the mixing of the reagents.

generated by decomposition of DMPO-OOH according the reaction reported in Scheme 6.3. The DMPO-OOH lifetime is short enough to not change appreciably the growth profile of DMPO-OH. In Figure 6.6 is represented a simulation with rate constants similar to the experimental one and they show that an intermediate (DMPO-OOH) with a decomposition rate about 10 time higher than its formation rate does not affect much the growth of the signal of DMPO-OH. The intensity of the signal of DMPO-OH was recorded at different delays from the mixing of the reagents for all the solutions listed above. The data are reported in Figure 6.7 and the normalized time constants obtained from the fitting of the kinetic traces in Table 6.2. In some cases, for very short delays, we managed to obtain and isolate a signal that match the spectra of the adduct DMPO-OOH reported in literature [37]. The simulation of this spectrum confirms the attribution. The spectrum is reported in Figure 6.8.

Table 6.2 Normalized time constants obtained from the exponential fitting of the kinetic traces in Fig. 6.7.

System	τ/τ_0
DMPO + DTT	1.00
DMPO + DTT + DEPM	0.56
DMPO + DTT + G20h	0.62
DMPO + DTT + G6h	0.64
DMPO + DTT + G1.5h	0.56
DMPO + DTT + NanoCarbon	0.59

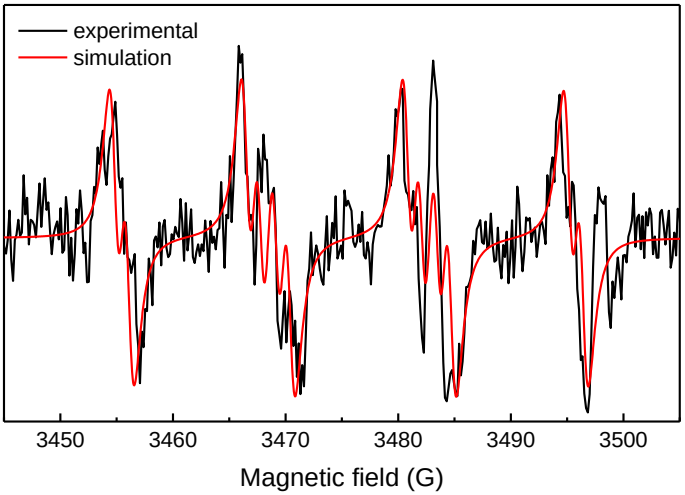

Figure 6.8 Experimental (black) and calculated (red) spectra of the adduct DMPO-OOH. The simulation has been obtained using parameters from [37].

6.3.3 - Raman measurements

The Raman measurement were done in Politecnico of Milan by the group of Prof. Giuseppe Zerbi. They used the same initiators that we used for the spin trapping measurement and as carbon materials they used pristine graphite, graphite milled for 10 and 20 hours (G10h and G20h), and nanocarbon (NC). In order to observe the superoxide radical formation, cytochrome c reduction was used. In presence of superoxide radical, cytochrome c is reduced (Scheme 6.5) and this reaction can be studied by Raman spectroscopy since the oxidized and reduced forms of cytochrome c have different Raman spectra.

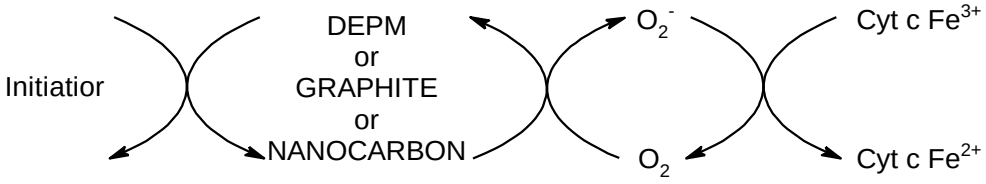

Scheme 6.5

The kinetics of the reaction of reduction of cytochrome have been recorded by Raman spectroscopy, varying the carbon-based catalyst. The kinetics have been analyzed by interpolation with exponential functions and the time constants have been obtained. In Figure 6.9 are reported the time constants of the reaction as function of the D/G ratio of the carbon materials.

The D/G ratio, in a carbon based material, is related to the total amount of defects that are present in the material and varies with the dimension; smaller sizes correspond to a higher concentration of defects, since the defects are localized mostly at the edges, which corresponds to a higher D/G ratio.

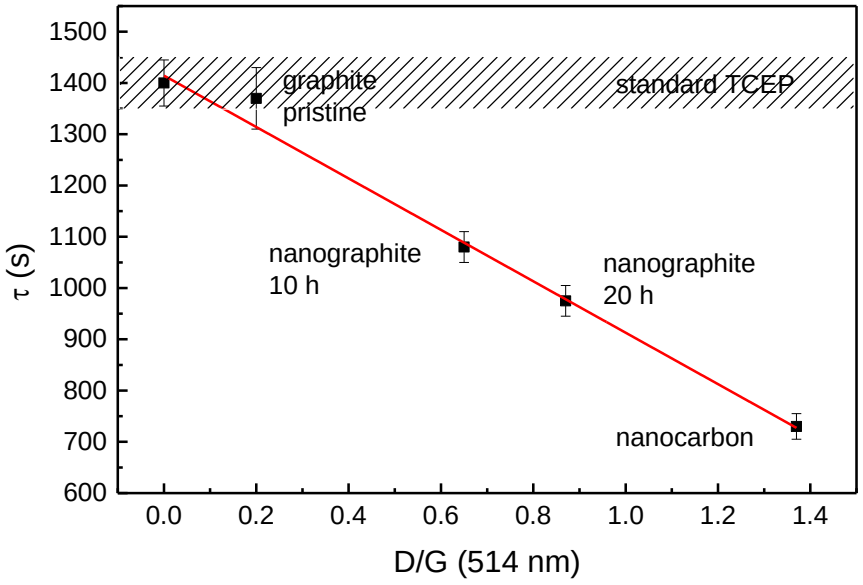

Figure 6.9 Time constants for the reaction of superoxide production measured by Raman using cytochrome c as function of the D/G ratio of the carbon particles used to catalyze the reaction

6.4 - Discussion

The EPR spectrum of NC powder is typical carbon-based radicals. We didn't observe signals due to metallic impurities. The signal is symmetric and quite intense. That means that it's not due to mobile electrons since in that case we would have observed an asymmetric lineshape [41,42]. The sample has also a low electrical conductivity since we did not observe an evident worsening of the Q-factor of the EPR cavity when we inserted the tube with the sample in it. From the simulation of the spectra at different temperatures we found out that the EPR signal can be well reproduced as a sum of two components, both with Lorentzian lineshape and isotropic g-tensor, no hyperfine coupling with paramagnetic nuclei has been observed, that is also a good indication of the material purity. The intensity of each component increases by lowering the temperature showing a Curie or Curie-Weiss behavior [43,44]. All these confirm that the EPR signal for the NC sample is due to localized electrons, probably in defect or edge states.

The EPR characterization NC, together with the characterization of the nanographites enabled us to verify the presence of localized electrons and to quantify them. Moreover, we have proven the chemical purity of these materials. This of paramount importance, since in the spin trapping measurements we require the materials to be as pure as possible. In particular we must be sure that there are no metallic impurities that could act ac catalyst for the reaction of ROS generation and no organic functional groups, like quinones, because our aim is to prove that localized electrons themselves

could act as catalysts.

The spin trapping measurement of the kinetic of formation of the spin adduct DMPO-OH enable to prove that the reaction of formation that radical is indeed catalyzed by the presence of carbon materials. For all the carbon materials used in this work, the reaction goes about twice as fast as in presence of the initiator alone. DEPM is a very complex material and has many organic functional groups, including quinones, which are known to participate to the reaction. On the other side, nanographites and nanocarbon are almost completely composed of carbon, so we assume that their catalytic activity implies the participation of defect states to the reaction since they are known to be highly reactive species.
With spin trapping we could not differentiate the carbon materials that we used. We observed the same effects for all of them within the experimental error.
One of the major findings of the spin trapping measurement was the isolation of the EPR spectrum of the DMPO-OOH spin adduct, that proves unequivocally the formation of the superoxide radical in our reaction conditions and confirms the validity of the assumption that the DMPO-OH spin adduct derives from the decomposition of the DMPO-OOH spin adduct, and not from other sources. As already said, this specie have a very low half-life, but by working very rapidly, we managed to recorder and to isolate its spectrum; this is the only way to prove directly the formation of such type of radical [45]. Despite the not optimal signal to noise ratio of the spectrum, it is very well reproduced by the simulation. The parameters used to obtain the simulation are exactly the same that are usually reported in literature for the DMPO-OOH spin adduct.
The spin adduct was observed at very short delays after the mixing of all reagents regardless of the type of carbon-based material used. This means that the production of superoxide radicals happens in presence of all carbon materials used in this work and then it decomposes into the other more stable spin-adduct that was observed in all our EPR spectra.

All these findings done by the spin trapping technique are confirmed by the Raman measurement. Raman spectroscopy proved also an increase of reaction rate of ROS generation in presence of carbon materials and provided a good indication of the presence of superoxide radical in the reaction condition. Cytochrome c was used to detect the superoxide radical with Raman since its Raman spectrum changes if cytochrome is in the oxidized or reduced form. As said in the introduction, cytochrome c reduction is not a fully reliable method to detect superoxide radical, since it is not completely specific for this radical. Anyway in the conditions used for the Raman measurements reported in this work, there are no competitors of superoxide to the reduction of cytochrome c, so Raman also proved indirectly the formation of superoxide radicals in presence of carbon materials.

In addition to all this, Raman spectroscopy could also differentiate between pristine graphite, graphite milled for 10 and 20 hours (G10h and G20h), and NC. It was possible to find a very nice linear correlation between the reaction rates and the D/G ratio of the carbon materials. The G band in the Raman spectrum of a carbon material is related to its structure while the D band to the amount of defects, in particular at the edges. Therefore, the D/G ratio is a very good indication of the defectivity of a material, higher the ratio is, higher the concentration of defects, that, in turn, is related to the particles dimensions. The decreasing order of particles size for the used materials is: pristine graphite < G10h < G20h < NC. The catalytic activity of the materials goes exactly with the same order. NC has the highest catalytic activity of the series and accelerate the reaction of about a factor two.

6.5 - Conclusions

The findings of this work prove unequivocally that the reaction of production of ROS, in particular of superoxide radical, is accelerated not only in presence of DEPM, but also with nanographites and nanocarbon as catalyst. This is an important and direct proof that the reaction doesn't necessary require the quinoid groups as was believed so far but also the edge and defect states in carbon-based materials can play an important role in the reaction.
With EPR we could detect directly the signal of the superoxide radical. That is a very important result since it is a univocal proof of the formation of that specie with all the carbon materials that we studied.
The Raman measurements enabled to find a clear correlation between the dimension of the carbon particles and the rate of the accelerated reaction of production of ROS. Smaller particles, corresponding to higher concentration of defects, have a higher catalytic activity.
This study can lead to the conclusion that the dangerous effects of the particulate on human health are not to be imputed only to the organic part, but also to the inorganic carbon part. This statement need to be confirmed by measurement in living cells that are scheduled in collaboration with the group of Prof. Marina Camatini from the Department of Enviromental Science at the University of Milan Bicocca.

References

[1] CI Davidson, RF Phalen, PA Solomon. Airborne particulate matter and human health: a review, Aerosol Science and Technology. 39 (2005) 737-749.

[2] ZD Ristovski, B Miljevic, NC Surawski, L Morawska, KM Fong, F Goh, et al. Respiratory health effects of diesel particulate matter, Respirology. 17 (2012) 201-212.

[3] R Brook. Cardiovascular effects of air pollution, Clin.Sci. 115 (2008) 175-187.

[4] RD Brook. Why physicians who treat hypertension should know more about air pollution, The Journal of Clinical Hypertension. 9 (2007) 629-635.

[5] AJ Lucking, M Lundback, NL Mills, D Faratian, SL Barath, J Pourazar, et al. Diesel exhaust inhalation increases thrombus formation in man, Eur.Heart J. 29 (2008) 3043-3051.

[6] A Peters, DW Dockery, JE Muller, MA Mittleman. Increased particulate air pollution and the triggering of myocardial infarction, Circulation. 103 (2001) 2810-2815.

[7] J Leal, R Luengo-Fernandez, A Gray, S Petersen, M Rayner. Economic burden of cardiovascular diseases in the enlarged European Union, Eur.Heart J. 27 (2006) 1610-1619.

[8] R Luengo-Fernandez, J Leal, A Gray, S Petersen, M Rayner. Cost of cardiovascular diseases in the United Kingdom, Heart. 92 (2006) 1384-1389.

[9] AC Rohr, RE Wyzga. Attributing health effects to individual particulate matter constituents, Atmos.Environ. 62 (2012) 130-152.

[10] M Gualtieri, E Longhin, E Pezzolato, P Mantecca, E Molteni, J Holme, et al. In vitro effects of summer and winter Milan particulate matter, Toxicol.Lett. 196 (2010) S65.

[11] M Camatini, V Corvaja, E Pezzolato, P Mantecca, M Gualtieri. PM10-biogenic fraction drives the seasonal variation of proinflammatory response in A549 cells, Environ.Toxicol. 27 (2012) 63-73.

[12] E Longhin, E Pezzolato, P Mantecca, J Holme, A Franzetti, M Camatini, et al. Season linked responses to fine and quasi-ultrafine Milan PM in cultured cells, Toxicology in Vitro. 27 (2013) 551-559.

[13] SE Manahan, Fundamentals of environmental chemistry, CRC press 2011.

[14] PL Kinney, M Aggarwal, ME Northridge, NA Janssen, P Shepard. Airborne concentrations of PM(2.5) and diesel exhaust particles on Harlem sidewalks: a community-based pilot study, Environ.Health Perspect. 108 (2000) 213-218.

[15] TM Naser, Y Yoshimura, K Sekiguchi, Q Wang, K Sakamoto. Chemical composition of PM 2.5 and PM 10 and associated polycyclic aromatic hydrocarbons at a roadside and an urban background area in Saitama, Japan, Asian Journal of Atmospheric Environment. 2 (2008) 90-101.

[16] N Khan, H Swartz. Measurements in vivo of parameters pertinent to ROS/RNS using EPR spectroscopy, Mol.Cell.Biochem. 234 (2002) 341-357.

[17] GL Squadrito, R Cueto, B Dellinger, WA Pryor. Quinoid redox cycling as a mechanism for sustained free radical generation by inhaled airborne particulate matter, Free Radical Biology and Medicine. 31 (2001) 1132-1138.

[18] J Robertson, E O'reilly. Electronic and atomic structure of amorphous carbon, Physical Review B. 35 (1987) 2946.

[19] H Von Bardeleben, J Cantin, K Zellama, A Zeinert. Spins and microstructure of amorphous carbon, Diamond and related materials. 12 (2003) 124-129.

[20] BH Bielski, RL Arudi, MW Sutherland. A study of the reactivity of HO2/O2- with unsaturated fatty acids, J.Biol.Chem. 258 (1983) 4759-4761.

[21] WA Pryor. Oxy-radicals and related species: their formation, lifetimes, and reactions, Annu.Rev.Physiol. 48 (1986) 657-667.

[22] IB Afanas' ev, Superoxide ion: chemistry and biological implications, CRC Press 1991.

[23] FJ Miller Jr, WJ Sharp, X Fang, LW Oberley, TD Oberley, NL Weintraub. Oxidative stress in human abdominal aortic aneurysms: a potential mediator of aneurysmal remodeling, Arterioscler.Thromb.Vasc.Biol. 22 (2002) 560-565.

[24] HA Omar, PD Cherry, MP Mortelliti, T Burke-Wolin, MS Wolin. Inhibition of coronary artery superoxide dismutase attenuates endothelium-dependent and -independent nitrovasodilator relaxation, Circ.Res. 69 (1991) 601-608.

[25] Y Li, MA Trush. Diphenyleneiodonium, an NAD (P) H oxidase inhibitor, also potently inhibits mitochondrial reactive oxygen species production, Biochem.Biophys.Res.Commun. 253 (1998) 295-299.

[26] G Merenyi, JS Lind. Role of a peroxide intermediate in the chemiluminescence of luminol. A mechanistic study, J.Am.Chem.Soc. 102 (1980) 5830-5835.

[27] HP Misra, I Fridovich. The role of superoxide anion in the autoxidation of epinephrine and a simple assay for superoxide dismutase, J.Biol.Chem. 247 (1972) 3170-3175.

[28] D Thomas. Handbook of Methods for Oxygen Radical Research. J.Pediatr.Gastroenterol.Nutr. 7 (1988) 314-316.

[29] BH Bielski, GG Shiue, S Bajuk. Reduction of nitro blue tetrazolium by CO2-and O2-radicals, J.Phys.Chem. 84 (1980) 830-833.

[30] T Munzel, IB Afanas'ev, AL Kleschyov, DG Harrison. Detection of superoxide in vascular tissue, Arterioscler.Thromb.Vasc.Biol. 22 (2002) 1761-1768.

[31] C Rota, CF Chignell, RP Mason. Evidence for free radical formation during the oxidation of 2'-7'-dichlorofluorescin to the fluorescent dye 2'-7'-dichlorofluorescein by horseradish peroxidase:: Possible implications for oxidative stress measurements, Free Radical Biology and Medicine. 27 (1999) 873-881.

[32] C Rota, YC Fann, RP Mason. Phenoxyl free radical formation during the oxidation of the fluorescent dye 2',7'-dichlorofluorescein by horseradish peroxidase. Possible consequences for oxidative stress measurements, J.Biol.Chem. 274 (1999) 28161-28168.

[33] MM Oosthuizen, D Greyling. Antioxidants suitable for use with chemiluminescence to identify oxyradical species, Redox Report. 4 (1999) 277-290.

[34] M Brustolon, Electron paramagnetic resonance: a practitioner's toolkit, John Wiley & Sons 2009.

[35] GR Buettner, LW Oberley. Considerations in the spin trapping of superoxide and hydroxyl radical in aqueous systems using 5, 5-dimethyl-1-pyrroline-1-oxide, Biochem.Biophys.Res.Commun. 83 (1978) 69-74.

[36] E Finkelstein, GM Rosen, EJ Rauckman. Spin trapping of superoxide and hydroxyl radical: practical aspects, Arch.Biochem.Biophys. 200 (1980) 1-16.

[37] E Finkelstein, GM Rosen, EJ Rauckman. Production of hydroxyl radical by decomposition of superoxide spin-trapped adducts, Mol.Pharmacol. 21 (1982) 262-265.

[38] A Barbon, M Brustolon. An EPR Study on Nanographites, Applied Magnetic Resonance. 42 (2012) 197-210.

[39] M Tommasini, C Castiglioni, G Zerbi, A Barbon, M Brustolon. A joint Raman and EPR spectroscopic study on ball-milled nanographites, Chemical Physics Letters. 516 (2011) 220-224.

[40] S Stoll, A Schweiger. EasySpin, a comprehensive software package for spectral simulation and analysis in EPR, Journal of Magnetic Resonance. 178 (2006) 42-55.

[41] G Feher, A Kip. Electron spin resonance absorption in metals. I. Experimental, Physical Review. 98 (1955) 337.

[42] FJ Dyson. Electron spin resonance absorption in metals. II. Theory of electron diffusion and the skin effect, Physical Review. 98 (1955) 349.

[43] NW Ashcroft, ND Mermin, Solid State Physics, Saunders College, Philadelphia, 1976.

[44] AF Orchard, Magnetochemistry, Oxford University Press 2003.

[45] ET Denisov, IB Afanas' ev, Oxidation and antioxidants in organic chemistry and biology, CRC press 2005.

CHAPTER 7 - GENERAL DISCUSSION AND CONCLUSION

The major aim of this thesis was to identify and characterize the different types of defects that can be found in graphene-like systems by using electron paramagnetic resonance spectroscopy. In the end of the project we also consider the reactivity of carbon-based materials connected with the presence of these defects.

7.1 - Characteristics of the EPR spectra of defects

In order to characterize by EPR the defects in graphenic materials, we considered and studied different kinds of samples: chemically exfoliated graphites with different degrees of exfoliation (Chapter 4), reduced graphene oxide (Chapter 4) and graphene quantum dots, both undoped and doped with nitrogen atoms (Chapter 5).
Defects can be considered an imperfection, which affects the general response of a material. It has a vague meaning without taking into account a reference state considered as a 'perfect' state. We consider the graphene (single layer or few layers thick) as the reference state (perfect) from which we can mark the differences.
Because we used EPR spectroscopy, the observed defects are naturally associated to the presence of a magnetic moment; substantially the studied defects are (para)magnetic, and are a fraction of the possible defects that can be present in graphene-like systems. Magnetic moments are associated to the presence of unpaired electrons in particular states and we have to say that unpaired electrons are naturally present in a pure graphene structure above 0 K as conduction electrons excited to the conduction band.
Topological defects in the structure can localize electrons in other types of orbitals, with specific characteristics that can be studied by EPR.
We first start to discuss the characteristics of conduction electrons that can be considered as a characteristic of a bulk graphene-based material. Conduction electrons in graphene-like systems have very clear and univocal EPR characteristics. If the material is more thick than the penetration depth of the mw radiation the lineshape is asymmetrical (Dysonian [1,2]). This has been observed for graphitic materials [3,4]. On the other hand, if the sample is made of few layers, the lineshape is Lorentzian [5]. Both graphite and graphene are zero-gap semiconductors, and only the electrons that are promoted in the conduction band give rise to the EPR signal. Therefore, in the case of conduction electrons, we observe an increase of the EPR intensity by increasing the temperature [3,5]. The $\boldsymbol{g}$-tensors of these systems reflects their structure. For single or few-layer materials, the spin-orbit contribution is negligible and the tensors are nearly isotropic with values slightly higher than g_e [5], if the sample is more graphitic-like, the tensors are highly anisotropic, with

perpendicular components near to g_e and parallel components that can reach values of about 2.1 for bulk materials at low temperatures [3].
We found signals of conduction electrons in the cw spectra of exfoliated graphites and reduced graphene oxide (Chapter 4). The spectrum of sample EH, was simulated using Dysonian lineshapes (Fig. 3.4) meaning that this sample has substantially retained the graphitic structure of the starting materials. The other samples, EK, EHK and RGO, showed Lorentzian lineshape (Fig. 3.4) since they are more exfoliated and the different graphene planes are sufficiently separated to enable a good penetration of the mw radiation. For all these sample an increase of the magnetic susceptivity by increasing the temperature was indeed observed (Fig.s 3.5, 3.6, 3.7 and 3.8).

From the analysis of the data, by putting together all the information coming from the techniques that have been used to characterize the samples, we could identify and distinguish at least four types of defects that are EPR active: 1) structures generating localization of electrons, 2) local topological rearrangements of the graphenic lattice, 3) molecular-like radicals and 4) structures generating delocalized non-interacting electrons. All these systems have different EPR features that we will collect in this chapter. Some of our attribution are confirmed by the results of the DFT study reported in Chapter 6.

7.1.1 - Structures generating localization of electrons

The edge of a graphene sheet acts as a perturbation of the ideal graphite system. The graphene structure near the edges is not different from the bulk material, but the electron in that regions are affected by the interruption of the conjugated system. These electron can be described by π-wavefunctions with limited extension [6,7]. There are two basic edge shapes, armchair and zigzag (see section 1.3.2 in the introduction), which determine the properties of graphene flakes. It was shown that flakes with zigzag edges possess localized electrons with energies close to the Fermi level [7-10]. In contrast, localized electrons are absent for flakes with armchair edges. These states can be observed not only at the external edges of a graphene flakes, but also at the edges of holes in the graphene lattice generated by vacancies (see section 1.3). EPR signals of localized electrons have Lorentzian lineshape and have generally low linewidth that becomes narrower by decreasing the temperature. The absence of a hyperfine structure for these states and the symmetry of the lineshape are indications of an exchange process that leads to the averaging of the interactions. The exchange can be with mobile electrons [11,12] or with other localized electrons [11]. The magnetic susceptivity follows a Curie-like behavior and the $\boldsymbol{g}$-tensor is nearly isotropic with values of about 2.003-2.004.
The neutral PAH that we studied in section 5.4.1 by DFT can be considered as a limiting case of these edge states. They have unpaired electrons in non-bonding molecular orbitals that are located inside the HOMO-LUMO gap. With DFT we could

verify the localization of electron density along the zigzag edges (see Fig. 5.4) and we calculated the $\boldsymbol{g}$-tensors. The values that we found in section 5.4.1 are lower with respect to those reported in literature for localized electrons in edge states, the differences come from the choice of the models that we used, since they are small molecules, not materials. By looking increasing the dimension of the models (Fig. 5.3) we noticed that the g-value increases toward values typical graphene-like materials. Signals due to localized electrons in edge states were observed in the cw spectra of all the studied samples, especially at low temperatures, because of their Curie-like behavior and their narrow linewidth. The linewidth for exfoliated graphites and RGO at low temperature are between 2 and 4 G and the g-tensors associated to these signals are in the right range for these systems (see Tables 3.3, 3.5 and 3.6).
For the undoped GQDs, we did not observe signals due to localized electrons, but in that case, we recorded the spectra at 80 K or higher, while for expanded graphites and RGO we reached the temperature of liquid helium. A narrow signal of localized electrons was evident in the spectrum of N-GQDs at 80 K. The nitrogen atoms introduced in the graphene lattice can be considered as internal defects (see section 1.3.1), which likely produces edge states inside the graphene structure at a higher concentration than for GQDs.
Signals of edge states were not observed in the pulsed spectra, meaning that they have fast relaxation processes.

7.1.2 - Rearrangement of graphenic lattice

These types of defects are due to rearrangements of the graphene crystal lattice with displacement of some carbon atoms that modify the hexagonal structure. These rearrangements have been described in the introduction of the thesis and can be found after the formation of vacancies or in Stone-Wall defects. These modifications of the graphene lattice comes after the rotation of one or more $C-C$ bonds, in this way pentagonal, heptagonal or larger rings are formed (see Fig.s 1.4, 1.5 and 1.6 in Chapter 1).
The formation of these structures implies the distortion of the graphene sheet. In particular, we know from theory [13] and from all the calculation that we reported in Chapter 5 that a pentagonal ring inserted in a planar honeycomb structure induces a curvature of the structure itself. If more pentagons are present in the same structure, the curvature is higher (see for example the calculations on fullerene fragments reported in section 5.4.4). Heptagonal rings also induce a curvature of the plane that is saddle like. The presence of vacancies and Stone-Wall defects has both the effect of interrupting the conjugated π-system and of causing the bending of the graphene plane.
By the DFT calculation shown in Chapter 5 we know that the bending of a carbon π-system induced by pentagonal rings results in a lowering of the $\boldsymbol{g}$-tensor of the system. The greater is the curvature, the lower are the principal values of the tensor

that can become appreciably lower than the free electron value g_e (see values in Table 5.6).

In a couple of sample analyzed in this thesis we found components with g-values typical of such defects. The components EK-1 and EHK-1 (Chapter 4), at high temperature, have $\boldsymbol{g}$-tensor values that are lower than g_e (see Figures 3.7b and 3.8b), meaning that in these samples the graphene layers are curved because of topological distortion. Some degree of curvature for these samples can be seen from the SEM images reported in Figure 3.1. The samples EK and EHK have been subjected to intercalation with potassium metal, reaction with ethanol and sonication. All these processes likely produced many defects in the graphene layers that could result in atomic rearrangements and formation of bent structures.

The lineshape of components EK-1 and EHK-1 is Lorentzian (Tables 3.5 and 3.6) and the signal has a Curie-like behavior (Fig.s 3.7 and 3.8) the low $\boldsymbol{g}$-tensors have been observed only at higher temperature. From these results we can say that the defects formed after lattice rearrangements are characterized by electron delocalized in small confined regions, created by the distortion of the conjugated π-system and not interacting with other electrons or paramagnetic nuclei.

7.1.3 - Molecular-like radicals

Molecular-like radicals are small graphene fragments with dimension typical of a large molecule (1-5 nm). These systems have unpaired electrons that are localized or delocalized in a limited number of carbon atoms. In solid-state, hyperfine coupling with paramagnetic nuclei, like terminal hydrogens or dopants that could be present in the graphene lattice, can be evident. Because of these couplings, molecular-like radicals have inhomogeneous lineshapes. The $\boldsymbol{g}$-tensor for such systems is generally isotropic or slightly anisotropic with values of about 2.003-2.004 [14,15]. The magnetic susceptivity has a Curie-like behavior.

Molecular-like radicals were observed with pulsed techniques for all our samples: exfoliated graphites, RGO (Chapter 4) and graphene quantum dots (Chapter 5). We did not observe them in the cw spectra, so they are not present at high concentration, but have longer relaxation times that enable us to measure them in the pulsed spectra.

By looking at the ESEEM and ENDOR spectra of our samples, we can find an estimate of the average dimension of these radicals. Regarding the quantum dots, from the proton signal in the spectra we found an isotropic coupling constant of about 0.7 G for the undoped sample and 1.9 G for the N-doped (see section 4.3.2). These values are typical of terminal protons in π-systems. By comparing the values with the hfccs of coronene and circumcoronene, obtained with a simple Hückel calculation, we can have an indication about the extent of the π-system. For coronene we found an isotropic coupling constant of about 1.5 G and for circumcoronene of about 0.6 G; the π-systems of these molecules comprehend respectively in 24 and 54 carbon

atoms. The undoped GQDs have hfccs similar to that of circumcoronene, so we can assume that the electrons are delocalized in a region that have almost the same size. That is in agreement with the average size of the GQDs of about 2 nm determined by STM (Fig. 4.1), that correspond to 50-70 carbon atoms. The N-doped GQDs, on the other hand, have slightly higher hfccs with respect to coronene. For them we assume that the unpaired electrons are delocalized in regions of less than 20 carbon atoms. That is the same result that we found in Chapter 5 by comparing the isotropic hyperfine constant of the nitrogen dopant, determined by the Davies ENDOR spectrum (Fig. 4.4), with the results of DFT calculation reported in Table 4.4.
Molecular-like radicals were observed also for exfoliated graphites and RGO. From the ESEEM spectra of these samples (Fig. 3.9), using the same procedure described for the GQDs, we found coupling constants with protons of about 1.8 G (see section 3.3.4), similar to what we found for N-GQDs. The molecular-like radicals that are present in the exfoliated graphites and RGO are composed of delocalized fragments of about 20-25 carbon atoms.

7.1.4 - Structures generating delocalized non-interacting electrons

These systems have some properties in common with the molecular-like radicals. They have unpaired electrons delocalized in fragments of a graphene plane with size larger than those determined for the molecular states (about 100 carbon atoms). These structure can be seen as large molecules, they are not described in terms of bands, but with molecular orbitals. They can be radical ions or neutral radical, like non-Kekulè molecules. Their EPR signal has Lorentzian lineshape, meaning that no hyperfine coupling with nuclei is observable. The unpaired electrons are independent from each other; therefore, the magnetic susceptibility follows a Curie-like trend. The EPR linewidth increases by decreasing the temperature, differently from the localized edge states. The variation of the linewidth with the temperature is caused by the fluctuations in the spin-orbit interaction for the electron associated to the scattering processes [16,17].
By analyzing the samples reported in this thesis, we found signals due to delocalized isolated electrons in the cw spectra of the GQDs (Chapter 5). They were the only component of the spectrum of the undoped sample, in the whole range of temperatures studied (80-290 K) and a major component of the doped sample. These species were present in our samples with concentration much higher than the molecular-like radicals since we could observe them in the cw spectra, but relax faster with respect to these last because we were not able to measure them with pulsed experiments.

7.2 - Conclusions

This PhD project has been mainly oriented to the study of different types of defects that can be present in graphene-like materials by means of EPR techniques, continuous wave (cw) or pulsed and of DFT calculations. The work was divided into three main parts: in the first part, we used EPR spectroscopy techniques to study some graphene-like materials. In the second part we performed a computational DFT study on some conjugated molecules in order to find a correlation between their morphology and their $\boldsymbol{g}$-tensor. The last part was devoted to the study of the reactivity of defect states in carbon materials.

We have analyzed different kind of graphene-like materials during the whole project. Chemically exfoliated graphites, reduced graphene oxide and graphene quantum dots. A careful analysis of the cw and pulsed EPR signals of the different materials enabled us to disentangle and classify all the contributions to the spectra and to determine which of them are due to defect states or to other EPR-active species. We could also highlight the differences and similarities between the samples. By comparing the results found for all samples, we identified and characterized the different types of defects that can be found in graphene-like systems.

The analysis and rationalization of the EPR spectra were facilitated by comparing the experimental results with the DFT calculations. We were able to correlate the lowering of the $\boldsymbol{g}$-tensor principal values with an increase of the curvature of a graphene plane induced by the presence of pentagonal rings. DFT calculation helped also in understanding the nature of the nitrogen doping for the doped GQDS.

The reactivity of the defects that we have characterized has been studied in the last part of the thesis. We proved that the electrons localized in carbon-based materials like graphite and nanosized amorphous carbon can participate to the reaction of formation of reactive oxygen species and increase the overall rate of the reaction. We also a clear correlation between the size of the carbon particles and the rate of the accelerated reaction meaning that not only the presence of defects in the materials, but also their concentration increases the reactivity.

References

[1] G Feher, A Kip. Electron spin resonance absorption in metals. I. Experimental, Physical Review. 98 (1955) 337.

[2] FJ Dyson. Electron spin resonance absorption in metals. II. Theory of electron diffusion and the skin effect, Physical Review. 98 (1955) 349.

[3] G Wagoner. Spin resonance of charge carriers in graphite, Physical Review. 118 (1960) 647.

[4] A Barbon, M Brustolon. An EPR Study on Nanographites, Applied Magnetic Resonance. 42 (2012) 197-210.

[5] L Ćirić, A Sienkiewicz, B Nafradi, M Mionić, A Magrez, L Forro. Towards electron spin resonance of mechanically exfoliated graphene, physica status solidi (b). 246 (2009) 2558-2561.

[6] M Tommasini, C Castiglioni, G Zerbi, A Barbon, M Brustolon. A joint Raman and EPR spectroscopic study on ball-milled nanographites, Chemical Physics Letters. 516 (2011) 220-224.

[7] M Fujita, K Wakabayashi, K Nakada, K Kusakabe. Peculiar localized state at zigzag graphite edge, Journal of the Physical Society of Japan. 65 (1996) 1920-1923.

[8] K Nakada, M Fujita, G Dresselhaus, MS Dresselhaus. Edge state in graphene ribbons: Nanometer size effect and edge shape dependence, Physical Review B. 54 (1996) 17954.

[9] K Wakabayashi, M Fujita, H Ajiki, M Sigrist. Electronic and magnetic properties of nanographite ribbons, Physical Review B. 59 (1999) 8271.

[10] K Wakabayashi, M Sigrist, M Fujita. Spin wave mode of edge-localized magnetic states in nanographite zigzag ribbons, Journal of the Physical Society of Japan. 67 (1998) 2089-2093.

[11] VJ Joly, K Takahara, K Takai, K Sugihara, T Enoki, M Koshino, et al. Effect of electron localization on the edge-state spins in a disordered network of nanographene sheets, Physical Review B. 81 (2010) 115408.

[12] MA Augustyniak-Jabłokow, K Tadyszak, M Maćkowiak, YV Yablokov. EPR evidence of antiferromagnetic ordering in single-layer graphene, physica status solidi (RRL)-Rapid Research Letters. 5 (2011) 271-273.

[13] F Banhart, J Kotakoski, AV Krasheninnikov. Structural defects in graphene, ACS nano. 5 (2010) 26-41.

[14] NM Atherton, N Atherton, Electron spin resonance: theory and applications, Ellis Horwood Chichester 1973.

[15] R Erickson, A Lund, M Lindgren. Analysis of powder EPR and ENDOR spectra of the biphenyl radical cation on H-ZSM-5 zeolite, silica gel and in CFCl 3 matrix, Chem.Phys. 193 (1995) 89-99.

[16] D Huber, R Urbano, M Sercheli, C Rettori. Fluctuating field model for conduction electron spin resonance in graphite, Physical Review B. 70 (2004) 125417.

[17] K Tadyszak, MA Augustyniak-Jabłokow, AB Więckowski, L Najder-Kozdrowska, R Strzelczyk, B Andrzejewski. Origin of electron paramagnetic resonance signal in anthracite, Carbon. 94 (2015) 53-59.